National Library of Canada
Bibliothèque nationale du Canada

Canadian Theses Service
Service des thèses canadiennes

Ottawa, Canada
K1A 0N4

NOTICE

The quality of this microform is heavily dependent upon the quality of the original thesis submitted for microfilming. Every effort has been made to ensure the highest quality of reproduction possible.

If pages are missing, contact the university which granted the degree.

Some pages may have indistinct print especially if the original pages were typed with a poor typewriter ribbon or if the university sent us an inferior photocopy.

Reproduction in full or in part of this microform is governed by the Canadian Copyright Act, R.S.C. 1970, c. C-30, and subsequent amendments.

AVIS

La qualité de cette microforme dépend grandement de la qualité de la thèse soumise au microfilmage. Nous avons tout fait pour assurer une qualité supérieure de reproduction.

S'il manque des pages, veuillez communiquer avec l'université qui a conféré le grade.

La qualité d'impression de certaines pages peut laisser à désirer, surtout si les pages originales ont été dactylographiées à l'aide d'un ruban usé ou si l'université nous a fait parvenir une photocopie de qualité inférieure.

La reproduction, même partielle, de cette microforme est soumise à la Loi canadienne sur le droit d'auteur, SRC 1970, c. C-30, et ses amendements subséquents.

NL-339 (r. 88/04) c

Canada

TECHNIQUES FOR THE CONTINUOUS MEASUREMENT OF MELT TEMPERATURE

by

Hyeon-Soo Choi

Department of Mining and Metallurgical Engineering
McGill University
Montreal, Canada

January, 1991

A thesis submitted to the Faculty of Graduate Studies
and Research in partial fulfillment of the requirements
for the degree of Doctor of Philosophy

ISBN 0-315-67666-3

Abstract

Continuous temperature measurement of molten steel in new as well as existing steelmaking processes is not always feasible with current technology. However, it is a well known fact that molten steel temperature, especially during the continuous casting operation, can have a profound effect on the quality of the product. A knowledge of the instantaneous steel temperature in the tundish can serve as a valuable tool in the quest for better quality. With the implementation of statistical process control techniques such occurrences as breakouts, tundish freeze up or the nucleation of an extensive area of columnar grains in the cast section can be reduced.

However, conventional thermocouples cannot withstand the severe corrosion around the slag line for a sustained period of time. Even though the sensing wires that comprise the hot junction can, if well protected, be used for long periods of time without serious deterioration, a suitable refractory cover or sleeve must be applied to the thermocouple prior to using it.

For the present work, two methods for continuously measuring melt temperature were developed. One of these relies on deducing melt temperature while the other is based on providing a cooled sleeve for the thermocouple to minimize slag line corrosion. The first technique involves the use of multiple thermocouples embedded in a refractory section at various displacements. When the refractory is contacted by the melt, transient heat transfer is initiated through the section. By analyzing this transient behaviour with a suitable heat transfer model, it is possible to infer the temperature of the

melt. A mathematical model that adequately describes this process has been developed and tested.

An alternative approach that was developed uses heat pipe technology to prevent the corrosion of the thermocouple probe through solidification of slag onto the heat pipe which can serve as a protector of the probe. Heat pipes are devices capable of transferring large quantities of heat with very small temperature differences. Advantages of the heat pipe when used as a heat transmission device are constructional simplicity, flexibility, high heat transport capability, and no need for external pumping device. The heat pipe consists of a closed evacuated tube, porous wicking material, and working fluid. Heating one part of the external surface leads to evaporation of the working fluid and the establishment of a pressure gradient within the heat pipe. The resulting pressure difference drives the vapor from the evaporator to the condenser where the pressure and temperature are slightly lower. The effective conductance of the heat pipe can be several orders of magnitude higher than that of an equivalent solid copper bar. In the second part of this thesis, the feasibility of incorporating heat pipe technology to solidify and maintain a thin layer of slag on the heat pipe while it is in operation is presented.

Résumé

Avec la technologie courante, il n'est pas toujours faisable de mesurer en continu, la température de l'acier liquide dans les procédés sidérurgiques. Par contre, il est bien connu que la température de l'acier liquide peut avoir un effet significatif sur la qualité du produit fini, particulièrement pendant les opérations de coulée continue. La connaissance de la température instantanée de l'acier dans un séparateur peut devenir un outil très utile dans la quête d'une meilleurs qualité. La fréquence de certains problèmes tels que les bris, les solidifications de métal dans le séparateur ou la formation de grains en colonne sur des surfaces étendues, peut être réduite par l'utilisation de techniques statistiques de contrôle de procédé.

Cependant, les thermocouples conventionnels ne peuvent être maintenus dans les conditions sévères de corrosion autour de la couche de laitier. Bien que, s'ils sont bien protégés, les deux fils qui forment la jonction peuvent supporter une longue exposition sans détérioration sérieuse, une gaine de matériel réfractaire approprié doit être installée avant l'utilisation du thermocouple.

Dans le cadre de cette étude, deux méthodes ont été développé pour mesurer en continu la température du métal liquide. L'une de celle-ci est basée sur la déduction de la température du métal tandis que l'autre fournie une gaine de refroidissement au thermocouple afin de minimiser la corrosion due au laitier. Une première technique fait appel à un système de thermocouples, encastrés à différentes profondeurs dans un bloc de matériel réfractaire. Quand le métal liquide touche le bloc, un transient de transfert de chaleur

est amorcé à travers le bloc. A l'aide d'un modèle approprié de transfert de chaleur, il est possible de déterminer la température du métal liquide par l'analyse de ce transient. Un modèle mathématique qui décrit adéquatement ce procédé a été développé et testé.

Une seconde approche utilise la technologie des caloduques pour prévenir la corrosion du thermocouple par la solidification d'une couche de laitier sur le caloduque. Les caloduques sont des objets capable de transférer d'importante quantité de chaleur avec de très faible gradient de température. Lorsque utilisé pour transmettre la chaleur, les avantages des caloduques sont: simplicité de construction, flexibilité, haute capacité de transfert de chaleur, et pas d'appareil de pompage externe. Le caloduque consiste en un tuyau fermé sous vide, d'une mèche en matériau poreux et d'un fluide. Chauffer une des parties extérieures provoque l'évaporation du fluide et un gradient de pression à l'intérieur du caloduque. La différence de pression résultante déplace les vapeurs de l'évaporateur vers le condenseur où la pression et la température sont légèrement plus basses. La conductivité du caloduque peut être plus élevée que celle d'une barre de cuivre équivalente par plusieurs ordres de grandeur. La technologie des caloduques peut être utilisée pour solidifier et maintenir solide une mince couche de laitier sur un caloduque, à partir des caractéristiques de ce dernier. Une étude de faisabilité de cette application est présentée dans la seconde partie.

Acknowledgements

The author wishes to express his gratitude to his supervisor, Professor Frank Mucciardi for his guidance and support.

The author extends special thanks to Professor R. I. L. Guthrie for his support.

The author also wishes to appreciate to his wife and parents for their patience and understanding throughout the course of this work.

Contents

List of Figures

List of Tables

Nomenclature

A_c	area of the cooling zone
C	heat capacity
d_i	inside diameter of the thermosyphon tube
d_o	outside diameter of the thermosyphon tube
g	gravitational constant
h	convective heat transfer coefficient
h_c	condensation heat transfer coefficient
h_{ic}	interfacial conductance defined by Eq. (3.13)
H	constant $(h/\rho C)$
ΔH_v	latent heat of vaporization
k	thermal conductivity
L	equivalent immersion depth
L_i	immersion depth
l	length of thermosyphon
M	Merit number
P_{cr}	critical pressure
ΔP_c	surface tension pressure difference acting at the surface of the wick capillary pores that return the liquid to the evaporator from the condenser
ΔP_l	pressure drop due to the liquid flow in the wick
ΔP_v	pressure drop due to the vapor flow
ΔP_g	gravitational head which may be zero, positive or negative

$\dot{Q}$	heat flow rate
$\dot{q}''$	heat flow rate per unit area
$\dot{q}'''$	rate of heat generation per unit volume
q_c	critical heat flux based on heated section area
Δr	radial nodal point spacing
Re	film Reynolds number defined by Eq. (3.3)
T	temperature
T^*	dimensionless temperature
u, v	velocity
V	volume of node
V_e^+	dimensionless fill charge: volume of working fluid divided by the volume of heated section
Δz	vertical nodal point spacing
α	thermal diffusivity
μ	dynamic viscosity
ν	kinematic viscosity
δ	thickness of the condensate film
ρ	density
θ	temperature at time t
θ'	temperature at time $t + \Delta t$

subscripts

a	adiabatic section
c	condenser section or critical condition
e	evaporator section
g	gas

l	liquid
t	total
v	vapor
∞	free stream

Chapter 1

Introduction

In the past decades, the tonnage and percentage of continuously cast steel has increased dramatically. This trend will continue because the advantages of continuous casting over ingot casting are widely recognized as higher yields, higher production rates, and superior surface and internal quality. The end product of the continuous casting process is a semi-finished shape thus eliminating the primary rolling stage required in the ingot casting process. In the continuous casting process, molten steel is carried by a ladle and teemed into a tundish which, in turn, feeds molten steel to one or several water cooled copper molds. A thin solid skin of steel (5 to 20 mm thick) is formed. The solidified steel shell containing a molten core passes through a water spray zone to completely solidify the section which is then cut to size.

The tundish performs several important functions including:

- distribution of steel between strands,
- separation of non-metallic inclusions,
- control of casting speed,
- acts as a buffer during ladle changes.

Moreover, the current trend is to expand the role of the tundish and use it as a continuous reaction vessel for carrying out various metallurgical treatments including[1]:

- deoxidation adjustment,
- alloy trimming,
- desulfurization,
- non-metallic inclusion control,
- grain size control.

Thus. the tundish in the continuous casting operation has become a vital component whose role is complicated by the added tasks it is required to perform.

The solidified product from a continuous casting machine can be characterized by a number of parameters one of which is microstructure. The microstructure of the casting depends on many variables, however it is a well known fact that molten steel temperature, especially during the continuous casting operation, can have a profound effect on the quality of the product[2, 3, 4, 5, 6]. A number of techniques such as radioactive tracer additions[7], sulphur prints, and micro-etching techniques have been used to study the microstructure of continuously cast steel. In general, the cast structure consists of three zones as is also the case in ingot casting. These are:

- a chilled zone near the strand surface consisting of fine equiaxed crystals that forms high in the mould
- a columnar zone in which dendrites extend inward from the chilled zone perpendicular to the strand surface

- a central equiaxed region consisting of randomly oriented dendrites.

The internal structure of the casting can be characterized by the relative size of the columnar and the equiaxed zones. The sizes of these areas can be used to figure out the internal quality of the product. The columnar zone is more susceptible to cracking than the equiaxed zones, moreover, a long columnar zone increases centerline segregation and porosity. It is to be noted that the relative size of the equiaxed and columnar zones depends on variables such as casting temperature, machine design, flow conditions in the liquid pool and steel chemistry.

Effects of steel temperature

W. Irving and A. Perkins[2] showed that the solidification rate is independent of casting speed for a constant spray water flow. They showed with a mathematical model of the caster that even doubling the spray water produces only a small increase in solidification rate, because the rate of heat extraction is limited mainly by the thermal conductivity of the steel and the surface condition of the shell. Thus, the width of the columnar and equiaxed zones are only marginally influenced by casting speed and spray cooling water; however, liquid steel superheat has a dominant effect.

K. Takeo and H. Iwata[3] and H. Iwata et al.[4] studied the effect of tundish superheat on the size of the equiaxed zone in a 0.8 % carbon steel continuously cast into 110 mm square billets at a casting speed of 2.4 m/min. Even though there is considerable scatter in their data, it is clear that increasing the tundish superheat decreases the size of the equiaxed zone. Low superheat provides a large number of nuclei for equiaxed crystals and results the temperature was increased. Taken together, sulphur spots and oxygen content provide a measure of the occurrence of nonmetallic inclusions. When superheat was increased from 20 °C to 38 °C, large inclusions were reduced by an average of 36 % and the oxygen content by about 60 %. Abo and Arai[11] also showed that the defect index was decreased as the steel temperature in the tundish was increased for the continuous casting of slabs of type 304 stainless steel.

Cracks

One of the problems that arises in the continuous casting of steel is the formation of cracks. Many types of crack formations are due to the nature of the continuous casting process itself. Continuous casting extracts heat at a remarkable rate with the combination of mould, spray and radiant cooling. This rapid cooling results in steep temperature gradients in the steel shell and generates thermal stresses when the shell expands or contracts. Cracks will form in the shell when the tensile strain exceeds the local strain to fracture of the steel.

Cracks can be divided into surface and internal cracks. Surface cracks are oxidized by air and are not rewelded during rolling. Generally these cause more problems than internal cracks. Internal cracks are less susceptible to oxidation, however, they can cause quality problems too. Internal cracks found between the center and the surface of the cast section are commonly called halfway cracks, radial cracks or ghost lines. Many investigators [12, 13, 14, 15, 16] have reported that the factors contributing to the formation of halfway cracks are excessive secondary cooling and a high casting temperature. In addition, the chemistry of the steel is also responsible for crack formation.

Excessive spray cooling is the main factor in the formation of midway cracks because it causes reheating of the surface after passing the spray zone and provides the driving force for cracking[12]. Reheating causes the surface to expand which results in a tensile strain in the interior region. High casting temperature also has an effect on the formation of midway cracks because it affects the cast structure. High steel temperature promotes the formation of a larger columnar zone. Midway cracks can be formed much more easily between the dendrites in the columnar zone which run perpendicular to the tensile stress than in the equiaxed zone. The occurrence of midway cracks can be diminished by the minimization of internal tensile strains. This can be accomplished by careful design of the spray system, improvement of the high temperature mechanical properties of steel, and minimal superheat.

Segregation

Centerline segregation is one of the serious quality problems during continuous casting that is a result of solute rejection of elements such as C, P, S, and Mn having a distribution coefficient less than one at the solidification front. Segregation of solute elements occurs on both micro and macro scales. Micro-segregation results from the freezing of solute enriched liquid between dendrites and does not cause major problems because it can be removed by annealing. Macro-segregation occurs on a large scale and can be observed in the central region of continuously cast section by radioactive tracer addition, sulphur prints, or micro-etching techniques. Macro-segregation is caused by mass movement of the solute enriched liquid away from the solidification front produced by[17]

(a) convectional forces due to differences in solute concentration and temperature in the liquid,

(b) motion of the liquid steel when poured into the mould and,

(c) gravitational forces on crystals growing in the liquid steel.

Macro-segregation is affected by the physical properties of the alloy component, convection in the liquid and solidification structure[18, 19]. The extent of centerline segregation and porosity is related to the cast structure; the severity of segregation and porosity increases as the columnar zone length increases or, correspondingly, the equiaxed zone width decreases. Therefore, variables such as superheat, section size and shape, chemistry, casting speed, and fluid flow all of which are known to affect cast structure, also produce changes in the degree of centerline segregation and porosity.

As explained earlier steel superheat has a predominant effect on the cast structure. By increasing superheat, the width of the central equiaxed zone decreases, and correspondingly the degree of centerline segregation and porosity increases. H. Iwata et al.[4] showed that the degree of centerline segregation was increased with increasing casting temperature especially for S, P and C in this order. In the case of Mn, segregation was negligible. From their investigation into the occurrence of core segregation as related to casting temperature, they concluded that 15 °C or less above the liquidus is the ideal casting temperature for minimizing harmful segregation. W. Irving and A. Perkins[20] studied the variations of the equiaxed zone for increases in Mn and S over nominal composition of 1524 × 178 mm slabs of X60 line pipe grade(0.2 % C). Segregation of sulphur was found to be more sensitive to increased tundish superheat than that of manganese. Increase in S compared with nominal composition was over 50 % while that of Mn was 10 % when the superheat was 20 °C.

Section size also affects the width of the central equiaxed zone and degree of segregation. R. J. Gray et al.[8] showed that the absolute width of central segregation increases as the cross section increases, but the relative size of the segregated zone decreases. Thus, from the quality viewpoint it is desirable to cast a large section size to decrease the relative length of the columnar zone. A casting of large section size requires longer solidification time which allows for the removal of superheat in the liquid core long before solidification is complete. From an energy and cost consideration, it is more beneficial to cast with minimum section size with satisfactory quality. The shape of the cross section of the casting also affects the width of the central equiaxed zone and segregation. A rectangular section will have less segregation than a square one even though the central equiaxed zone is smaller[21].

Casting speed also influences structure because higher speeds result in an increase in pool depth. The longer pool produced by increased casting speed is more prone to bridging and generally there is an increase in central pipe formation and segregation[22]. Increasing the casting speed reduces the residence time in the mould, thereby decreasing the solidification rate. This will result in an increase in the time required for the dissipation of the superheat, a delay in the nucleation and growth of equiaxed crystals, an increase in the size of the columnar zone[23] and an increase in the extent of axial segregation. The optimum casting speed will depend on the efficiency of heat extraction from the solidifying metal. This will be affected by the tundish superheat, casting cross section, extent of secondary cooling, and steel composition. A limiting factor for casting speed is the solid shell thickness below the mould because this shell must be sufficient to prevent break-outs. The rate of heat transfer through the mould is a minimum for low carbon steel, i.e. 0.1% C, and increases with carbon content to 0.25% at which composition it remains essentially constant[24]. This is the primary reason for the increased columnar zone and associated axial segregation exhibited by 0.1% C steel when compared with medium carbon steel[21]. Thus, optimum casting speeds should be determined to fit each steel composition and operating condition.

Steel carbon content is another variable that influences centerline segregation [4, 21, 25, 26]. Axial segregation causes quality problems in the production of continuously cast high carbon steels which are subsequently hot rolled and drawn into rod or wire products. This is especially true in high carbon steels, where segregation of carbon along the centerline of billets easily exceeds the eutectoid point thus causing the precipitation of cementite networks. This, together with the segregation of other elements or impurities and coupled with the existence of shrinkage cavities and centerline porosity, reduces the ductility of the material. It is well known that intense segregation can result in the deterioration of drawability and mechanical properties of steel wires. In wire production, defects such as segregation or shrinkage cavities along the axis of rod may cause numerous problems during cold drawing and can adversely affect the quality of the final products. If the intensity of the defects is comparatively small the tensile strength of the wire is not influenced, but the elongation and the reduction of area are decreased and the wire does not give the normal fracture surface of cup and cone shape. For samples with intense defects, the fracture surface showed typical cuppy shape[4], which is characteristic of a small reduction in fracture area. With such defects, toughness and tensile strength deteriorate. More intense defects cause the breaking of wires during the drawing or stranding process. Much research has been carried out on the continuous casting of small sections to find the influence of casting condition on the solidification structure or defects of the center part of billets. As for centerline segregation, one of the conclusions is that segregation is less in a billet with a large homogeneous equiaxed zone.

Haida et al.[27, 28] correlated the frequency of Hydrogen Induced Cracking(HIC) to the degree of semi-macro segregation. Hydrogen induced crack is initiated at an elongated manganese sulphide inclusion and propagates along the band structure. Centerline segregation enhances the occurrence of HIC because the positive segregation of manganese and sulphur accelerates the precipitation of manganese sulphide and the positive segregation of phosphorus and manganese causes the band structure. It was found that the better anti-HIC property of plates was achieved by having a lower degree of segregation in the slab. This improved anti-HIC property of plates was achieved by lowering the bulk concentration of phosphorous from 0.01 to 0.005% for slabs heat treated at 1250 °C for 16 hours.

Mixing in the liquid pool is achieved by the input stream or by external means such as electromagnetic stirring(EMS). EMS is one of the most important advances to control the internal structure of continuously cast steel. Columnar growth is decreased and equiaxed crystallization promoted by reducing the temperature gradient ahead of the solid/liquid interface with the application of EMS[4, 19, 29, 30, 31, 32]. An investigation conducted by H. Iwata[4] showed the effectiveness of EMS in reducing axial segregation in high carbon steel billets. EMS was very effective in reducing the extent of the columnar zone as well as segregation, especially at high superheats, but EMS showed little effect at low superheats. When there is no electromagnetic stirring axial segregation is reduced significantly as the superheat is lowered.

The molten steel should have sufficient superheat to allow easy flow of the steel from the beginning to the end of casting. Temperature of the steel in the tundish varies with time and position. It is typical that the temperature in the tundish at the beginning of the casting is relatively low due to the chilling effect of the tundish. With time it recovers to its normal temperature and remains relatively constant, however steel temperature drops toward the end of the casting. To decrease the temperature fluctuation at the beginning of the cast, at the end of the cast, and during ladle changes in sequence casting, a rapid heating system is employed at several plants in the world. Y. Habu et al.[10] showed that a temperature drop of 10-20 °C under normal casting conditions could be decreased to 0-5 °C when the tundish heating system was used. When steel of excessive superheat is poured in the tundish, it can be cooled by the addition of scrap even though this is not an ideal way to control steel temperature. In such cases casting speed should be decreased by reducing the tundish level to reduce the chance of breakout.

As mentioned previously, product quality is affected by the superheat of the melt. If the superheat is too high, it will lower the quality of the product and casting speed should be reduced to decrease the risk of breakout. If the superheat of the steel in the tundish becomes too low during casting, it may cause nozzle freeze-off. The physical properties of steel around its melting point limit the escape of inclusions. Thus an optimum tundish superheat is one that tends to minimize chemical segregation and the occurrence of inclusions in the product yet avoids freezing-off problems. The general conclusion of workers investigating continuous casting of high carbon steel is that the optimum degree of superheat in practice is between 10-15 °C[3]. Therefore, a knowledge of the instantaneous steel temperature in the tundish can serve as a valuable tool in the quest for better quality. With the implementation of statistical process control techniques such occurrences as breakouts, tundish freeze up or the nucleation of an extensive area of columnar grains in the cast section can be reduced.

Reoxidation of the molten steel increases the total oxygen content of the steel and is caused by several factors including:

- direct oxidation of both the stream as it falls through the air and the liquid metal surface
- oxidation of the metal in the pool by air entrained by the plunging stream
- chemical interaction of the steel with solid phases such as the refractory

To resolve one of the problems mentioned above the contact between the metal and air should be minimized. In the tundish, this can be done by adding artificial slag on the top surface.

Even though continuous tundish temperature can be valuable for improved quality control, continuous temperature measurement of molten steel in new as well as existing steelmaking processes is not a simple task with current technology. Conventional immersion type thermocouples are simply not resistant for sustained periods of time under corrosive slag conditions. Even though the sensing wires that comprise the hot junction can, if well protected, be used for long periods of time without serious deterioration, a suitable refractory cover or sleeve must be applied to the thermocouple prior to using it. In this study, two possible techniques for achieving continuous steel temperature measurements are developed. Both are considered to be novel approaches for the proposed application. Brief descriptions follow.

- The first technique involves the use of multiple thermocouples embedded in a test brick at varying displacements. When the test brick is contacted by hot media, transient heat transfer is initiated through the section. By analyzing this transient behaviour with a suitable heat transfer model (inverse heat conduction approach), it is possible to infer the bath temperature. Two mathematical models that adequately describe this process have been developed and tested. Mathematical formulations of both models are presented in the following chapter.
- An alternative approach is the use of a self cooling sleeve called a heat pipe to protect conventional immersion type thermocouples. Instead of using protective materials for the thermocouple, an annulus type heat

pipe can be placed around the thermocouple. The main purpose for using a heat pipe is to make and maintain a thin solid crust around the heat pipe while it is in operation. This solid crust having the same chemical composition as the slag can protect the thermocouple from corrosion that normally occurs around the slag line. The characteristics of such a heat pipe have been studied and will be discussed in subsequent chapters of this thesis.

Chapter 2

Inverse Heat Conduction Approach

2.1 Introduction

If the heat flux or temperature at the boundary is known, then the temperature distribution in a region can be calculated and this can be termed a *direct problem.* In *inverse problems*, the surface heat flux and temperature can be determined from the interior temperature at one or more locations. This method can be used to estimate heat flux and temperature histories when it is difficult to place a sensor on the boundary, or when the accuracy of the measurement can be deteriorated by the presence of the sensor.

A typical example is the estimation of surface heat transfer of the reentry vehicle from space with measurements taken within the skin of the vehicle. Some work has been directed toward application to the space program by Blackwell[33], Imber[34, 35, 36], and Mulholland[37, 38]. Some other applications published for inverse heat conduction problems(IHCP) include periodic heating in combustion chambers of internal combustion engines[39], solidification of glass[40], and indirect calorimetry for lab use[41]. The inverse heat conduction method can be used to determine the heat transfer coefficient[42] and thermophysical properties of materials[43]. One of the earliest papers on the inverse heat conduction problem was presented by Stolz [44] in 1960 and dealt with the calculation of heat transfer rates during quenching of bodies of simple shape. In his paper exact matching of the experimental and calculated temperatures was used. Thus Stolz's method is restricted to large time steps. J. V. Beck developed basic concepts of IHCP[45, 46, 47, 48, 49]. He changed Stolz's method by using future temperature in addition to past and present temperatures. The least squares technique was utilized to minimize the error between the calculated and measured temperatures. The addition of the future temperature increases the stability to the computational procedure and thus permits use of smaller time steps.

In order to be *well-posed* mathematically, a solution should exist, unique, and be continuously dependent on the data or equivalently, be stable. The inverse heat conduction problem is known to be an *ill-posed* problem mathematically because the solution is not stable. The inverse heat conduction problem is shown to be ill-posed by Beck[50] and Tikhonov[51].

Due to the diffusive nature of heat flow, changes in surface condition are damped in the interior. Thus, in IHCP, small errors in the measured internal temperatures are magnified at the surface and can cause oscillation in calculated surface conditions. As the distance between the surface and sensor locations increases these oscillations increase. By using a large time step or a low-order linear model, stability of the finite difference and finite element techniques can be improved even though the resolving power is degraded.

Numerous methods have been presented to reduce the sensitivity to measurement errors. The methods for solving inverse heat conduction can be classified in several ways. Two basic algorithms are function specification and regularization methods. Methods for solving the conduction equation can be used to classify the IHCP and include the use of finite differences, finite elements and finite control volumes. IHCP is also classified by the time domain utilized. Three time domains have been proposed: only to the present time, to the present time plus a few future time steps, and the complete time domain. J. V. Beck gave some criteria for comparison between many methods[49] and some methodology for comparison of inverse heat conduction methods[52].

In the function specification method, a functional form for the unknown heat flux is assumed. The functional form contains a number of unknown parameters that are estimated by the least squares. A number of authors have used the function specification method[46, 48, 53, 54, 55]. Regularization method is a procedure which modifies the least squares approach by adding factors that are intended to reduce the fluctuation in the unknown functions such as surface heat flux. The regularization method has a number of forms and has been studied by many researchers including Tikhonov and Arsenin[51], Alifanov[56, 57], Bell[58, 59], and Beck and Murio[60].

2.2 1-D Rectangular Model

2.2.1 Mathematical Model

In the present study, a method called *exact matching of data*[50] was adopted. If one considers a temperature sensor located in the interior of an object, then the value of heat flux that forces a matching of the computed temperature at the location of the sensor with the measured temperature can be calculated. This approach is simple in concept and development, but the disadvantage is that it produces oscillations in the calculated heat flux if a relatively small time step is used. The model is based on the finite difference formulation of Fourier's heat conduction equation.

(A) Internal node i

For heat conduction the heat transfer process equation is known as Fourier's law. For a one dimensional plane wall having a temperature distribution $T(x)$, Fourier's equation is expressed as

$$\dot{q}'' = -k\frac{dT}{dx_n} \tag{2.1}$$

where x_n is a coordinate direction and $\dot{q}''$ is the conduction heat transfer flux per unit area and unit time (W/m^2).

For the rectangular coordinate system(x, y, z) the heat conduction equation is

$$\frac{\partial^2 T}{\partial x^2} + \frac{\partial^2 T}{\partial y^2} + \frac{\partial^2 T}{\partial z^2} + \frac{\dot{q}'''}{k} = \frac{1}{\alpha}\frac{\partial T}{\partial t} \tag{2.2}$$

where $T = T(x, y, z, t)$ and $\dot{q}'''$ is rate of energy generation per unit volume. From Eq. (2.2) the one dimensional heat conduction equation without an internal heat source can be written as

$$\frac{\partial^2 T}{\partial x^2} = \frac{1}{\alpha}\frac{\partial T}{\partial t} \tag{2.3}$$

Exact solutions of Eq. (2.3) with appropriate boundary conditions are normally difficult to arrive at - thus numerical techniques will be used. The first step in establishing a finite difference procedure for solving a partial differential equation is to replace the continuous problem domain by a finite difference mesh or grid as shown in Figure 2.1.

The idea of a finite difference representation for a derivative can be introduced by the definition of the derivative for the function $T(x)$ at $x = x_o$

$$\left.\frac{\partial T}{\partial x}\right|_{x=x_o} = \lim_{\Delta x \to 0} \frac{T(x_o + \Delta x) - T(x_o)}{\Delta x} \tag{2.4}$$

If $T(x)$ is continuous, $(T(x_o + \Delta x) - T(x_o))/\Delta x$ will be a *reasonable* approximation to $\partial T/\partial x$ for a sufficiently small but finite Δx.

The difference approximation can also be obtained using the Taylor-series expansion. Let $T(x)$ be a function that can be expanded in Taylor-series, the series expansion of the function $T(x_o + \Delta x)$ is given as

$$\begin{aligned} T(x_o + \Delta x) = T(x_o) + \left.\frac{\partial T}{\partial x}\right|_{x=x_o} \Delta x + \left.\frac{\partial^2 T}{\partial x^2}\right|_{x=x_o} \frac{(\Delta x)^2}{2!} + \cdots \\ + \left.\frac{\partial^{n-1} T}{\partial x^{n-1}}\right|_{x=x_o} \frac{(\Delta x)^{n-i}}{(n-1)!} + \left.\frac{\partial^n T}{\partial x^n}\right|_{\xi} \frac{(\Delta x)^n}{n!} \\ x_o \leq \xi \leq x_o + \Delta x \end{aligned} \tag{2.5}$$

where the last term can be termed the remainder. We can get the *forward* difference by rearranging Eq. (2.5) such that

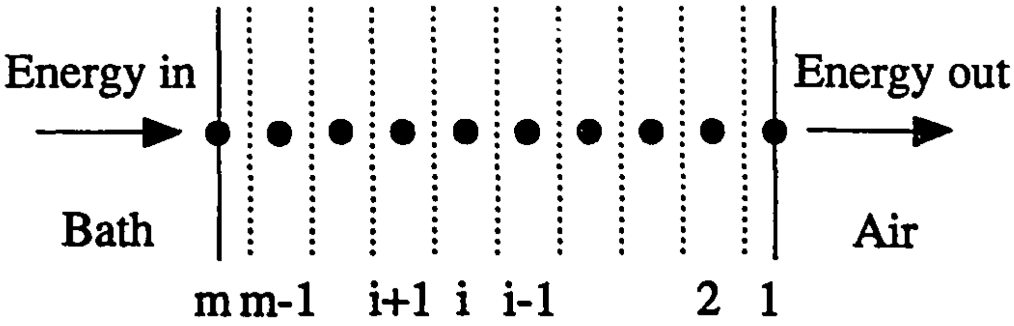

Figure 2.1: Schematic distribution of nodal points in 1-D section.

$$\left.\frac{\partial T}{\partial x}\right|_{x=x_o} = \frac{T(x_o+\Delta x)-T(x_o)}{\Delta x} - \left.\frac{\partial^2 T}{\partial x^2}\right|_{x=x_o}\frac{(\Delta x)}{2!} - \cdots \tag{2.6}$$

After switching the notation, Eq. (2.6) can be written as

$$\left.\frac{\partial T}{\partial x}\right|_{i} = \frac{T_{i+1}-T_i}{\Delta x} + \text{Truncation error} \tag{2.7}$$

The truncation error is the error between the derivative and its finite difference representation. The limit of truncation error can be characterized by using the order of (O) notation such as

$$\left.\frac{\partial T}{\partial x}\right|_{i} = \frac{T_{i+1}-T_i}{\Delta x} + O(\Delta x) \tag{2.8}$$

$O(\Delta x)$ means |truncation error| $\leq K\,|\Delta x|$ for $\Delta x \to 0$ (sufficiently small Δx) where K is a positive real constant.

Taylor-series expansion of $T(x)$ at $x = x_o - \Delta x$ can be written as

$$\begin{aligned} T(x_o-\Delta x) = T(x_o) - \left.\frac{\partial T}{\partial x}\right|_{x=x_o}\Delta x + \left.\frac{\partial^2 T}{\partial x^2}\right|_{x=x_o}\frac{(\Delta x)^2}{2!} \\ - \left.\frac{\partial^3 T}{\partial x^3}\right|_{x=x_o}\frac{(\Delta x)^3}{3!} + \cdots \end{aligned} \tag{2.9}$$

The *backward* difference can be obtained from Eq. (2.9) and using the same notation as Eq. (2.7) such that

$$\left.\frac{\partial T}{\partial x}\right|_i = \frac{T_i - T_{i-1}}{\Delta x} + O(\Delta x) \qquad (2.10)$$

By subtracting Eq. (2.9) from Eq. (2.5) and rearranging, the *central* difference can be obtained

$$\left.\frac{\partial T}{\partial x}\right|_i = \frac{T_{i+1} - T_{i-1}}{2\Delta x} + O(\Delta x)^2 \qquad (2.11)$$

We note that forward and backward differences are accurate to the order of (Δx) whereas the central-difference expansion is accurate to the order of $(\Delta x)^2$. We can add Eq. (2.9) and Eq. (2.5) to arrive at an approximation to the second derivative. Thus

$$\left.\frac{\partial^2 T}{\partial x^2}\right|_i = \frac{T_{i+1} - 2T_i + T_{i-1}}{(\Delta x)^2} + O(\Delta x)^2 \qquad (2.12)$$

To obtain a series of the finite difference form of Eq. (2.3), space(i.e. x) and time(i.e. t) domains are divided into small steps of Δx and Δt size respectively as shown in Figure 2.2. Thus,

$$\begin{aligned} x &= (i-1)\Delta x && \text{for } i = 2, 3, \ldots, m-1 \\ t &= n\Delta t && \text{for } n = 0, 1, 2, \ldots \end{aligned}$$

The second derivative of temperature with respect to x at position i and at time $(n+1)\Delta t$ can be written as

$$\left.\frac{\partial^2 T}{\partial x^2}\right|_{i,n+1} \cong \frac{T_{i+1}^{n+1} - 2T_i^{n+1} + T_{i-1}^{n+1}}{(\Delta x)^2} \qquad (2.13)$$

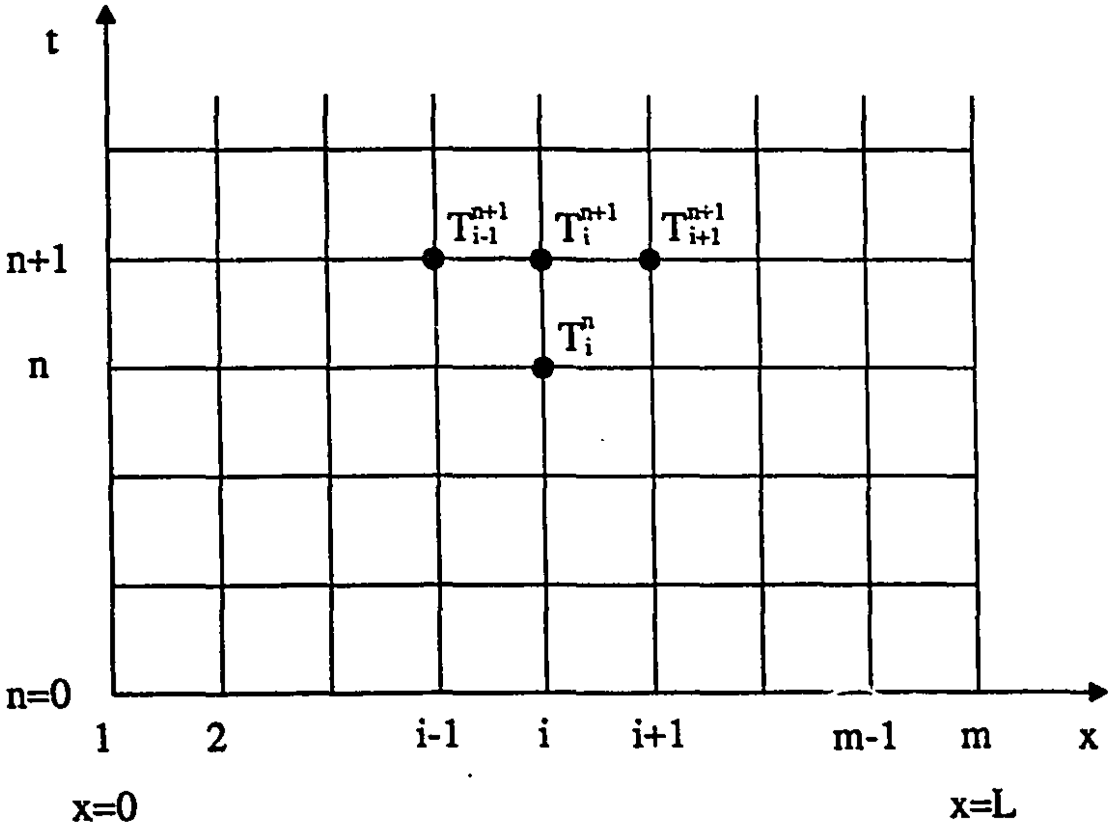

Figure 2.2: Subdivision of the x-t domain into intervals Δx and Δt for finite difference representation of the one dimensional time-dependent heat conduction equation.

The first derivative of temperature with respect to the time variable t at position i and at time $(n+1)\Delta t$ is represented in finite difference form using the backward difference expression as

$$\left.\frac{\partial T}{\partial t}\right|_{i,n+1} \cong \frac{T_i^{n+1} - T_i^n}{(\Delta t)} \tag{2.14}$$

By incorporating Eqs. (2.13) and (2.14) into Eq. (2.3), the finite difference formulation of the one-dimensional time-dependent heat conduction equation is given by

$$\frac{T_i^{n+1} - T_i^n}{\Delta t} = \alpha \frac{T_{i+1}^{n+1} - 2T_i^{n+1} + T_{i-1}^{n+1}}{(\Delta x)^2} \tag{2.15}$$

This equation represents a formulation of the *implicit* finite difference scheme. Solution of T_i^{n+1} for $i = 2, 3, \ldots, m-1$ at the (n+1)th time step requires that a set of simultaneous algebraic equations be solved. An alternative to the implicit scheme is the explicit formulation whereby as the name implies, T_i^{n+1} can be obtained from one equation *explicitly* without having to solve simultaneously a series of equations. Moreover it requires that certain stability criteria be satisfied. The advantage of the implicit scheme is that it is stable for all time steps Δt. It has the first-order accuracy with a truncation error of $O\left[\Delta t, (\Delta x)^2\right]$.

After rearranging Eq. (2.15) and substituting the notation given by Eq. (2.17), the following expression is obtained

$$M\theta'_{i-1} - (1+2M)\theta'_i + M\theta'_{i+1} = -\theta_i \tag{2.16}$$

for $2 \leq i \leq m-1$ where

θ_i = Temperature of node i at time t

θ'_i = Value of θ_i at $t + \Delta t$

$$M = \alpha \frac{\Delta t}{(\Delta x)^2} \tag{2.17}$$

M is called the Fourier number based on a time-space grid.

(B) Surface nodes m and 1

For surface nodes, it is normally wiser especially if convection and/or radiation are involved to consider the overall energy balance from which Eq. (2.3) was derived. The energy balance for surface node m yields the expression given by Eq. (2.18) with the convention that energy flows from node m to node 1.

$$\begin{pmatrix} \text{Rate of energy} \\ \text{into node } m \end{pmatrix} - \begin{pmatrix} \text{Rate of energy} \\ \text{out of node } m \end{pmatrix}$$

$$+ \begin{pmatrix} \text{Rate of energy} \\ \text{generated in node } m \end{pmatrix} = \begin{pmatrix} \text{Rate of energy} \\ \text{accumulated in} \\ \text{node } m \end{pmatrix}$$

or

$$\dot{q}''_{in} A - \dot{q}_{m \to m-1} + \dot{q}'''_m V_m = \rho_m C_m V_m \frac{\theta'_m - \theta_m}{\Delta t} \tag{2.18}$$

where: V_m = Volume of node m

ρ_m = Density of node m

C_m = Heat capacity of node m

θ_m = Temperature of node m at time t

θ'_m = Value of θ_m at $t + \Delta t$

Δt = Iterative time increment

$\dot{q}''_{in}$ = Heat flux into node m per unit area and time

$\dot{q}'''_m$ = Rate of heat generation per unit volume in node m

From Fourier's law of heat conduction the heat flow rate can be approximated as

$$\dot{q}_{m\to m-1} = k_{m\to m-1}A\frac{\theta'_m - \theta'_{m-1}}{\Delta x} \tag{2.19}$$

Substituting Eq. (2.19) into Eq. (2.18) yields

$$\dot{q}''_{in}A - k_{m\to m-1}A\frac{\theta'_m - \theta'_{m-1}}{\Delta x} = \rho_m C_m V_m \frac{\theta'_m - \theta_m}{\Delta t} \tag{2.20}$$

where $V_m = A \times \Delta x/2$. By dividing by $\rho_m C_m V_m/\Delta t$, Eq. (2.20) can be written as follows assuming $k_{m\to m-1} = k$, $\rho_m = \rho$ and $C_m = C$.

$$\frac{\dot{q}''_{in}A\Delta t}{\rho C V_m} - \frac{kA\Delta t}{\rho C V_m \Delta x}(\theta'_m - \theta'_{m-1}) = \theta'_m - \theta_m \tag{2.21}$$

After rearranging, substitution of Eq. (2.17) into Eq. (2.21) gives

$$\frac{2\Delta t}{\Delta x}q_{in} - (1 + 2M)\theta'_m + 2M\theta'_{m-1} = -\theta_m \tag{2.22}$$

where $q_{in} = \dot{q}''_{in}/\rho C$

Same energy balance can be applied to outer surface node 1 to produce the expression given by Eq. (2.23)

$$k_{2\to1}A\frac{\theta'_2-\theta'_1}{\Delta x} - \dot{q}''_{out}A = \rho C V_1\frac{\theta'_1-\theta_1}{\Delta t} \tag{2.23}$$

Substitution of Eq. (2.17) into Eq. (2.23) gives the following

$$2M\theta'_2 - (1+2M)\theta'_1 - \frac{2\Delta t}{\Delta x}q_{out} = -\theta_1 \tag{2.24}$$

where $q_{out} = \dot{q}''_{out}/\rho C$.

q_{in} in Eq. (2.22) represents a modified form of the heat flux from the bath to the test piece and can be written as

$$q_{in} = \frac{h}{\rho C}(\theta'_b - \theta'_m) = H(\theta'_b - \theta'_m) \tag{2.25}$$

where: h = Heat transfer coefficient

ρ = Density of the test piece

C = Heat capacity of the test piece

θ'_b = Bath temperature at time $t + \Delta t$

θ'_m = Temperature of node m(wall) at time $t + \Delta t$

H = Constant $(h/\rho C)$

It is to be noted that the implicit finite difference formulation was adopted for the present analysis. Two actual thermocouple measurements at known locations within the test piece are expressed mathematically as follows

$$\theta_j' = \text{measured temperature at node } j \tag{2.26}$$

$$\theta_k' = \text{measured temperature at node } k \tag{2.27}$$

By solving Eqs. (2.16), (2.22) and (2.24) with the above two equations, unknown temperatures at each $(m - 2)$ nodes, q_{in} as well as q_{out} can be computed. Assuming a 10 node system, 10 equations from Eqs. (2.16), (2.22) and (2.24) and two actual thermocouple measurements at nodes 8 and 9 can be written in matrix form so that

$$\mathbf{A} \times \mathbf{X} = \mathbf{B} \tag{2.28}$$

where

$$\mathbf{A} = \left[\begin{array}{cccccccccccc}
d & 2M & & & & & & & & & & -N1 \\
M & d & M & & & & & & & & & \\
 & M & d & M & & & & & & & & \\
 & & M & d & M & & & & & & & \\
 & & & M & d & M & & & & & & \\
 & & & & M & d & M & & & & & \\
 & & & & & M & d & M & & & & \\
 & & & & & & M & d & M & & & \\
 & & & & & & & M & d & M & & \\
 & & & & & & & & 2M & d & N1 & \\
 & & & & & & & 1 & & & & \\
 & & & & & & & & 1 & & &
\end{array}\right]$$

and where $d = -(1 + 2M)$, $N1 = 2\Delta t/\Delta x$ and

$$\mathbf{X} = \begin{bmatrix} \theta'_1 \\ \theta'_2 \\ \theta'_3 \\ \theta'_4 \\ \theta'_5 \\ \theta'_6 \\ \theta'_7 \\ \theta'_8 \\ \theta'_9 \\ \theta'_{10} \\ q_{in} \\ q_{out} \end{bmatrix} \qquad \mathbf{B} = -\begin{bmatrix} \theta_1 \\ \theta_2 \\ \theta_3 \\ \theta_4 \\ \theta_5 \\ \theta_6 \\ \theta_7 \\ \theta_8 \\ \theta_9 \\ \theta_{10} \\ -m_8 \\ -m_9 \end{bmatrix}$$

$\theta'_1, \cdots, \theta'_{10}$ contain the temperatures of each of the nodes at time $t + \Delta t$. $\theta_1, \cdots, \theta_{10}$ represent the temperatures of the nodes at time t. m_8 and m_9 represent measured temperatures at nodes 8 and 9 respectively.

At the start of the analysis θ'_b is measured with an immersion thermocouple and input to the model. In this way H, a parameter lumping the heat transfer coefficient of the system is evaluated with Eq. (2.25) and its value used in subsequent analyses. Once H is known, the bath temperature, θ'_b, is computed by substituting θ'_m and q_{in} into Eq. (2.25). It is worth noting that θ'_m and q_{in} are determined by solving the set of simultaneous equations as given by Eq. (2.28).

Another section of the model is used to calculate thermal diffusivity(α) as a function of temperature. Rearranging Eq. (2.16) and substituting Eq. (2.17) gives

$$\alpha = \frac{\Delta x^2}{\Delta t} \frac{\theta'_i - \theta_i}{\theta'_{i-1} - 2\theta'_i + \theta'_{i+1}} \tag{2.29}$$

Thus, thermal diffusivity (α) as a function of temperature can be computed from a knowledge of the three temperatures as measured by thermocouples located at equal spacings in the test section. Upon substitution of these readings into Eq. (2.29), a value for α was produced. This value was taken to represent the thermal diffusivity at an average temperature of θ'_i. But it should be noted that the basic assumption of deriving Eq. (2.29) is that the heat transfer is in transient mode. Thus Eq. (2.29) is no longer valid at steady state. In this way it was possible to compute thermal diffusivity data for a transient heat transfer system.

2.2.2 Experimental

Experiments with water

A schematic of the experimental apparatus appears in Figure 2.3. The test tank was made of sheet metal and measured 20 × 30 × 30 cm. The front side of the tank was replaced by a plexi-glass plate 2.1 cm in thickness. Three type K thermocouples were located in the plexi-glass plate 0.42, 0.63 and 0.84 cm away from the interface between the plexi-glass and the water. A fourth thermocouple was located in the tank to measure the bath temperature. All thermocouples were connected to a H.P. 3497A data acquisition/control unit. The water in the return reservoir was heated. When the water reached its boiling point, it was pumped up to the feed reservoir. Data acquisition was started after the test tank was full.

Data acquisition was controlled by a HP 85A microcomputer. The microcomputer permitted the storing of data onto a floppy disk and the subsequent processing of data followed by plotting.

In another set of low temperature experiments, the test tank was changed

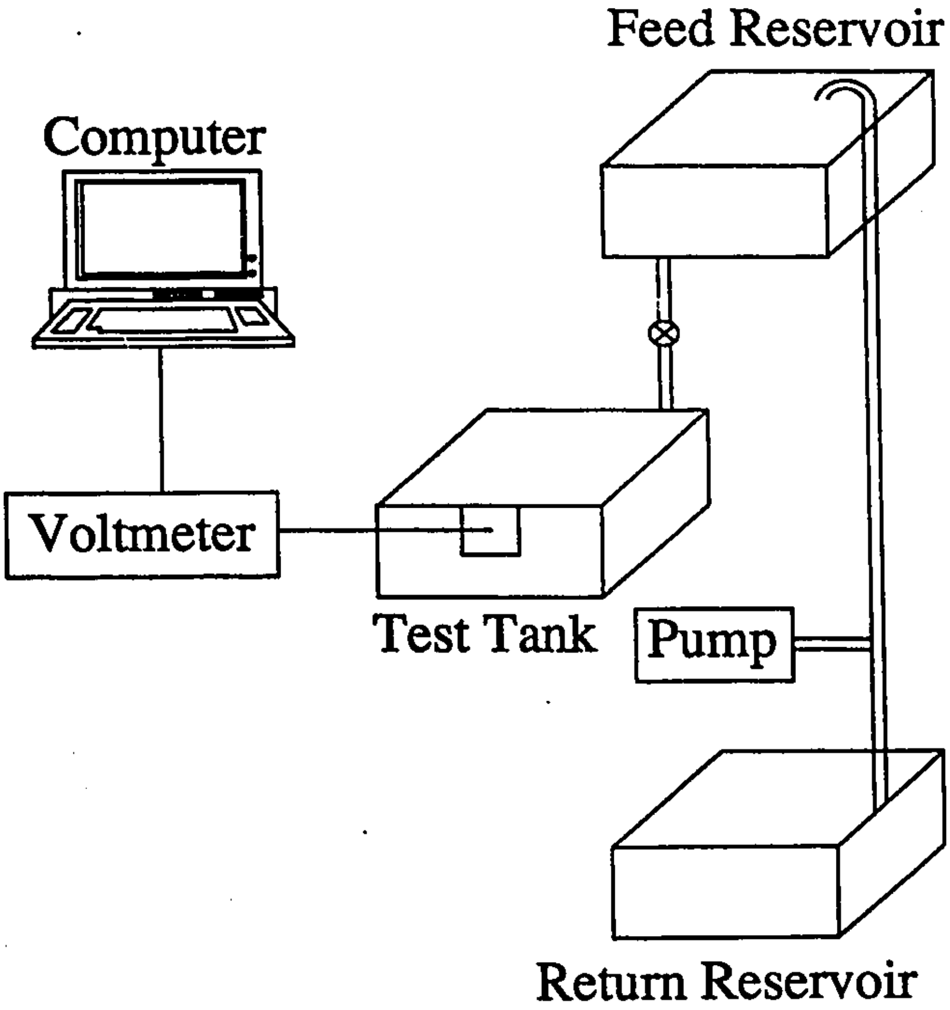

Figure 2.3: Schematic of water model test apparatus.

slightly such that the plexi-glass, in which thermocouples were embedded, was placed on top of the water and supported by steel wire in order to test the model with a different configuration. Plexi-glass plate measured 14 × 19 cm and 2.1 cm in thickness. Three K type thermocouples were embedded in the plexi-glass plate 0.42, 0.63 and 0.84 cm away from the interface between plexi-glass and hot water. The same procedure as adopted for the previous series of experiments was followed to acquire temperature data.

Experiments with aluminum

In addition to the experiments involving water, a series of high temperature laboratory experiments with molten aluminum were carried out to test the model at high temperatures. In another set of tests, the same mathematical algorithm, as expressed by Eq. (2.29), was used to compute thermal diffusivity data for refractory brick. As mentioned in the previous section, the heat flow in the test brick must be in transient mode to enable the calculation of thermal diffusivity values using Eq. (2.29). In this case, transient heat transfer was achieved by replacing the door of a Lindberg furnace with the test brick in which three thermocouples were embedded. The test brick measured 11 × 11 cm and 6.4 cm in thickness. Three K-type thermocouples were located 0.5, 1 and 1.5 cm from the interface between the refractory brick and hot air. All thermocouples were connected to a H.P. 3497A data acquisition/control unit. Insulating brick pieces were put around the refractory brick to fit the furnace opening. When the temperature of the furnace reached about 1200 °C the furnace door was opened and replaced with the test brick assembly and data acquisition was started. This procedure was necessary only once to obtain thermal diffusivity data for the test specimen.

A series of high temperature laboratory experiments wherein aluminum was melted in a stainless steel vessel measuring 25 × 19 × 13.5 cm were also carried out. Insulating brick was added to the inside wall of the container to make it reusable. The top of the container was left uncovered to allow the aluminum to melt quickly. One of the steel walls was replaced with refractory brick in which thermocouples were embedded. The refractory brick measured 12 × 13 × 6.4 cm. Insulating brick pieces were put around the test brick to achieve 1-D heat flow by preventing heat flow from the side wall. Three type K thermocouples were placed in the refractory brick 0.5, 1.0 and 1.5 cm from the interface between the refractory brick and the molten aluminum. A thermocouple was inserted in the molten aluminum bath through the brick to monitor bath temperature. Once all the aluminum was fully molten, data acquisition was started and controlled by the microcomputer. Same procedure as previous experiments was followed to acquire the temperature data.

2.2.3 Results and Discussions

Calculation of thermal diffusivity

The thermal diffusivities(α) of plexi-glass, 70 % alumina brick and magnesite brick were computed using Eq. (2.29). The results for plexi-glass are shown plotted in Figure 2.4. Figure 2.5 and Figure 2.6 present the results obtained for the alumina and magnesite bricks. In all cases the thermal diffusivity is presented as a function of temperature.

Individual values for the thermal diffusivity of plexi-glass were obtained from the readings of 3 thermocouples embedded in a plexi-glass sheet that was contacted by hot water. Upon substitution of these readings into Eq. (2.29), a value for α was produced. This value was taken to represent the thermal diffusivity at an average temperature of θ_i'. In this way it was possible to compute thermal diffusivity data for a transient heat transfer system. Some of the properties of plexi-glass(polymethyl methacrylate) at 25 °C are listed by D. Van Krevelen[61] as follows.

$$\begin{aligned} \rho &= 1170 \ \ kg/m^3 \\ C_p &= 1380 \ \ J/kg\,^{\circ}C \\ k &= 0.193 \ \ W/m\,^{\circ}C \end{aligned}$$

Thus the calculated thermal diffusivity($\alpha = k/\rho C_p$) of the plexi-glass given the above properties is 1.19×10^{-7} m^2/s. A value of 1.14×10^{-7} m^2/s was obtained by extrapolating the least square curve fitted line shown in Figure 2.4.

The same mathematical algorithm, as expressed by Eq. (2.29) was used to compute thermal diffusivity data for refractory brick. Even though the furnace was set at 1200 °C, the maximum temperature reached in the refractory brick at node i was far lower than that of the furnace. As the temperature attained its maximum value, heat transfer approached steady state behaviour. Under this scenario it was no longer possible to compute α with Eq. (2.29). For this reason the thermal diffusivity could only be calculated up to about 500 °C. Examination of the thermal diffusivity data presented in Figure 2.5 for the 70% alumina brick shows that at temperatures beyond about 400 °C, the natural logarithm of α appears to vary linearly with temperature and at only a relatively modest rate. Figure 2.6 shows that the natural logarithm of α for magnesite brick varies linearly with temperature beyond about 150 °C. These linear data were fit with the least squares method and the resulting

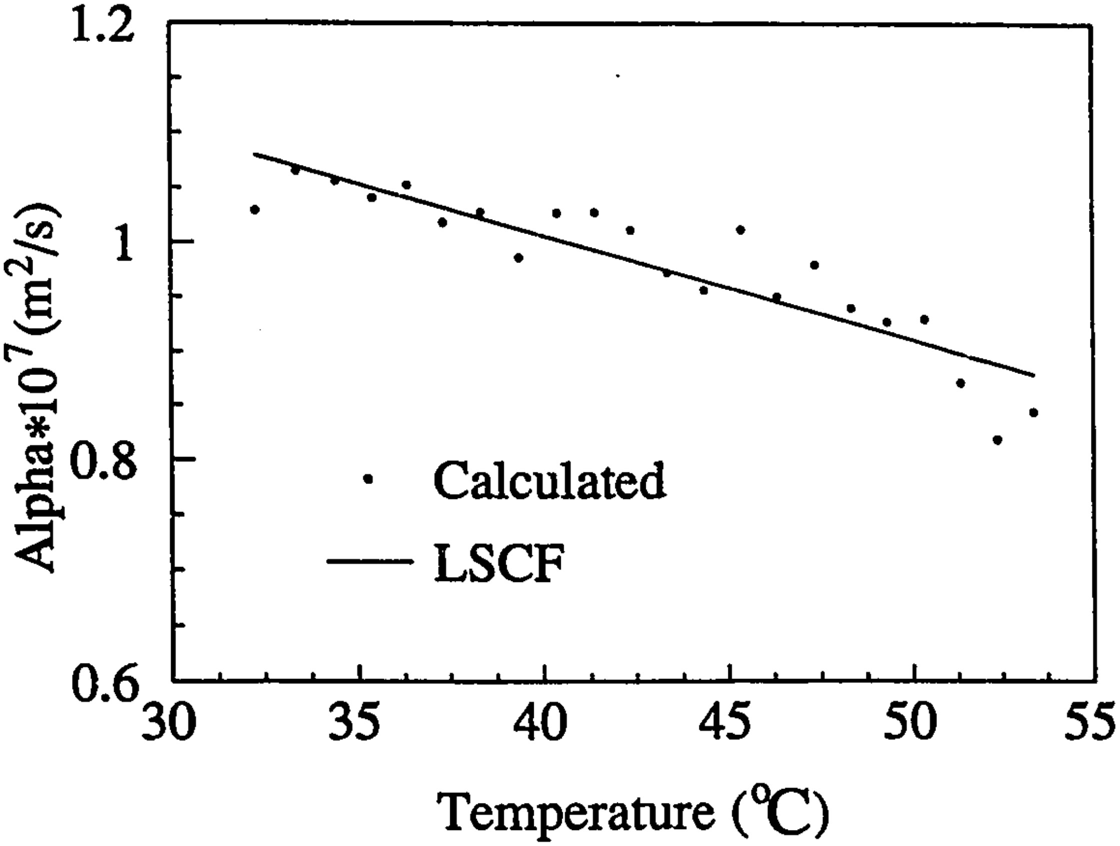

Figure 2.4: Thermal diffusivity (m^2/s) for plexi-glass plate.

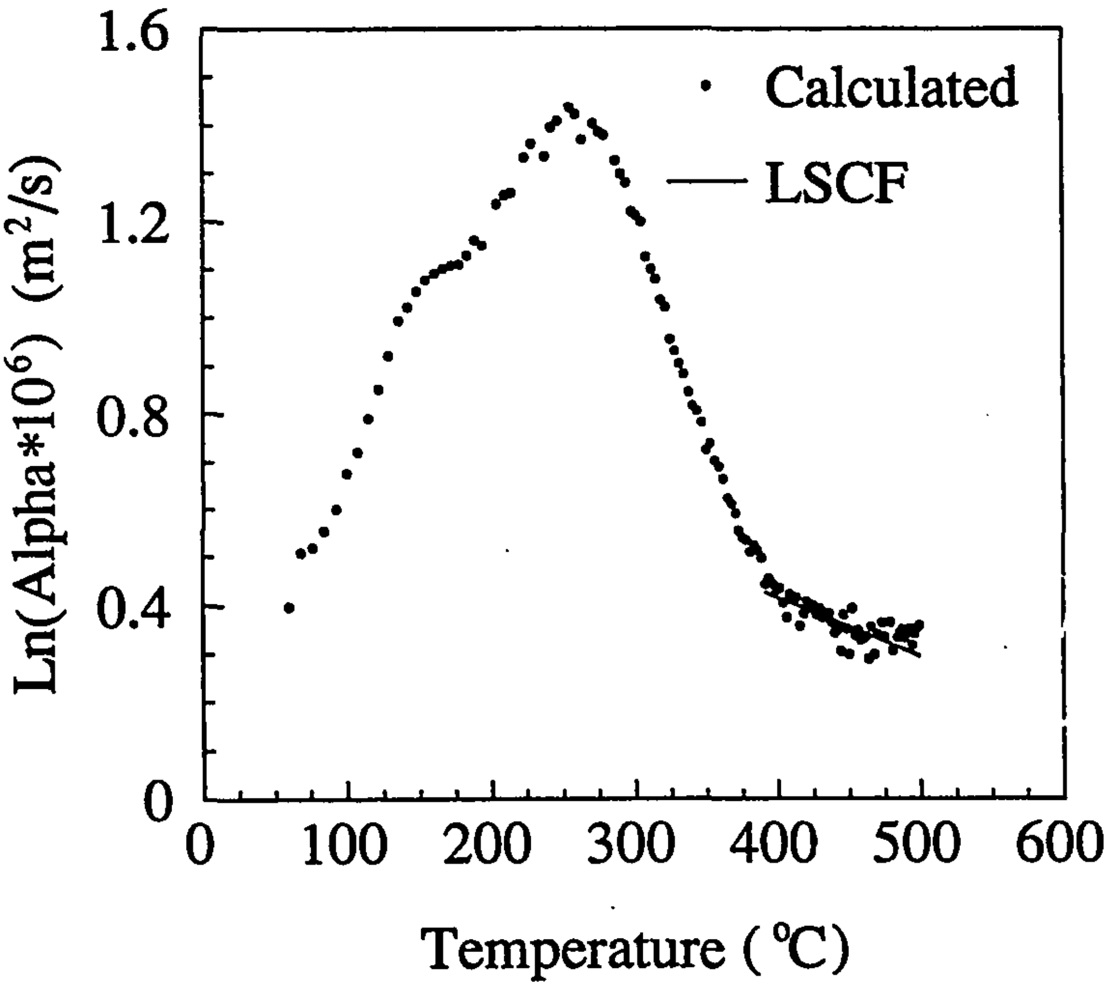

Figure 2.5: Temperature dependence of the thermal diffusivity (m^2/s) for 70% alumina brick.

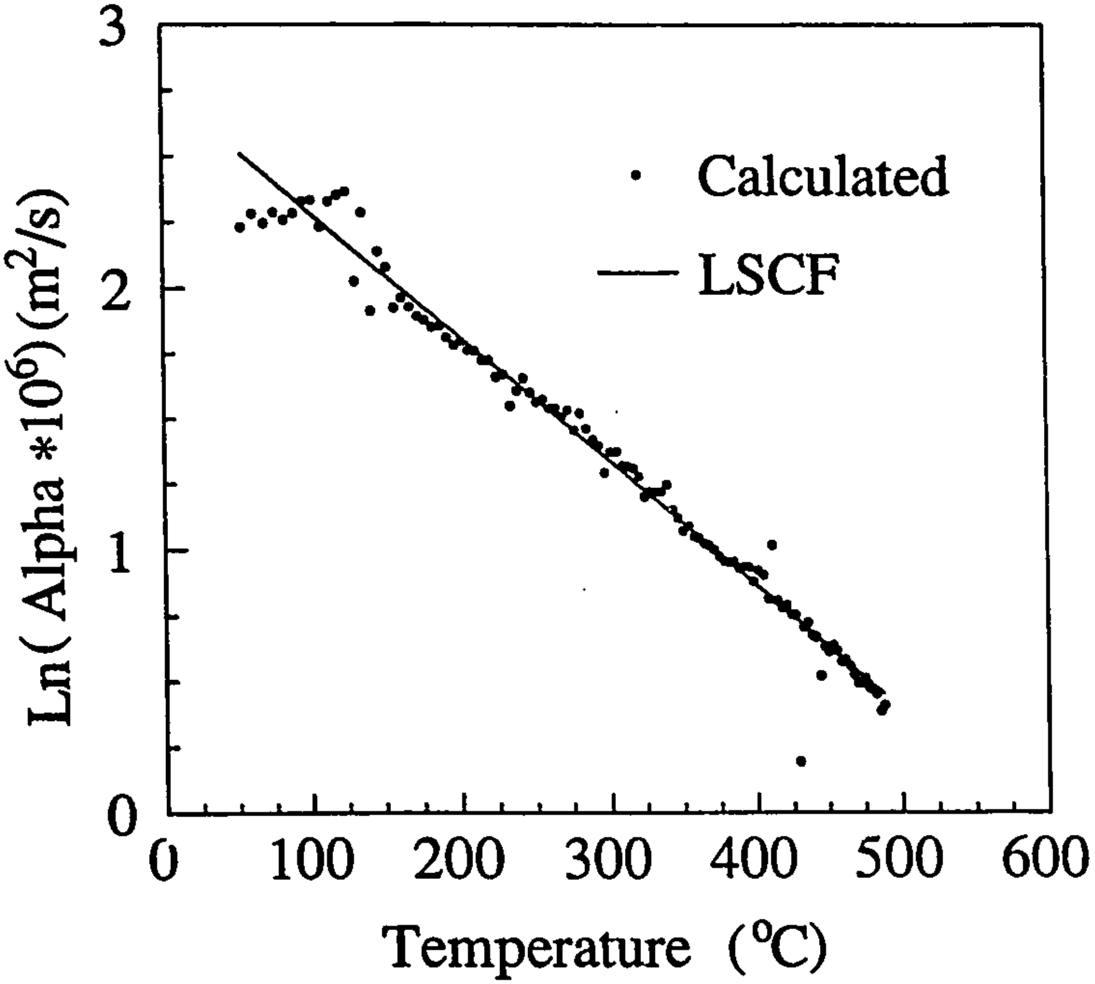

Figure 2.6: Temperature dependence of the thermal diffusivity (m^2/s) for magnesite brick.

equations were used to extrapolate values for α beyond the temperature range that was investigated.

Experiments with water

Test piece in vertical position

The low temperature water model described in the preceding section was tested extensively. Results showing actual measurements of bath temperature compared to computed bath temperatures are presented in Figure 2.7. As can be seen in this figure, there are fluctuations in the calculated temperatures. If a relatively small time step is used(e.g. 10 seconds in this case), then oscillations are produced in the calculated values due to the nature of the IHCP procedure. As the time step is increased to 20, 30, and 50 seconds, as shown in Figures 2.8, 2.9, and 2.10, the amplitude of the oscillations in the calculated values diminishes noticeably. However, if the time step is too large, the degree of resolution is lost in the analysis. A time increment of 30 seconds was found to be an optimal value that produced an acceptable compromise between oscillation and resolution. The computed bath temperature curves shown in Figures 2.7 to 2.10 were determined from Eq. (2.25) wherein H was assumed to be constant and not a function of temperature. To access the accuracy of each calculation using different time increments the error defined by Eq. (2.30) has been introduced

$$\text{Error} = \sum_{i=1}^{N} \frac{(T_{m,i} - T_{c,i})^2}{N} \tag{2.30}$$

where : $T_{m,i}$ = measured bath temperature

$T_{c,i}$ = calculated bath temperature

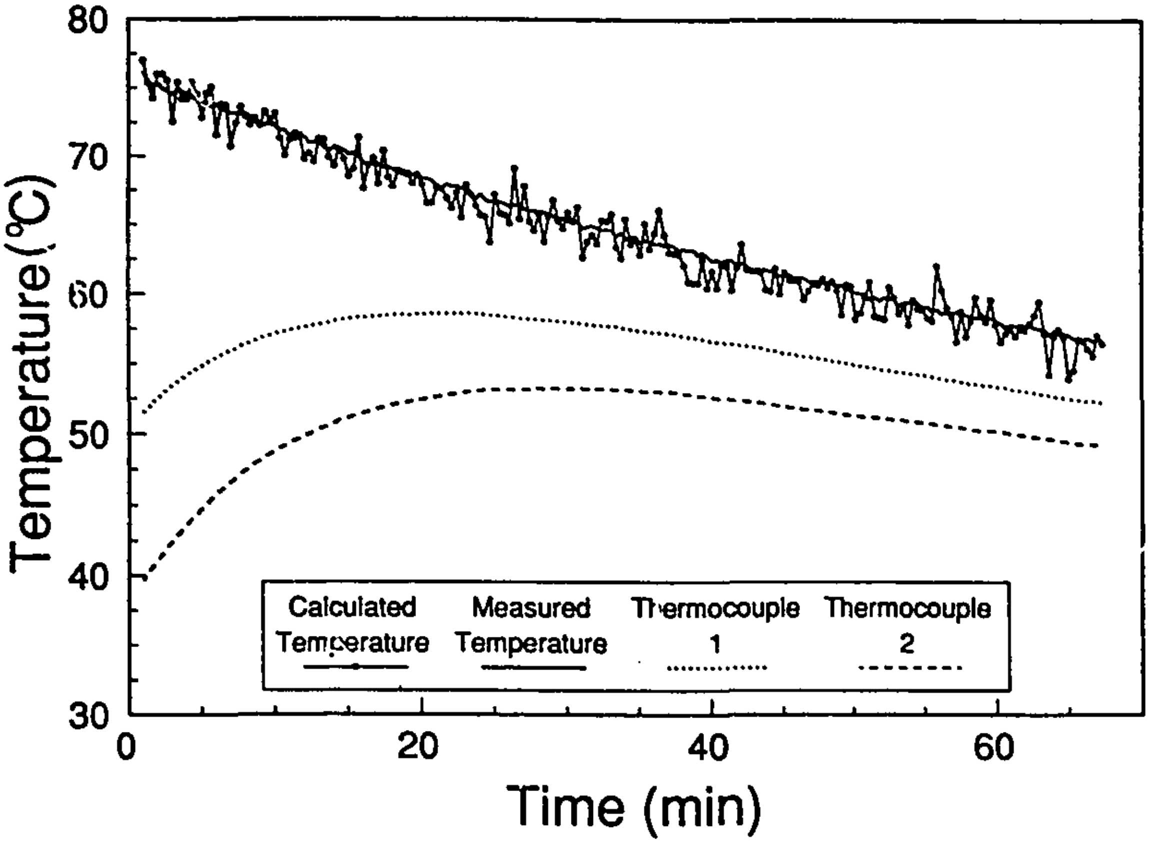

Figure 2.7: Computed and measured bath temperatures of water model experiment for vertical test piece when $\Delta t = 10$ sec. and $n = 0$.

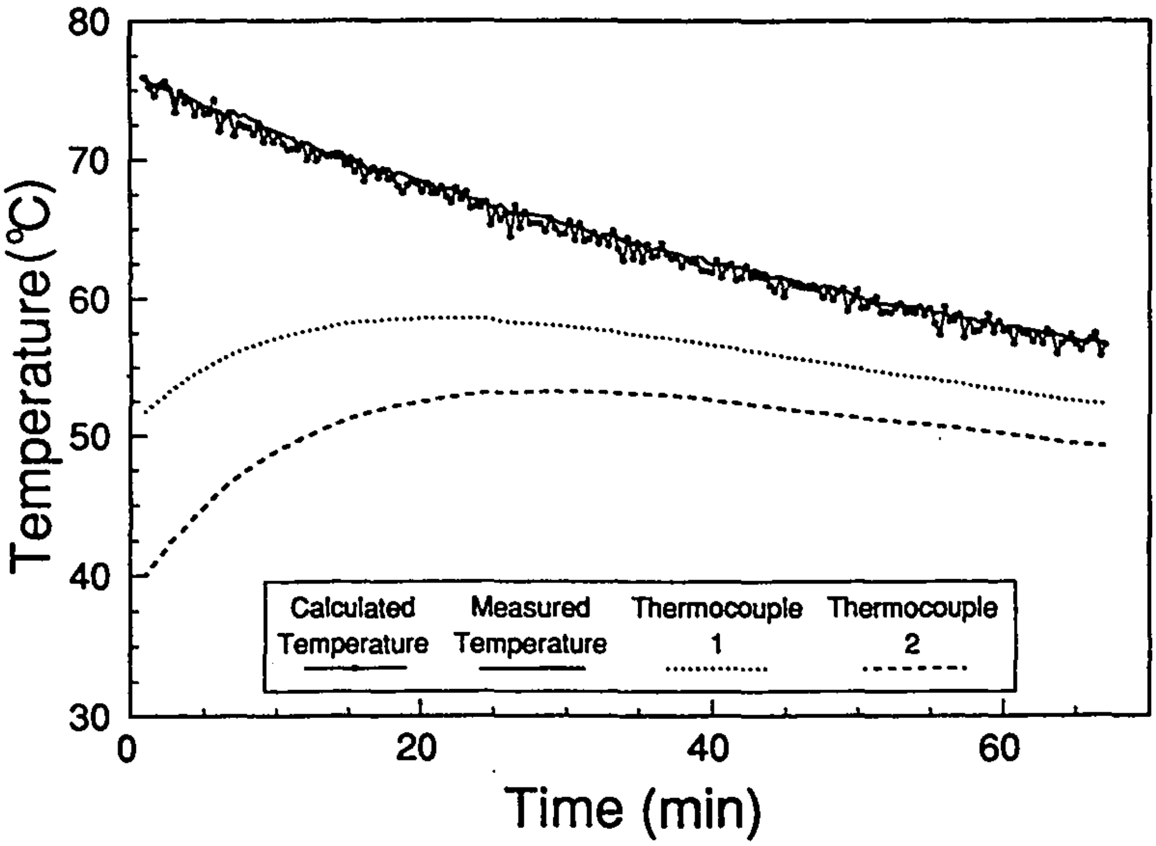

Figure 2.8: Computed and measured bath temperatures of water model experiment for vertical test piece when $\Delta t = 20$ sec. and $n = 0$.

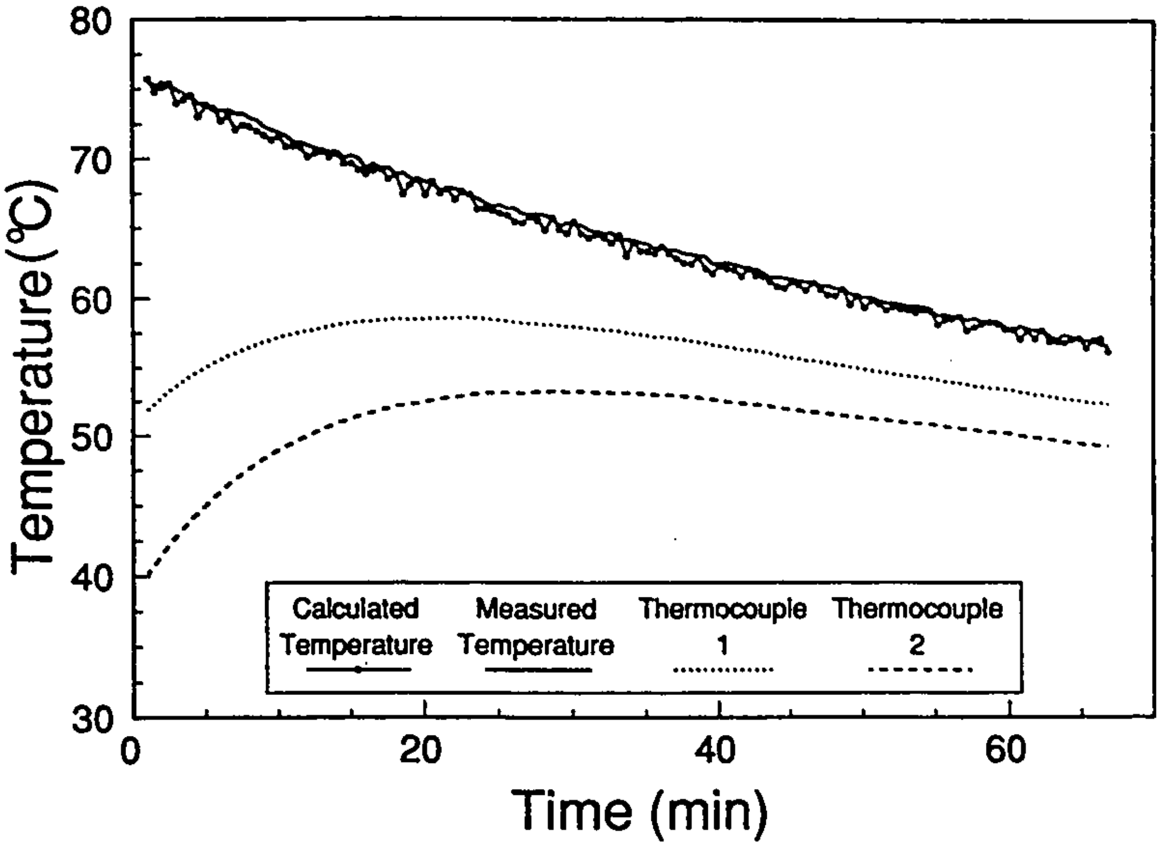

Figure 2.9: Computed and measured bath temperatures of water model experiment for vertical test piece when $\Delta t = 30$ sec. and $n = 0$.

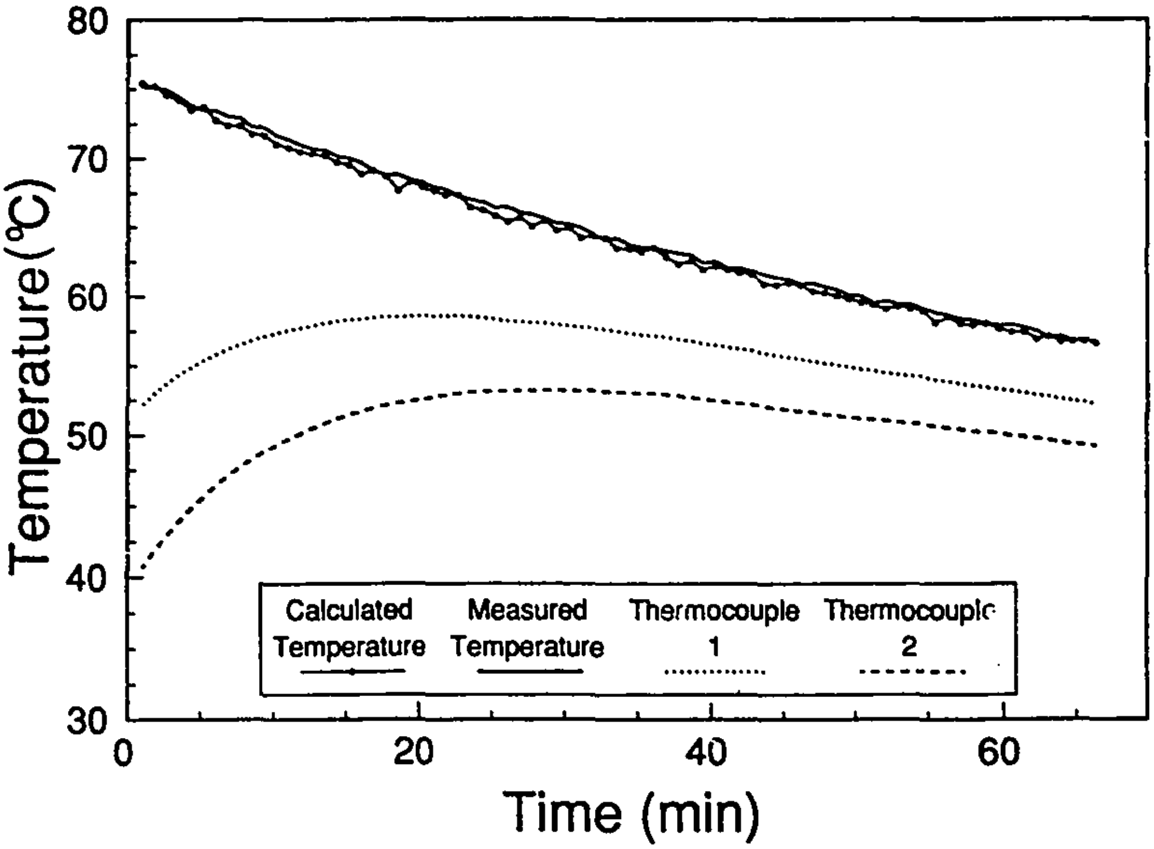

Figure 2.10: Computed and measured bath temperatures of water model experiment for vertical test piece when $\Delta t = 50$ sec. and $n = 0$.

N = total number of calculated data

As the time step is increased the error decreases as shown in Table 2.1.

Table 2.1: Calculated error for water model experiment with vertical test piece for different Δt's.

Δt	Error
10	1.43
20	0.387
30	0.269
40	0.223
50	0.209

However careful scrutiny of the results indicates that the model is overestimating H and thus underestimating the bath temperature. To find a more appropriate value of the heat transfer coefficient, the effect of natural convection which originates when a body force acts on a fluid in which there is a density gradient, should be taken into account. To find the factors affecting the convective heat transfer coefficient, consider a laminar boundary layer flow(Figure 2.11) which is driven by buoyancy forces originating from density variations assuming the following

- Laminar flow, steady state,
- plate and fluids are at constant temperature,
- boundary layer assumption valid,

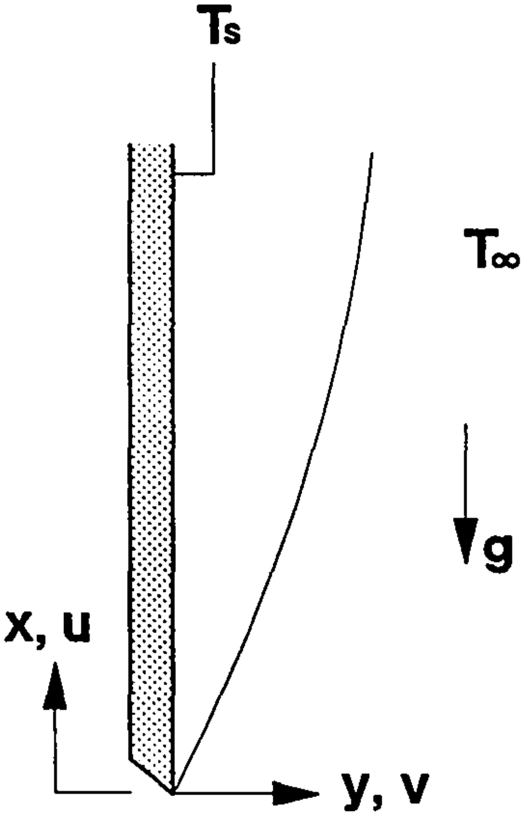

Figure 2.11: The laminar boundary layer for free convection on a vertical plate.

– density variations are important only in body force term.

Continuity equation, energy equation, and Navier-Stokes equations for steady state, constant property and 2-D flow can be written as

$$\frac{\partial u}{\partial x} + \frac{\partial v}{\partial y} = 0 \tag{2.31}$$

$$\rho\left(u\frac{\partial u}{\partial x} + v\frac{\partial u}{\partial y}\right) = -\frac{\partial p}{\partial x} + \mu\left[\frac{\partial^2 u}{\partial x^2} + \frac{\partial^2 u}{\partial y^2}\right] + \rho g_x \tag{2.32}$$

$$\rho\left(u\frac{\partial v}{\partial x} + v\frac{\partial v}{\partial y}\right) = -\frac{\partial p}{\partial y} + \mu\left[\frac{\partial^2 v}{\partial x^2} + \frac{\partial^2 v}{\partial y^2}\right] + \rho g_y \tag{2.33}$$

$$\rho C_p\left(u\frac{\partial T}{\partial x} + v\frac{\partial T}{\partial y}\right) = k\left[\frac{\partial^2 T}{\partial x^2} + \frac{\partial^2 T}{\partial y^2}\right] \tag{2.34}$$

where: u = velocity in x direction
v = velocity in y direction
p = fluid pressure
T = fluid temperature
C_p = heat capacity at constant pressure
g = gravitational constant
k = thermal conductivity
μ = dynamic viscosity
ρ = fluid density

From boundary layer analysis we know that

$$u \gg v$$

$$\frac{\partial^2 u}{\partial y^2} \gg \frac{\partial^2 u}{\partial x^2} \qquad \text{and} \qquad \frac{\partial^2 T}{\partial y^2} \gg \frac{\partial^2 T}{\partial x^2}$$

and $g_y = 0$, $g_x = -g$.

Thus Eqs. (2.31) - (2.34) can be simplified as

$$\frac{\partial u}{\partial x} + \frac{\partial v}{\partial y} = 0 \tag{2.35}$$

$$\rho\left(u\frac{\partial u}{\partial x} + v\frac{\partial u}{\partial y}\right) = -\frac{\partial p}{\partial x} + \mu\frac{\partial^2 u}{\partial y^2} - \rho g \tag{2.36}$$

$$\frac{\partial p}{\partial y} = 0 \tag{2.37}$$

$$\rho C_p\left(u\frac{\partial T}{\partial x} + v\frac{\partial T}{\partial y}\right) = k\frac{\partial^2 T}{\partial y^2} \tag{2.38}$$

From Eq. (2.37) pressure(p) is not a function of y. Thus $\partial p/\partial x$ can be written as dp/dx. From Eq. (2.36) dp/dx can be evaluated in the stagnant fluid far from the boundary layer, where $u = 0$. Thus,

$$\frac{\partial p}{\partial x} = -\rho_\infty g$$

The first and third term of the right hand side of Eq. (2.36) can be written as

$$-\frac{\partial p}{\partial x} - \rho g = (\rho_\infty - \rho)g \tag{2.39}$$

Density variation with respect to temperature can be treated by using the volumetric thermal expansion coefficient which is defined as

$$\beta = -\frac{1}{\rho}\left(\frac{\partial \rho}{\partial T}\right)_p \tag{2.40}$$

The thermal expansion coefficient can be approximated as

$$\beta \approx -\frac{1}{\rho}\left(\frac{\rho_\infty - \rho}{T_\infty - T}\right) \tag{2.41}$$

Thus Eq. (2.36) can be written as

$$u\frac{\partial u}{\partial x} + v\frac{\partial u}{\partial y} = \mu\frac{\partial^2 u}{\partial y^2} + g\beta(T - T_\infty) \tag{2.42}$$

with the following boundary conditions

$$\begin{array}{lll} y = 0 & u = v = 0 & T = T_s \\ y \to \infty & u \to 0 & T = T_\infty \end{array}$$

A similarity solution to this problem has been obtained by Ostarch[62] using the transformation of variables by introducing a similarity parameter

$$\eta \equiv \frac{y}{x}\left[\frac{1}{4}\frac{g\beta(T_s - T_\infty)x^3}{\nu^2}\right]^{1/4} \tag{2.43}$$

The velocity components can be represented with a stream function defined as

$$\psi(x, y) \equiv f(\eta)4\nu\left[\frac{1}{4}\frac{g\beta(T_s - T_\infty)}{\nu^2}\right]^{1/4} \tag{2.44}$$

and a dimensionless temperature parameter defined as

$$T^* \equiv \frac{T - T_\infty}{T_s - T_\infty} \tag{2.45}$$

The stream function $\psi(x, y)$ satisfies the continuity equation(Eq. (2.31)) and Eqs. (2.42) and (2.38) can be transformed into ordinary differential equations such that

$$\frac{d^3 f}{d\eta^3} + 3f\frac{d^2 f}{d\eta^2} - 2\left(\frac{df}{d\eta}\right)^2 + T^* \;=\; 0 \tag{2.46}$$

$$\frac{d^2 T^*}{d\eta^2} + 3\,Pr \cdot f \cdot \frac{dT^*}{d\eta} \;=\; 0 \tag{2.47}$$

with boundary conditions

$$\begin{array}{lll} \eta = 0 & f = \left.\frac{df}{d\eta}\right|_{\eta=0} = 0 & T^* = 1 \\ \eta \to \infty & \frac{df}{d\eta} = 0 & T^* = 0 \end{array}$$

A numerical solution has been obtained by Ostrach[62]. The local Nusselt number can be expressed as

$$Nu_x = \frac{hx}{k} = \frac{[\dot{q}_s''/(T_s - T_\infty)]x}{k} \tag{2.48}$$

Thus, the heat flow rate can be written as

$$\dot{q}_s'' = -k\left.\frac{\partial T}{\partial y}\right|_{y=0} = h(T_s - T_\infty) \tag{2.49}$$

Surface temperature gradient can be expressed with η and T^* from Eqs. (2.43) and (2.45) so that

$$\dot{q}_s'' = -k\,\frac{\partial T}{\partial y}\bigg|_{y=0} = \frac{k}{x}(T_\infty - T_s)\left(\frac{Gr_x}{4}\right)^{1/4}\frac{dT^*}{d\eta}\bigg|_{\eta=0} \qquad (2.50)$$

where

$$Gr_x = \frac{g\beta(T_s - T_\infty)x^3}{\nu^2}$$

Thus, the local Nusselt number can be rewritten as

$$Nu_x = \frac{hx}{k} = -\left(\frac{Gr_x}{4}\right)^{1/4}\frac{dT^*}{d\eta}\bigg|_{\eta=0} = \left(\frac{Gr_x}{4}\right)^{1/4} g(Pr) \qquad (2.51)$$

knowing that the dimensionless temperature gradient at the surface is only a function of Prandtl number(Pr).

The average convective heat transfer coefficient can be obtained by integrating the local heat transfer coefficient from $x = 0$ to $x = L$.

$$\overline{h} = \frac{1}{L}\int_0^L h dx = \frac{k}{L}\left[\frac{g\beta(T_s - T_\infty)}{4\nu^2}\right]^{1/4} \cdot g(Pr) \cdot \int_0^L \frac{dx}{x^{1/4}} \qquad (2.52)$$

Thus,

$$\overline{Nu} = \frac{\overline{h}L}{k} = \frac{4}{3}\left(\frac{Gr_x}{4}\right)^{1/4} g(Pr) = \frac{4}{3}Nu_{x=L}$$

It should be noted that foregoing results can be applied whether the surface temperature (T_s) is higher than the free stream temperature (T_∞) or not. If $T_s < T_\infty$, the leading edge will be located at the top and positive x is defined as being in the direction of gravity.

Thus, the Nusselt number containing the natural convective heat transfer coefficient is a function of the Grashof number and the Prandtl number as shown in Eq. (2.51). However for external flow geometries, empirical correlations for the Nusselt number usually take the following form for engineering calculations

$$Nu = \frac{hL}{k} = \text{Constant} \cdot Ra^n \tag{2.53}$$

where the Rayleigh number is

$$Ra = GrPr = \frac{g\beta(T_s - T_\infty)L^3}{\nu\alpha} \tag{2.54}$$

where: Pr = Prandtl number
Gr = Grashof number
ν = Kinematic viscosity
g = Gravitational constant
α = Thermal diffusivity
β = Volumetric thermal expansion coefficient
T_∞ = Temperature of free stream
T_s = Temperature of the solid surface
L = Characteristic length of geometry

The properties listed above are evaluated for the fluid that is convecting. Typical values of the exponent, n, in Eq. (2.53) are 1/4 and 1/3 for laminar and turbulent flows respectively. When water constituted the medium, all properties of water were considered to be constant with temperature and only the temperature difference between the water and the wall in Eq. (2.54) was considered to vary with time. Combining Eqs. (2.25) and (2.53), the heat flux from the bath to the brick takes the form

$$q_{in} = H_1(\theta'_b - \theta'_n)^{1+n} \qquad (2.55)$$

where H_1 is constant, and it is understood that θ'_b is equivalent to T_∞ and θ'_n to T_s. Figure 2.12 shows calculated bath temperatures obtained from Eq. (2.55) using a value of 0.25 for the exponent n.

In this case the heat transfer coefficient is underestimated since calculated bath temperatures are consistently higher than measured values. The error is higher than that of Figure 2.9 as shown in Table 2.2. As expected some value of n between 0 and 0.25 yields accurate predictions. The agreement is excellent when n is 0.08 as shown by the results in Figure 2.13.

Also shown on the same graph are the two temperature traces used by the model to generate the computed bath temperature trace. During the early stages of the experiment(up to a time of 30 min.) the heat transfer phenomenon was clearly transient wherein the temperature at some locations in the wall was increasing while the bath temperature was decreasing. These tests were repeated several times - the results were virtually identical.

Table 2.2: Calculated error for water model experiment with vertical test piece for different Δt's and exponents(n).

Δt	n	Error
10	0	1.43
20	0	.387
30	0	.269
40	0	.223
50	0	.209
30	0.25	.9
30	0.08	.12

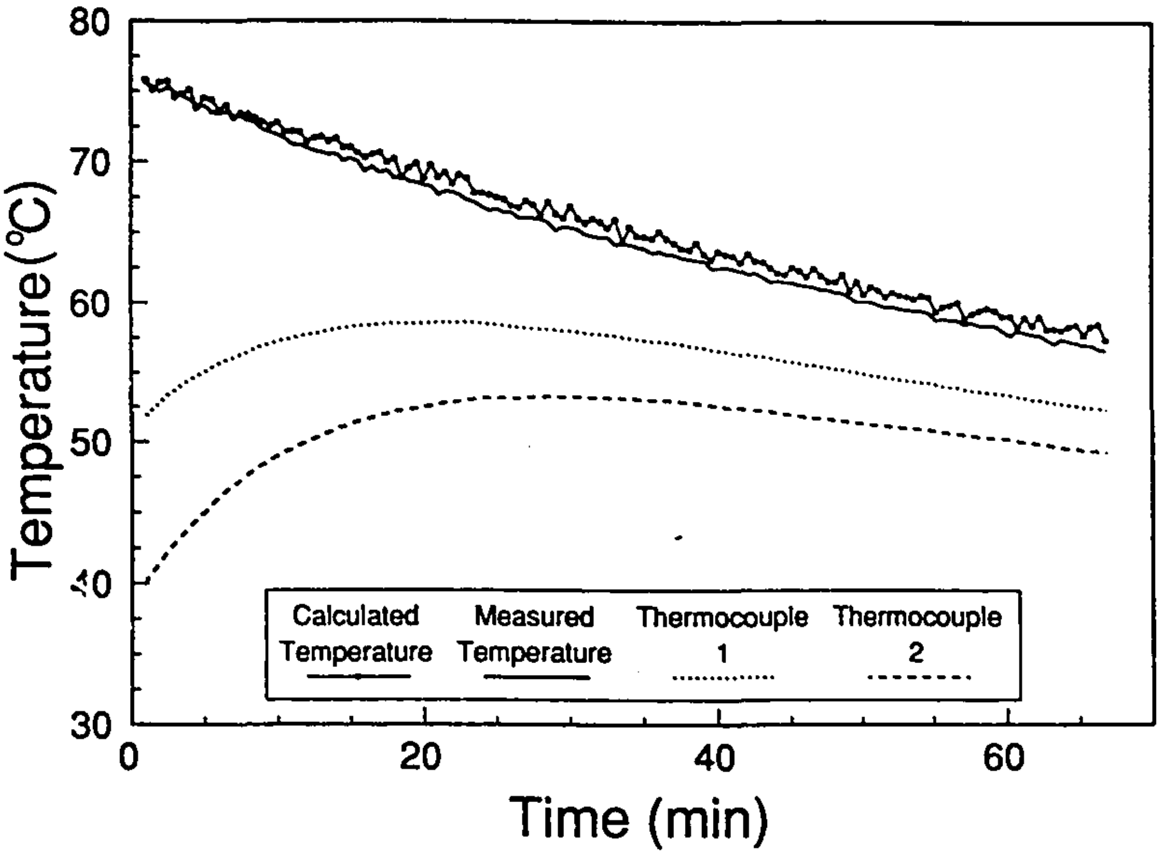

Figure 2.12: Computed and measured bath temperatures of water model experiment for vertical test piece when $\Delta t = 30$ sec. and $n = 0.25$.

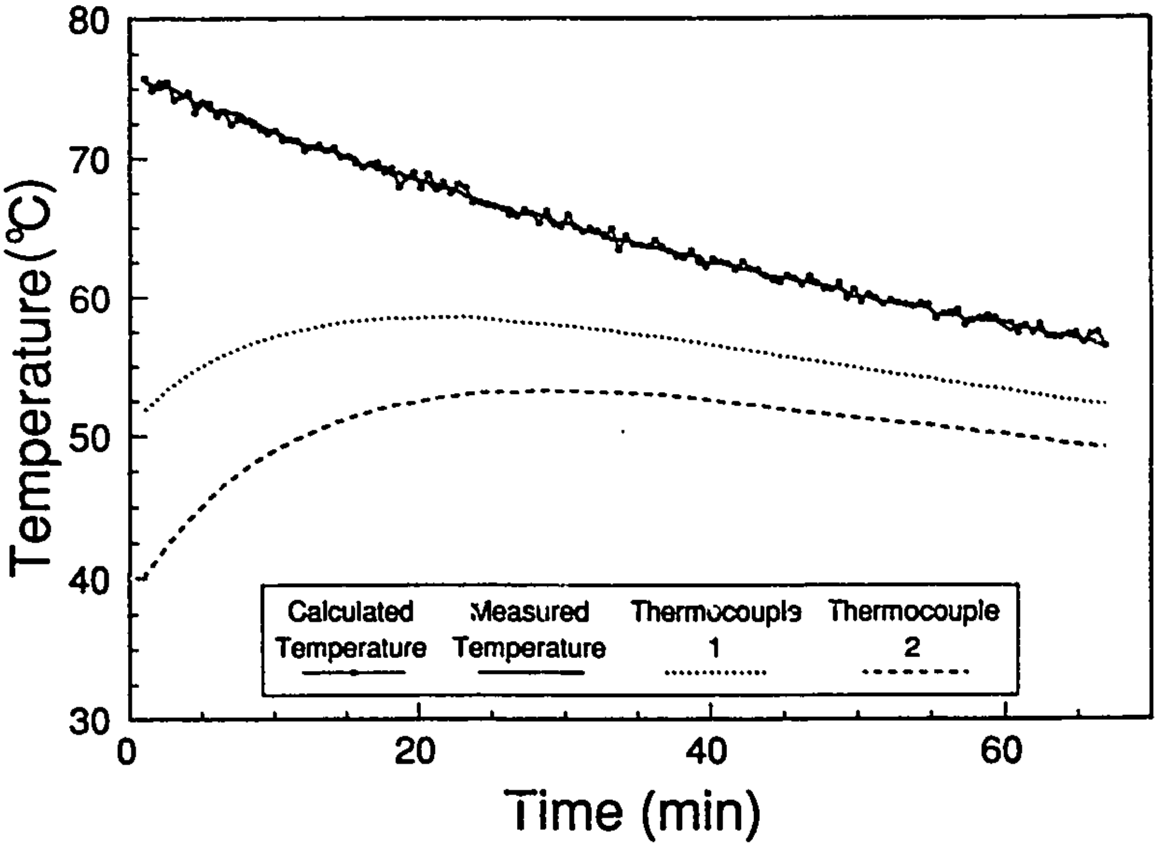

Figure 2.13: Computed and measured bath temperatures of water model experiment for vertical test piece when $\Delta t = 30$ sec. and $n = 0.08$.

Test piece in horizontal position

Figure 2.14 shows the calculated and measured temperatures obtained when the test piece was placed on top of the water in the horizontal position. These experiments were performed in an effort to evaluate the possibility of placing the test piece on the top layer of steel in the real system instead of placing the test piece in the side wall of the tundish. The time increment was 5 seconds. This figure clearly shows how a small time step produces large fluctuations which is evident from a comparison of Figures 2.14 and 2.15. In Figure 2.15 the time increment has been increased to 10 seconds. The frequency of the oscillation is quite similar to that shown in Figure 2.14 but the amplitude of the fluctuation of the calculated temperature has been decreased noticeably. The amplitude of the oscillations of calculated temperature values was decreased further as the time increments were increased to 20, 30, and 50 seconds as shown in Figures 2.16, 2.17, and 2.18. This trend is also discernable in Table 2.3.

From Figure 2.18, we can see that the model is overestimating H values and thus shows lower values of calculated bath temperatures. Figure 2.19 shows calculated bath temperature acquired from Eq. (2.55) using a value of 0.33 for the exponent n. For this test, calculated bath temperatures are a little higher than the measurements. Therefore some value between 0 and 1/3 would give good agreement between calculated and measured values and as shown in Figure 2.20 there is good agreement when n was set at 0.25.

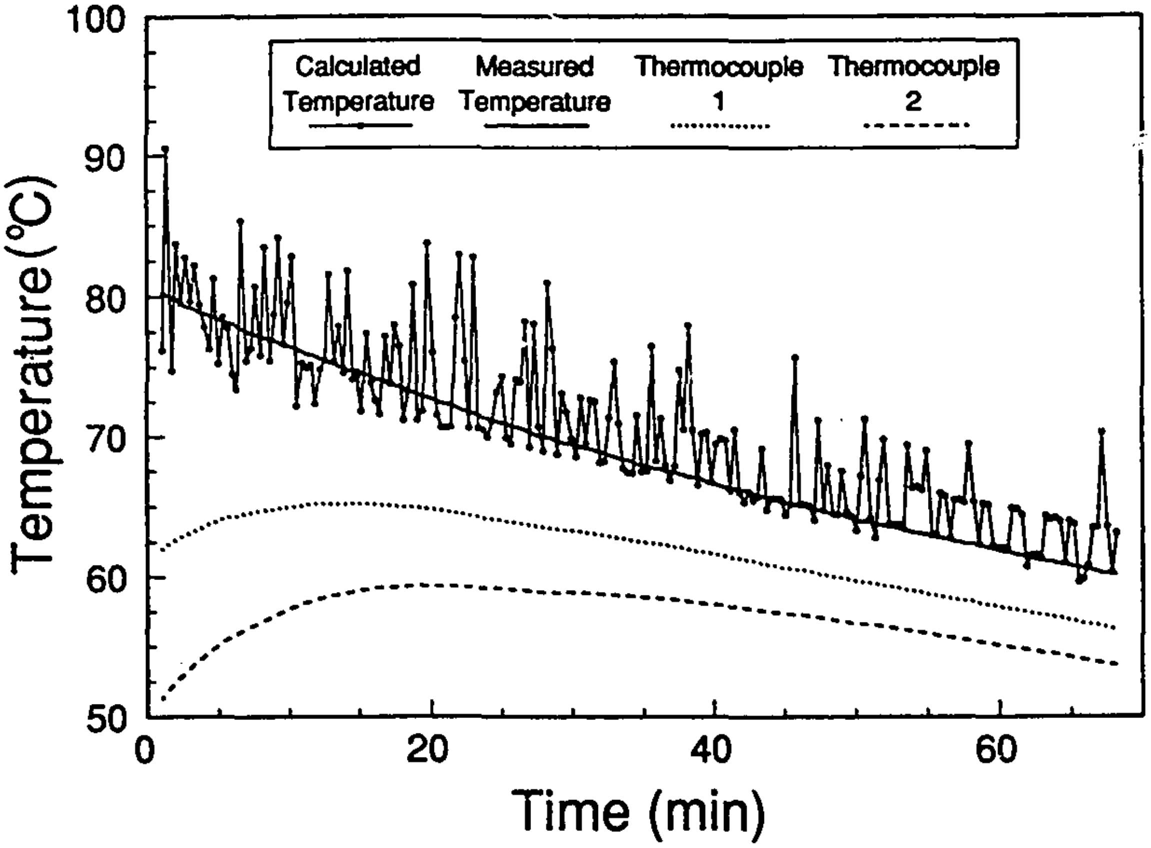

Figure 2.14: Computed and measured bath temperatures of water model experiment for horizontal test piece when $\Delta t = 5$ sec. and $n = 0$.

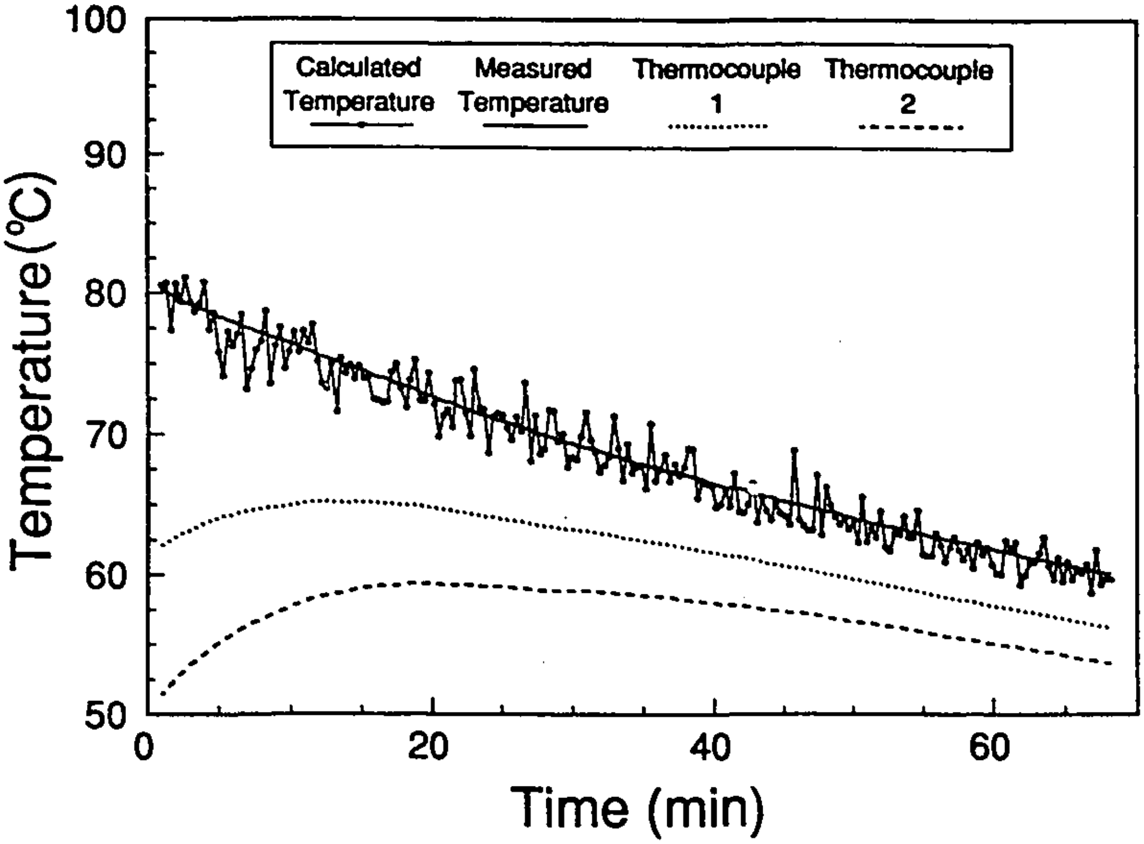

Figure 2.15: Computed and measured bath temperatures of water model experiment for horizontal test piece when $\Delta t = 10$ sec. and $n = 0$.

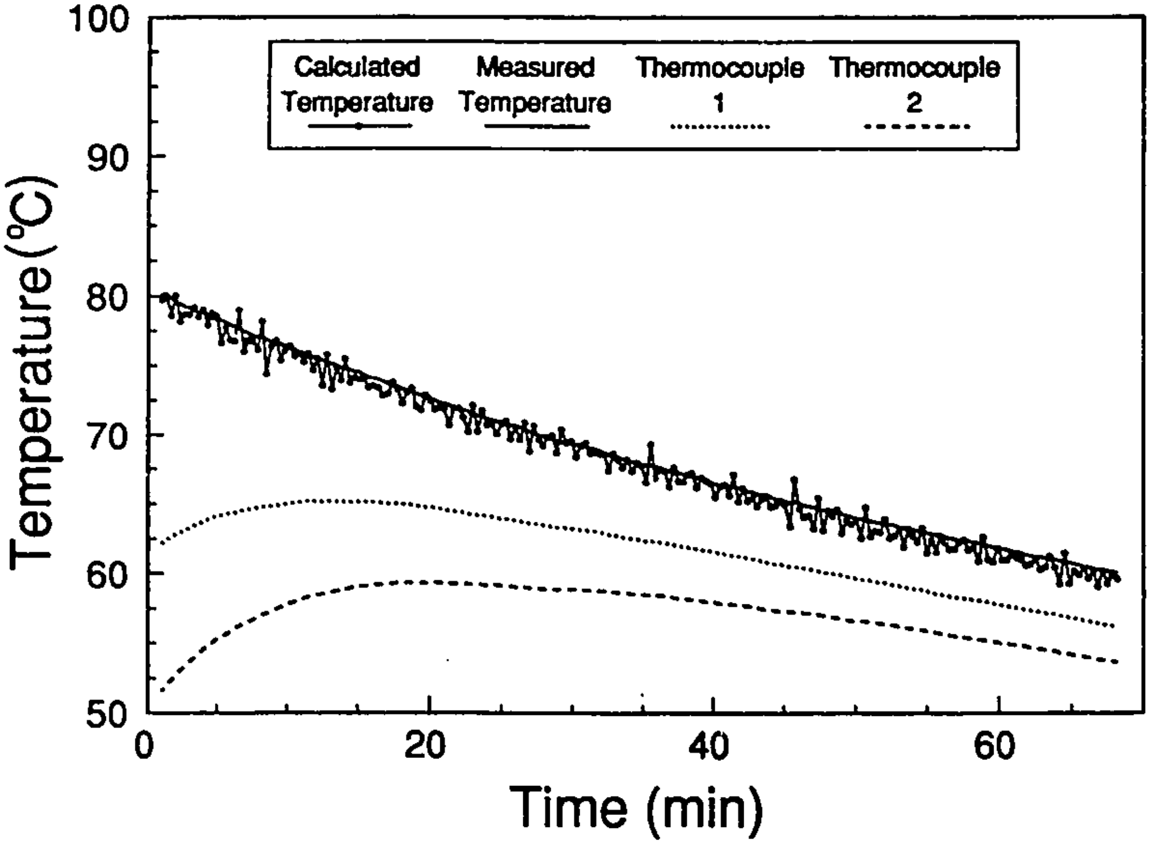

Figure 2.16: Computed and measured bath temperatures of water model experiment for horizontal test piece when $\Delta t = 20$ sec. and $n = 0$.

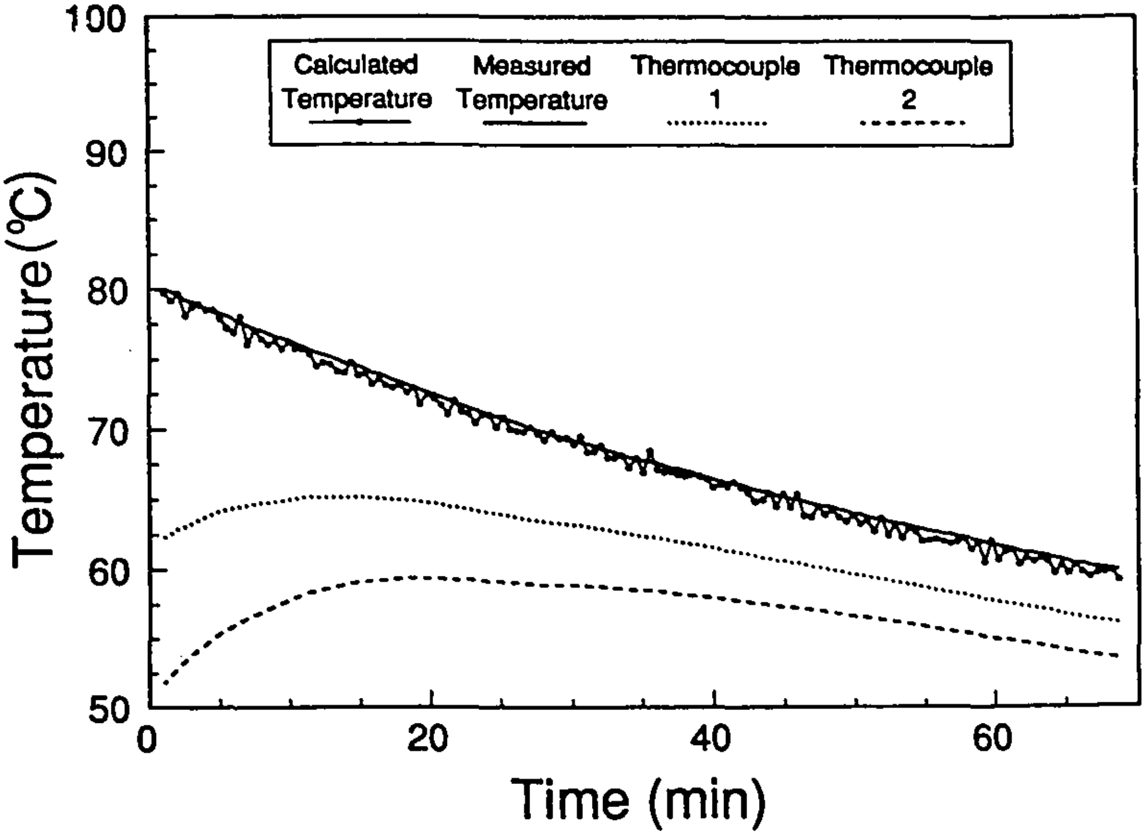

Figure 2.17: Computed and measured bath temperatures of water model experiment for horizontal test piece when $\Delta t = 30$ sec. and $n = 0$.

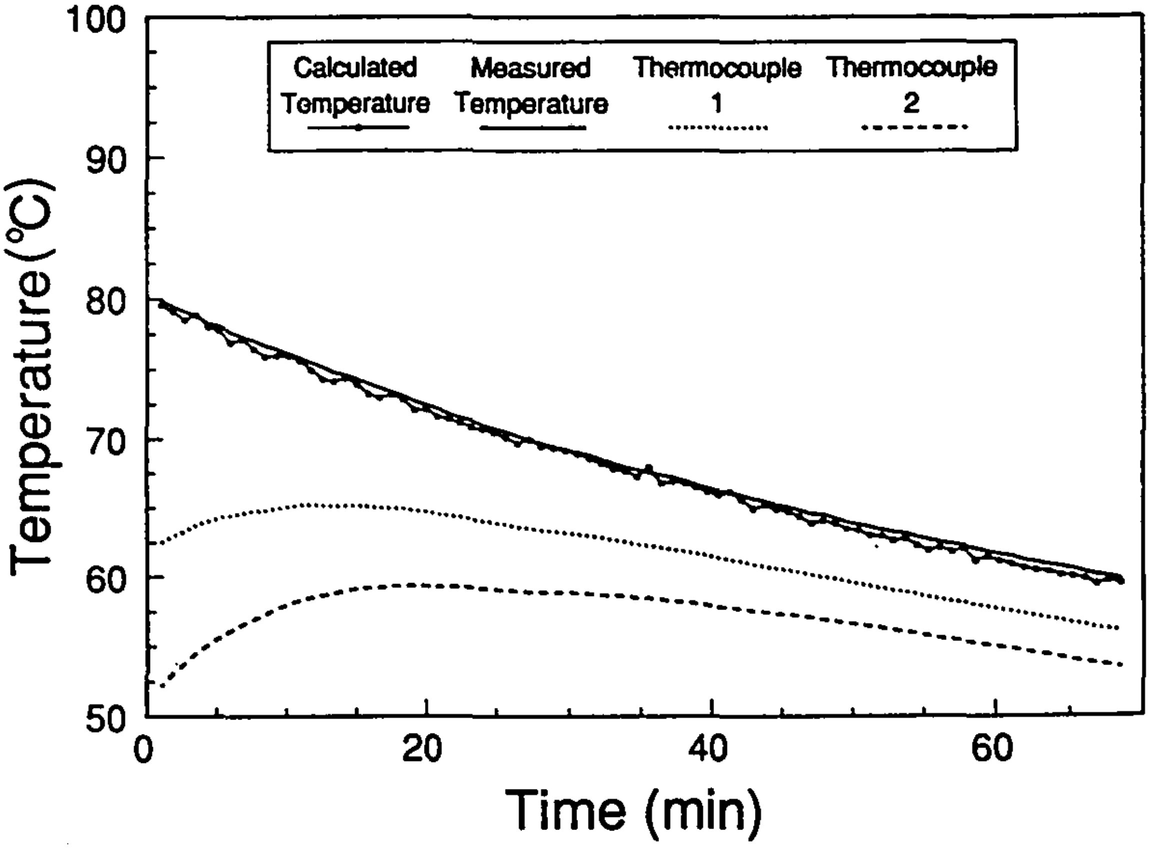

Figure 2.18: Computed and measured bath temperatures of water model experiment for horizontal test piece when $\Delta t = 50$ sec. and $n = 0$.

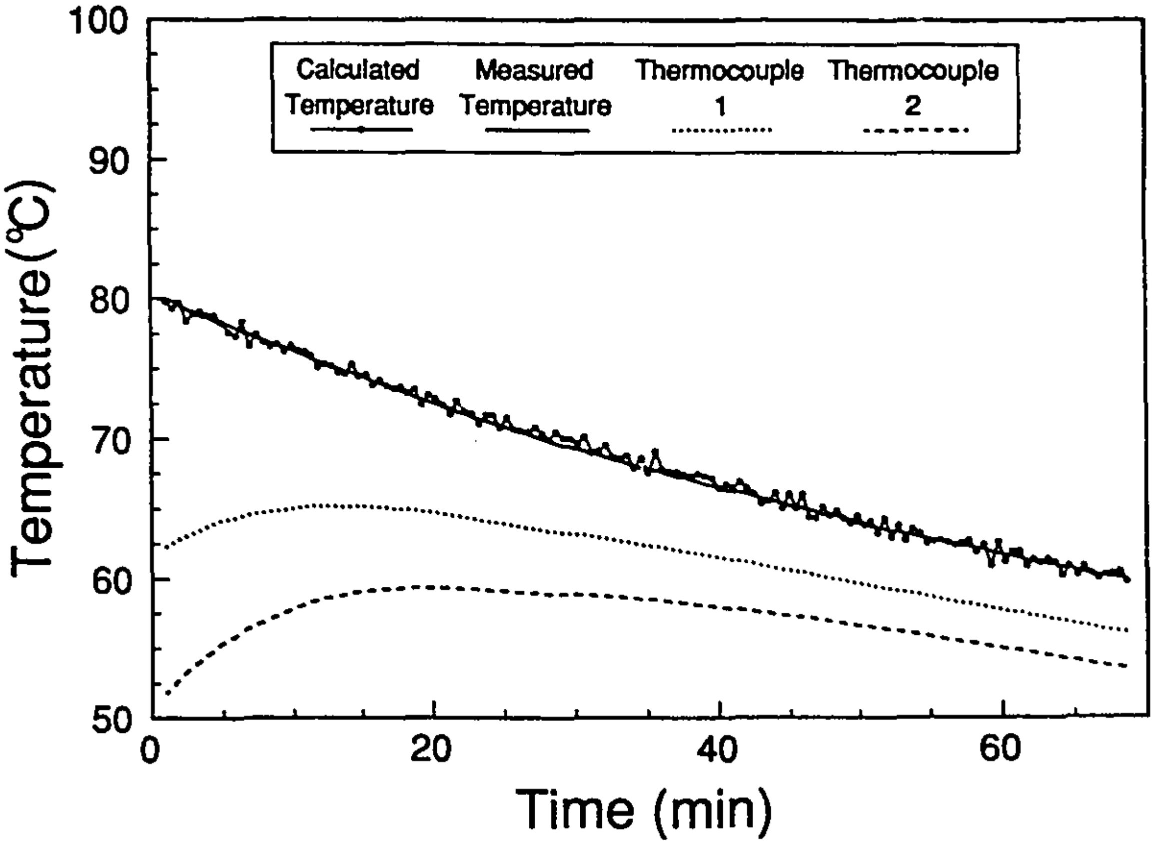

Figure 2.19: Computed and measured bath temperatures of water model experiment for horizontal test piece when $\Delta t = 30$ sec. and $n = 0.33$.

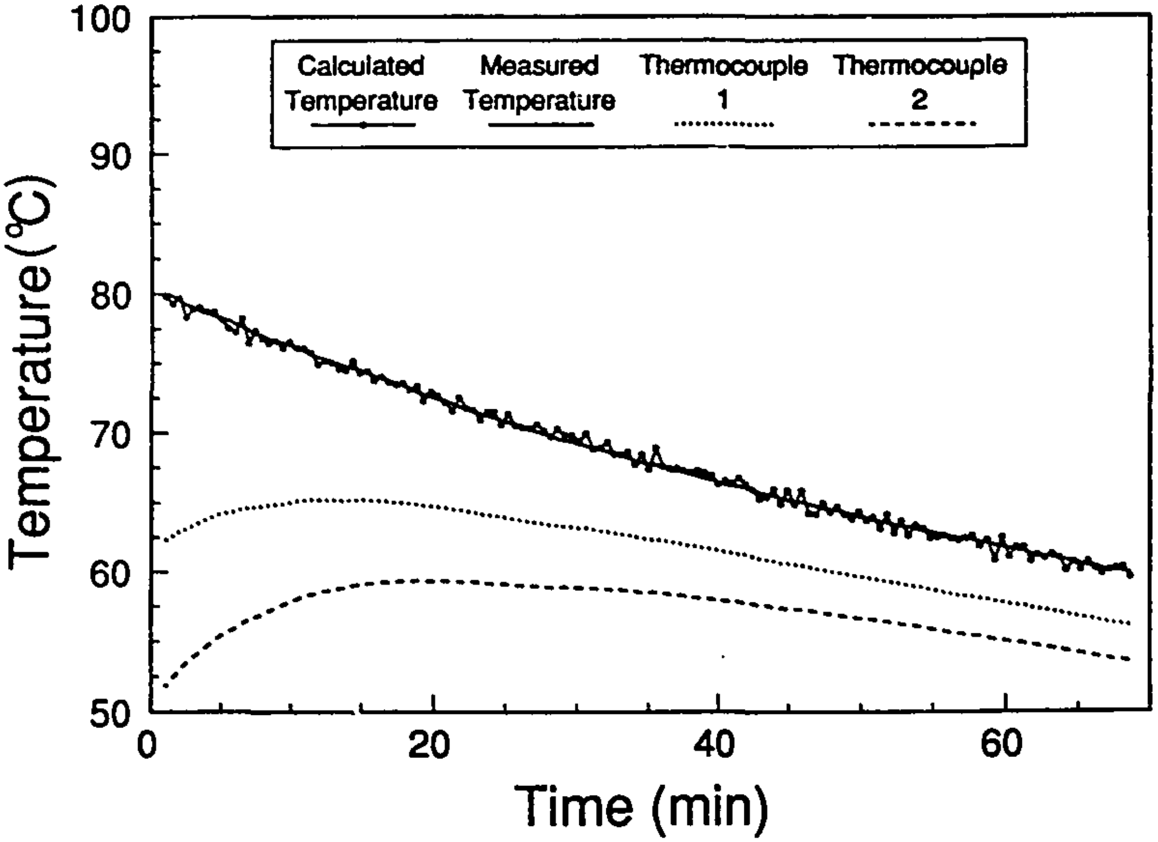

Figure 2.20: Computed and measured bath temperatures of water model experiment for horizontal test piece when $\Delta t = 30$ sec. and $n = 0.25$.

Table 2.3: Calculated error for water model experiment with horizontal test piece for different Δt's and exponents(n).

Δt	n	Error
5	0	9.99
10	0	1.83
20	0	.563
30	0	.31
40	0	.247
50	0	.219
30	.33	.17
30	.25	.15

Experiments with aluminum

A set of high temperature laboratory experiments were also carried out to test the 1-D model. For these tests, aluminum was melted in a stainless steel vessel. This same mathematical model was used to compute bath temperature based on internal refractory temperatures. It is worth noting that such is mathematically viable only if the convective heat transfer coefficient can be assigned a value. The temperature dependence of the kinematic viscosity term in Eq. (2.54) was also taken into account for the high temperature experiments. The viscosity for liquid aluminum has been measured experimentally by V. I. Kononenko et al.[63] from the melting point up to 1300 K. In this range the kinematic viscosity(m^2/s) has been found to vary according to the equation

$$\nu = 12.32 \times 10^{-8} exp(1228/T) \tag{2.56}$$

Incorporating Eq. (2.56) into Eq. (2.53), and subsequently rewriting Eq. (2.55) yields the following:

$$q_{in} = H_2(\theta'_b - \theta'_n)^{1+n}\{exp(1228/T_f)\}^{-n} \tag{2.57}$$

where T_f is the average film temperature, $\{(\theta'_b + \theta'_n)/2\}$. As before, the constant H_2 was calculated by 'priming' Eq. (2.57) with an actual bath temperature measurement obtained with an immersion thermocouple. Since the system of simultaneous equations generates values for q_{in} and θ'_n, Eq. (2.57) reduces to one equation in one unknown. Newton's method was then used to solve the ensuing non-linear equation for θ_b'. The results are shown in Figure 2.21. Again, computed and measured bath temperatures were in excellent agreement.

This 1-D model was found to be adequate if the refractory section was embedded within the wall of a vessel. However, in many plants operational constraints do not permit one to readily locate thermocouples in the wall of a vessel such as a tundish. Thus, for the full scale plant trials it was deemed necessary to use a 'float' system whereby the refractory test piece is lowered onto the melt and allowed to float on the molten steel. This design change had the effect of altering the heat flow patterns in the test piece to the point that a 1-D system could no longer be assumed. After careful consideration it was decided that the most viable solution would be to use a cylindrical test piece and to analyze the results with a 2-D model the derivation of which is presented in the following section.

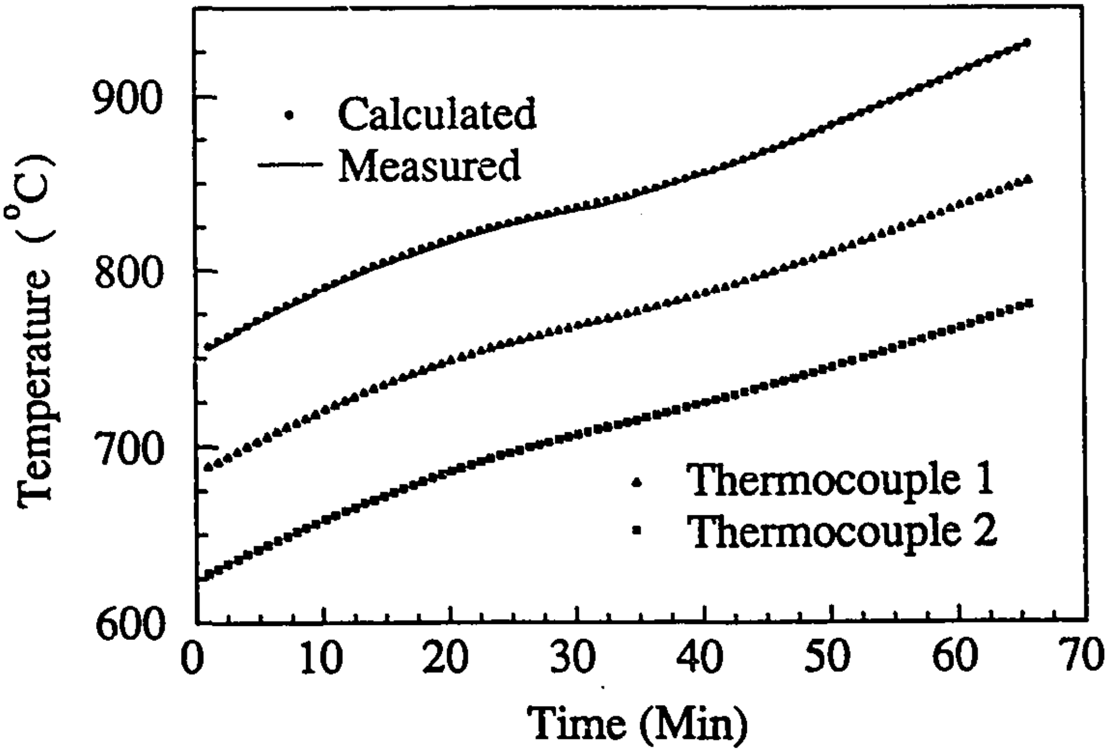

Figure 2.21: Comparison of computed and measured aluminum temperatures using the 1-D model when $n = 0.25$.

2.3 2-D Cylindrical Model

2.3.1 Mathematical Model

The two dimensional model was also based on the implicit finite difference formulation of Fourier's heat conduction equation. The spatial distribution of nodal points in the cylindrical refractory section that was adopted for the present study is shown in Figure 2.22. The 2 dimensions considered in the model are the radial and longitudinal axes. Angular variations were not considered in this analysis however, it should be noted that all angular displacements implied in the 2-D mathematical model were taken to be 1 radian in magnitude. Heat fluxes per unit area between the bath and the test piece at each surface node submerged in the bath were assumed to be equal and expressed as $\dot{q}''_{in}$. Heat fluxes from the surface nodes exposed to the surroundings were also assumed to be equal and represented as $\dot{q}''_{out}$.

(A) Internal nodes l, z

Assuming that heat flows from right to left and from bottom to top in the 2-D nodal grid presented in Figure 2.22, an overall energy balance as applied to node l, z assuming an angular displacement of 1 radian can be written as follows:

$$\begin{pmatrix} \text{Rate of energy} \\ \text{into node } l, z \end{pmatrix} - \begin{pmatrix} \text{Rate of energy} \\ \text{out of node } l, z \end{pmatrix}$$

$$+ \begin{pmatrix} \text{Rate of energy} \\ \text{generated in node } l, z \end{pmatrix} = \begin{pmatrix} \text{Rate of energy} \\ \text{accumulated in node } l, z \end{pmatrix}$$

or

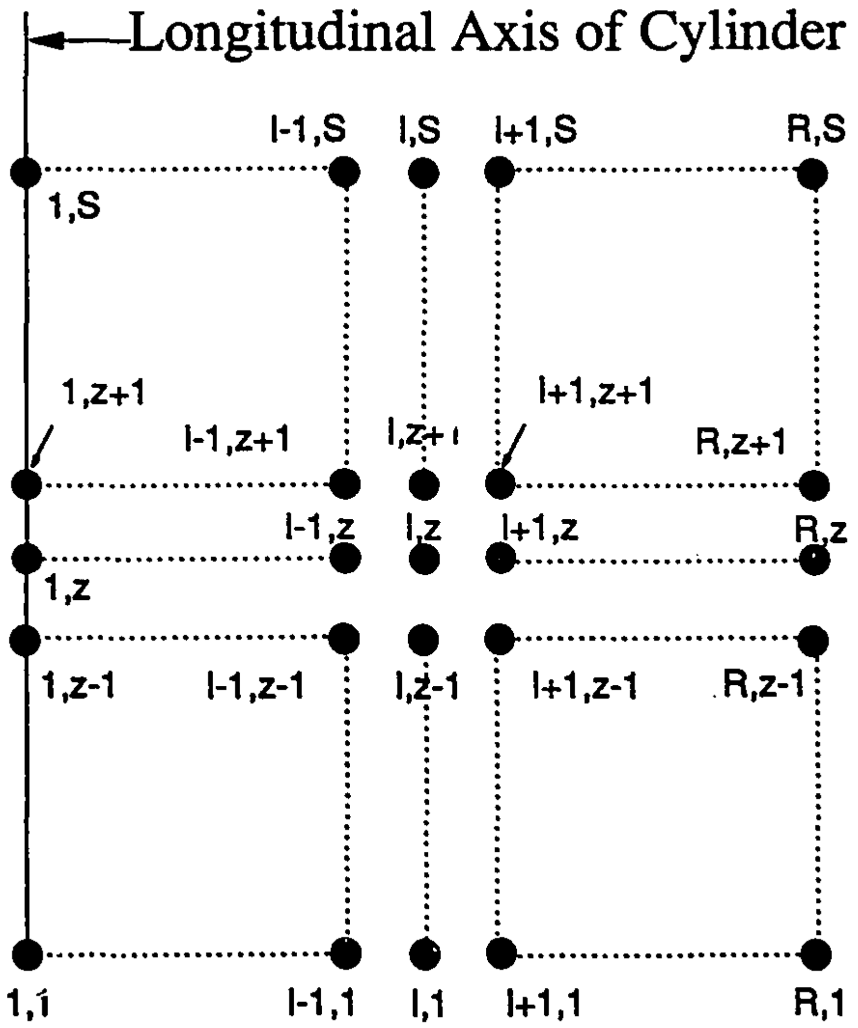

Figure 2.22: 2-D spatial distribution of nodal points in a cylindrical test piece.

$$\begin{aligned}\dot{q}_{l+1,z\to l,z} + \dot{q}_{l,z+1\to l,z} - \dot{q}_{l,z\to l-1,z} - \dot{q}_{l,z\to l,z-1} + \dot{q}'''_{l,z}V_{l,z}& \\ = \rho_{l,z}C_{l,z}V_{l,z}\frac{\theta'_{l,z}-\theta_{l,z}}{\Delta t} & \qquad (2.58)\end{aligned}$$

where: $V_{l,z}$ = Volume of node l,z per radian of angular displacement

$\rho_{l,z}$ = Density of node l,z

$C_{l,z}$ = Heat capacity of node l,z

$\theta_{l,z}$ = Temperature at time t at nodal point l,z

$\theta'_{l,z}$ = Value of $\theta_{l,z}$ at $t+\Delta t$

Δt = Iterative time increment

$\dot{q}'''$ = Rate of heat generation per unit volume

$\dot{q}_{l+1,z\to l,z}$ = Heat flow rate from node $l+1,z$ to l,z per radian of angular displacement

From Fourier's law of conduction

$$\dot{q}_{l+1,z\to l,z} = k_{l+1,z\to l,z}(l-1/2)\Delta r\Delta z\frac{(\theta'_{l+1,z}-\theta'_{l,z})}{\Delta r} \qquad (2.59)$$

$$\dot{q}_{l,z\to l-1,z} = k_{l,z\to l-1,z}(l-3/2)\Delta r\Delta z\frac{(\theta'_{l,z}-\theta'_{l-1,z})}{\Delta r} \qquad (2.60)$$

$$\dot{q}_{l,z-1\to l,z} = k_{l,z-1\to l,z}(l-1)\Delta r^2\frac{(\theta'_{l,z-1}-\theta'_{l,z})}{\Delta z} \qquad (2.61)$$

$$\dot{q}_{l,z\to l,z+1} = k_{l,z\to l,z+1}(l-1)\Delta r^2\frac{(\theta'_{l,z}-\theta'_{l,z+1})}{\Delta z} \qquad (2.62)$$

where: Δr = Radial nodal point spacing

Δz = Vertical nodal point spacing

$k_{l+1,z-l,z}$ = Thermal conductivity between nodal points $l+1, z$ and l, z

Rearranging Eq. (2.58) gives

$$\dot{q}_{l+1,z\to l,z} - \dot{q}_{l,z\to l-1,z} + \dot{q}_{l,z+1\to l,z} - \dot{q}_{l,z\to l,z-1}$$
$$= \rho_{l,z} C_{l,z} (l-1) \Delta r^2 \Delta z \frac{\theta'_{l,z} - \theta_{l,z}}{\Delta t} \qquad (2.63)$$

where $\dot{q}'''_{l,z} = 0$. Substituting Eqs. (2.59), (2.60), (2.61) and (2.62) into Eq. (2.63) yields the following:

$$\left(\frac{l-1/2}{l-1}\frac{\alpha\Delta t}{\Delta r^2}\right)\theta'_{l+1,z} + \left(\frac{l-3/2}{l-1}\frac{\alpha\Delta t}{\Delta r^2}\right)\theta'_{l-1,z} + \left(\frac{\alpha\Delta t}{\Delta z^2}\right)\theta'_{l,z+1}$$
$$+ \left(\frac{\alpha\Delta t}{\Delta z^2}\right)\theta'_{l,z-1} - \left(\frac{2\alpha\Delta t}{\Delta r^2} + \frac{2\alpha\Delta t}{\Delta z^2} + 1\right)\theta'_{l,z} = -\theta_{l,z} \qquad (2.64)$$

for $2 \leq l \leq R-1$ and $2 \leq z \leq S-1$

The thermal conductivity, density and heat capacity terms have been lumped together in Eq. (2.64) as the thermal diffusivity, α which is assumed to be a function of temperature.

(B) Center bottom node 1, 1

$$\begin{pmatrix}\text{Rate of energy}\\ \text{into node 1,1}\end{pmatrix} - \begin{pmatrix}\text{Rate of energy}\\ \text{out of node 1,1}\end{pmatrix}$$
$$+ \begin{pmatrix}\text{Rate of energy}\\ \text{generated in node 1,1}\end{pmatrix} = \begin{pmatrix}\text{Rate of energy}\\ \text{accumulated in node 1,1}\end{pmatrix}$$

or

$$\dot{q}_{2,1\rightarrow 1,1} - \dot{q}_{1,1\rightarrow 1,2} + \dot{q}''_{in} A_{1,1} = \rho_{1,1} C_{1,1} V_{1,1} \frac{\theta'_{1,1} - \theta_{1,1}}{\Delta t} \tag{2.65}$$

where $A_{1,1}$ is the surface area in contact with the bath $(\Delta r^2/8)$. From Fourier's law of conduction

$$\dot{q}_{2,1\rightarrow 1,1} = k_{2,1\rightarrow 1,1} \frac{\Delta r \Delta z}{4} \frac{(\theta'_{2,1} - \theta'_{1,1})}{\Delta r} \tag{2.66}$$

$$\dot{q}_{1,1\rightarrow 1,2} = k_{1,1\rightarrow 1,2} \frac{\Delta r^2}{8} \frac{(\theta'_{1,1} - \theta'_{1,2})}{\Delta z} \tag{2.67}$$

Substituting Eqs. (2.66) and (2.67) into Eq. (2.65) yields the following:

$$\left(\frac{4\alpha\Delta t}{\Delta r^2}\right)\theta'_{2,1} + \left(\frac{2\alpha\Delta t}{\Delta z^2}\right)\theta'_{1,2} + q_{in}\frac{2\Delta t}{\Delta z} - \left(\frac{4\alpha\Delta t}{\Delta r^2} + \frac{2\alpha\Delta t}{\Delta z^2} + 1\right)\theta'_{1,1} = -\theta_{1,1} \tag{2.68}$$

where $q_{in} = \dot{q}''_{in}/\rho C$. q_{in} in Eq. (2.68) represents a modified form of the heat flux from the bath to the refractory test piece.

(C) Bottom surface nodes $l, 1$

The heat balance yields:

$$\dot{q}_{l+1,1\rightarrow l,1} - \dot{q}_{l,1\rightarrow l-1,1} - \dot{q}_{l,1\rightarrow l,2} + \dot{q}''_{in} A_{l,1} = \rho_{l,1} C_{l,1} V_{l,1} \frac{\theta'_{l,1} - \theta_{l,1}}{\Delta t} \tag{2.69}$$

where $A_{l,1}$ is the surface area perpendicular to heat flow, $((l-1)\Delta r^2/2)$, and

$$\dot{q}_{l+1,1\rightarrow l,1} = k_{l+1,1\rightarrow l,1}\frac{(l-1/2)\Delta r\Delta z}{2}\frac{(\theta'_{l+1,1}-\theta'_{l,1})}{\Delta r} \tag{2.70}$$

$$\dot{q}_{l,1\rightarrow l-1,1} = k_{l,1\rightarrow l-1,1}\frac{(l-3/2)\Delta r\Delta z}{2}\frac{(\theta'_{l,1}-\theta'_{l-1,1})}{\Delta r} \tag{2.71}$$

$$\dot{q}_{l,1\rightarrow l,2} = k_{l,1\rightarrow l,2}(l-1)\Delta r^{2}\frac{(\theta'_{l,1}-\theta'_{l,2})}{\Delta z} \tag{2.72}$$

Substituting Eqs. (2.70), (2.71) and (2.72) into Eq. (2.69) yields the following:

$$\left(\frac{l-1/2}{l-1}\frac{\alpha\Delta t}{\Delta r^{2}}\right)\theta'_{l+1,1}+\left(\frac{l-3/2}{l-1}\frac{\alpha\Delta t}{\Delta r^{2}}\right)\theta'_{l-1,1}+\left(\frac{2\alpha\Delta t}{\Delta z^{2}}\right)\theta'_{l,2}$$

$$+q_{in}\frac{2\Delta t}{\Delta z}-\left(\frac{2\alpha\Delta t}{\Delta r^{2}}+\frac{2\alpha\Delta t}{\Delta z^{2}}+1\right)\theta'_{l,1}=-\theta_{l,1} \tag{2.73}$$

for $2\leq l\leq R-1$

(D) Outside bottom node $R,1$

The overall energy balance for node $R,1$ can be stated as:

$$\dot{q}''_{in}A_{R,1}-\dot{q}_{R,1\rightarrow R,2}-\dot{q}_{R,1\rightarrow R-1,1}=\rho_{R,1}C_{R,1}V_{R,1}\frac{\theta'_{R,1}-\theta_{R,1}}{\Delta t} \tag{2.74}$$

where $A_{R,1}$ comprises both the vertical and horizontal surface area components in contact with the melt and is computed as $((R-1)\Delta r\Delta z/2+(R-5/4)\Delta r^{2}/2)$, and

$$\dot{q}_{R,1\to R-1,1} = k_{R,1\to R-1,1}\frac{(l-3/2)\Delta r\Delta z}{2}\frac{(\theta'_{R,1}-\theta'_{R-1,1})}{\Delta r} \tag{2.75}$$

$$\dot{q}_{R,1\to R,2} = k_{R,1\to R,2}\frac{(R-5/4)\Delta r^2}{2}\frac{(\theta'_{R,1}-\theta'_{R,2})}{\Delta z} \tag{2.76}$$

Substituting Eqs. (2.75) and (2.76) into Eq. (2.74) yields the following:

$$\left(\frac{2\alpha\Delta t}{\Delta z^2}\right)\theta'_{R,2} + \left(\frac{R-3/2}{R-5/4}\frac{2\alpha\Delta t}{\Delta r^2}\right)\theta'_{R-1,1} + \left(\frac{R-1}{R-5/4}\frac{2\Delta t}{\Delta r} + \frac{2\Delta t}{\Delta z}\right)q_{in}$$

$$-\left(\frac{R-3/2}{R-5/4}\frac{2\alpha\Delta t}{\Delta r^2} + \frac{2\alpha\Delta t}{\Delta z^2} + 1\right)\theta'_{R,1} = -\theta_{R,1} \tag{2.77}$$

where $q_{in} = \dot{q}''_{in}/\rho C$

(E) Center inner nodes $1, z$

Node $1, z$ has the following energy balance:

$$\dot{q}_{2,z\to 1,z} + \dot{q}_{1,z-1\to 1,z} - \dot{q}_{1,z\to 1,z+1} = \rho_{1,z}C_{1,z}V_{1,z}\frac{\theta'_{1,z}-\theta_{1,z}}{\Delta t} \tag{2.78}$$

where

$$\dot{q}_{2,z\to 1,z} = k_{2,z\to 1,z}\frac{\Delta r\Delta z}{2}\frac{(\theta'_{2,z}-\theta'_{1,z})}{\Delta r} \tag{2.79}$$

$$\dot{q}_{1,z-1\to 1,z} = k_{1,z-1\to 1,z}\frac{\Delta r^2}{8}\frac{(\theta'_{1,z-1}-\theta'_{1,z})}{\Delta z} \tag{2.80}$$

$$\dot{q}_{1,z\to 1,z+1} = k_{1,z\to 1,z+1}\frac{\Delta r^2}{8}\frac{(\theta'_{1,z} - \theta'_{1,z+1})}{\Delta z} \tag{2.81}$$

Substituting Eqs. (2.79), (2.80) and (2.81) into Eq. (2.78) yields the following:

$$\left(\frac{4\alpha\Delta t}{\Delta r^2}\right)\theta'_{2,z} + \left(\frac{\alpha\Delta t}{\Delta z^2}\right)\theta'_{1,z-1} + \left(\frac{\alpha\Delta t}{\Delta z^2}\right)\theta'_{1,z+1}$$

$$-\left(\frac{4\alpha\Delta t}{\Delta r^2} + \frac{2\alpha\Delta t}{\Delta z^2} + 1\right)\theta'_{1,z} = -\theta_{1,z} \tag{2.82}$$

for $2 \leq z \leq S-1$

(F) Center top node $1, S$

$$\dot{q}_{2,S\to 1,S} + \dot{q}_{1,S-1\to 1,S} - \dot{q}''_{out}A_{1,S} = \rho_{1,S}C_{1,S}V_{1,S}\frac{\theta'_{1,S} - \theta_{1,S}}{\Delta t} \tag{2.83}$$

where $A_{1,S}$ is the surface area outside the melt $(\Delta r^2/8)$, and

$$\dot{q}_{2,S\to 1,S} = k_{2,S\to 1,S}\frac{\Delta r\Delta z}{4}\frac{(\theta'_{2,S} - \theta'_{1,S})}{\Delta r} \tag{2.84}$$

$$\dot{q}_{1,S-1\to 1,S} = k_{1,S-1\to 1,S}\frac{\Delta r^2}{8}\frac{(\theta'_{1,S-1} - \theta'_{1,S})}{\Delta z} \tag{2.85}$$

Substituting Eqs. (2.84) and (2.85) into Eq. (2.83) yields the following:

$$\left(\frac{4\alpha\Delta t}{\Delta r^2}\right)\theta'_{2,S} + \left(\frac{2\alpha\Delta t}{\Delta z^2}\right)\theta'_{1,S-1} - \left(\frac{2\Delta t}{\Delta z}\right)q_{out}$$

$$-\left(\frac{4\alpha\Delta t}{\Delta r^2} + \frac{2\alpha\Delta t}{\Delta z^2} + 1\right)\theta'_{1,S} = -\theta_{1,S} \tag{2.86}$$

where $q_{out} = \dot{q}''_{out}/\rho C$.

(G) Top surface nodes l, S

$$\dot{q}_{l+1,S\to l,S} + \dot{q}_{l,S-1\to l,S} - \dot{q}_{l,S\to l-1,S} + \dot{q}''_{in}A_{l,S} = \rho_{l,S}C_{l,S}V_{l,S}\frac{\theta'_{l,S} - \theta_{l,S}}{\Delta t} \quad (2.87)$$

where $A_{l,S}$ is defined as $((l-1)\Delta r^2/2)$, and

$$\dot{q}_{l+1,S\to l,S} = k_{l+1,S\to l,S}\frac{(l-1/2)\Delta r\Delta z}{2}\frac{(\theta'_{l+1,S} - \theta'_{l,S})}{\Delta r} \quad (2.88)$$

$$\dot{q}_{l,S\to l-1,S} = k_{l,S\to l-1,S}\frac{(l-3/2)\Delta r\Delta z}{2}\frac{(\theta'_{l,S} - \theta'_{l-1,S})}{\Delta r} \quad (2.89)$$

$$\dot{q}_{l,S-1\to l,S} = k_{l,S-1\to l,S}(l-1)\Delta r^2\frac{(\theta'_{l,S-1} - \theta'_{l,S})}{\Delta z} \quad (2.90)$$

Substituting Eqs. (2.88), (2.89) and (2.90) into Eq. (2.87) yields the following:

$$\left(\frac{l-1/2}{l-1}\frac{\alpha\Delta t}{\Delta r^2}\right)\theta'_{l+1,S} + \left(\frac{l-3/2}{l-1}\frac{\alpha\Delta t}{\Delta r^2}\right)\theta'_{l-1,S} + \left(\frac{2\alpha\Delta t}{\Delta z^2}\right)\theta'_{l,S-1}$$

$$-q_{out}\frac{2\Delta t}{\Delta z} - \left(\frac{2\alpha\Delta t}{\Delta r^2} + \frac{2\alpha\Delta t}{\Delta z^2} + 1\right)\theta'_{l,S} = -\theta_{l,S} \quad (2.91)$$

for $2 \leq l \leq R-1$

(H) Outside top node R, S

$$\dot{q}_{R,S-1\to R,S} - \dot{q}_{R,S\to R-1,S} - \dot{q}''_{out}A_{R,S} = \rho_{R,S}C_{R,S}V_{R,S}\frac{\theta'_{R,S} - \theta_{R,S}}{\Delta t} \quad (2.92)$$

where $A_{R,S}$ is defined as $((R-1)\Delta r\Delta z/2 + (R-5/4)\Delta r^2/2)$, and

$$\dot{q}_{R,S\rightarrow R-1,S} \;=\; k_{R,S\rightarrow R-1,S}\frac{(R-3/2)\Delta r\Delta z}{2}\frac{(\theta'_{R,S}-\theta'_{R-1,S})}{\Delta r} \qquad (2.93)$$

$$\dot{q}_{R,S-1\rightarrow R,S} \;=\; k_{R,S-1\rightarrow R,S}\frac{(R-5/4)\Delta r^2}{2}\frac{(\theta'_{R,S-1}-\theta'_{R,S})}{\Delta z} \qquad (2.94)$$

Substituting Eqs. (2.93) and (2.94) into Eq. (2.92) yields the following:

$$\left(\frac{R-3/2}{R-5/4}\frac{2\alpha\Delta t}{\Delta r^2}\right)\theta'_{R-1,S} - \left(\frac{R-1}{R-5/4}\frac{2\Delta t}{\Delta r} + \frac{2\Delta t}{\Delta z}\right) q_{out}$$

$$+\left(\frac{2\alpha\Delta t}{\Delta z^2}\right)\theta'_{R,S-1} - \left(\frac{R-3/2}{R-5/4}\frac{2\alpha\Delta t}{\Delta r^2} + \frac{2\alpha\Delta t}{\Delta z^2} + 1\right)\theta'_{R,S} = -\theta_{R,S} \qquad (2.95)$$

(I) Outside nodes (submerged) R, z

$$\dot{q}_{R,z-1\rightarrow R,z} - \dot{q}_{R,z\rightarrow R,z+1} - \dot{q}_{R,z\rightarrow R-1,z} + \dot{q}''_{in}A_{R,z}$$

$$= \rho_{R,z}C_{R,z}V_{R,z}\frac{\theta'_{R,z}-\theta_{R,z}}{\Delta t} \qquad (2.96)$$

where $A_{R,z}$ is $((R-1)\Delta r\Delta z)$, and

$$\dot{q}_{R,z\rightarrow R-1,z} \;=\; k_{R,z\rightarrow R-1,z}(l-3/2)\Delta r\Delta z\frac{(\theta'_{R,z}-\theta'_{R-1,z})}{\Delta r} \qquad (2.97)$$

$$\dot{q}_{R,z-1\rightarrow R,z} \;=\; k_{R,z-1\rightarrow R,z}\frac{(R-5/4)\Delta r^2}{2}\frac{(\theta'_{R,z-1}-\theta'_{r}\;)}{\Delta z} \qquad (2.98)$$

$$\dot{q}_{R,z\rightarrow R,z+1} = k_{R,z\rightarrow R,z+1}\frac{(R-5/4)\Delta r^2}{2}\frac{(\theta'_{R,z}-\theta'_{R,z+1})}{\Delta z} \tag{2.99}$$

Substituting Eqs. (2.97), (2.98) and (2.99) into Eq. (2.96) yields the following:

$$\left(\frac{R-3/2}{R-5/4}\frac{2\alpha\Delta t}{\Delta r^2}\right)\theta'_{R-1,z}+\left(\frac{\alpha\Delta t}{\Delta z^2}\right)\theta'_{R,z+1}+\left(\frac{R-1}{R-5/4}\frac{2\Delta t}{\Delta r}\right)q_{in}$$

$$+\left(\frac{\alpha\Delta t}{\Delta z^2}\right)\theta'_{R,z-1}-\left(\frac{R-3/2}{R-5/4}\frac{2\alpha\Delta t}{\Delta r^2}+\frac{2\alpha\Delta t}{\Delta z^2}+1\right)\theta'_{R,z}=-\theta_{R,z} \tag{2.100}$$

for $2 \leq z \leq SN$. SN represents the number of nodes submerged into the bath.

(J) Outside nodes (not submerged) R, z

$$\left(\frac{R-3/2}{R-5/4}\frac{2\alpha\Delta t}{\Delta r^2}\right)\theta'_{R-1,z}+\left(\frac{\alpha\Delta t}{\Delta z^2}\right)\theta'_{R,z+1}-\left(\frac{R-1}{R-5/4}\frac{2\Delta t}{\Delta r}\right)q_{out}$$

$$+\left(\frac{\alpha\Delta t}{\Delta z^2}\right)\theta'_{R,z-1}-\left(\frac{R-3/2}{R-5/4}\frac{2\alpha\Delta t}{\Delta r^2}+\frac{2\alpha\Delta t}{\Delta z^2}+1\right)\theta'_{R,z}=-\theta_{R,z} \tag{2.101}$$

for $SN+1 \leq z \leq S-1$

Since Eqs. (2.64), (2.68), (2.73), (2.77), (2.82), (2.86), (2.91), (2.95), (2.100) and (2.101) contain $(R \times S)+2$ unknowns in $R \times S$ equations, two additional equations need to be generated. These are produced by actual thermocouple measurements at known locations.

If one considers a 4×6 nodal system, then 24 equations as derived from Eqs. (2.64), (2.68), (2.73), (2.77), (2.82), (2.86), (2.91), (2.95), (2.100) and

(2.101) can be coupled with two actual thermocouple measurements at two known locations and written in the following matrix form:

$$\mathbf{A} \times \mathbf{X} = \mathbf{B} \tag{2.102}$$

where **A** contains the coefficients of the energy balance equations and

$$\mathbf{X} = \begin{bmatrix} \theta'_{1,1} \\ \vdots \\ \theta'_{1,6} \\ \vdots \\ \theta'_{l,z} \\ \vdots \\ \theta'_{4,1} \\ \vdots \\ \theta'_{4,6} \\ q_{in} \\ q_{out} \end{bmatrix} \qquad \mathbf{B} = - \begin{bmatrix} \theta_{1,1} \\ \vdots \\ \theta_{1,6} \\ \vdots \\ \theta_{l,z} \\ \vdots \\ \theta_{4,1} \\ \vdots \\ \theta_{4,6} \\ -m_1 \\ -m_2 \end{bmatrix} \tag{2.103}$$

$\theta'_{1,1} \cdots \theta'_{4,6}$ represents the temperature at each nodal point at time $t + \Delta t$. $\theta_{1,1} \cdots \theta_{4,6}$ represent temperature at each nodal point at time t. m_1 and m_2 represent measured temperatures at two known locations in the test piece. Instantaneous bath temperature is computed from q_{in} as was done for the 1-D model.

2.3.2 Experimental

To evaluate the accuracy of the two-dimensional model, high temperature laboratory experiments were conducted. Figure 2.23 shows a schematic of the experimental apparatus. Aluminum was melted in a crucible contained in a gas furnace. Once the aluminum attained temperature, half of the test piece (magnesite brick) in which two thermocouples were embedded was immersed. The magnesite brick was cylindrical in shape and was 3 cm in radius and 5 cm high. Locations of the two thermocouples are shown in Figure 2.24 along with nodal positions. Another thermocouple was placed in the molten aluminum to measure bath temperature.

All experiments were controlled by a HP 85A microcomputer. The microcomputer permitted the storing of data onto a floppy disk and the subsequent processing of data followed by plotting.

2.3.3 Results and Discussions

A set of high temperature experiments were carried out to evaluate the 2-D model. As was described previously, testing of the 2-D model involves immersing a portion of a cylindrical magnesite test piece into molten aluminum. In these tests, the temperature dependence of the kinematic viscosity term in Eq. (2.54) was also taken into account. Thus the equation for q_{in} has the same form as Eq. (2.57). Figure 2.25 shows that computed and measured bath temperatures were in good agreement even though some fluctuations in the readings were evident. These, it was concluded, were caused by variations in the gas and air flow rates to the furnace.

In the present chapter, two mathematical models have been developed and tested. To obtain good agreement between calculated and measured temperature values, the exponent n, has to be determined for each specific system. This can be done with one experiment. Once the exponent has been found the model can predict the bath temperature continuously with one actual bath measurement which is used to *prime* the model and two continuous temperature measurements at known locations. In this way, one can monitor internal temperature readings of a test piece and couple them with the model to arrive at the melt temperature.

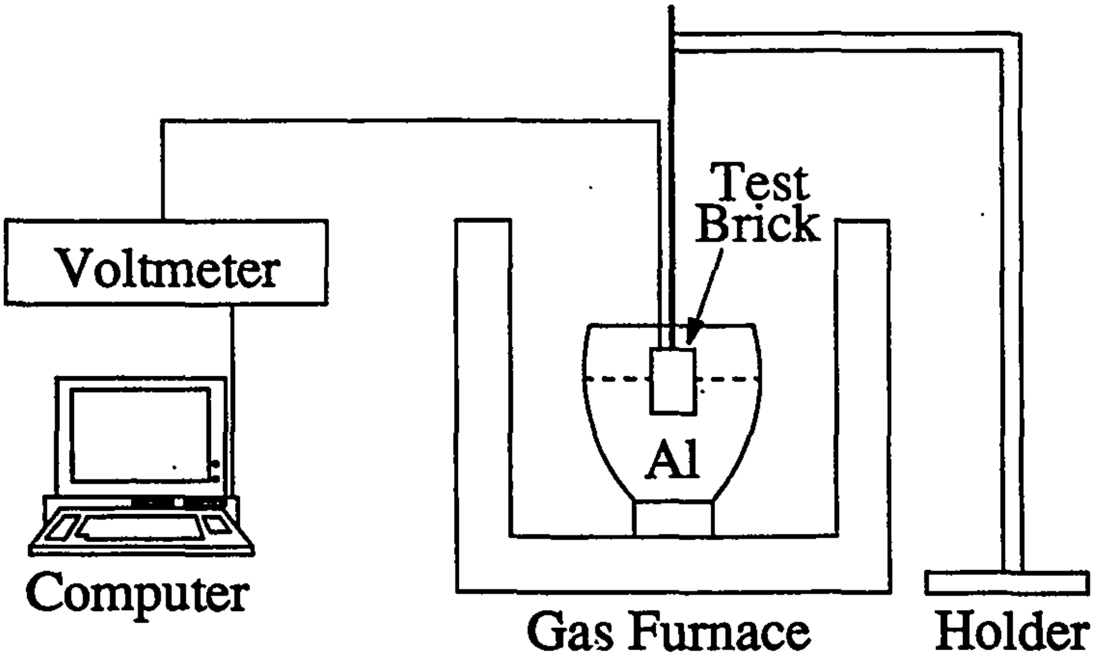

Figure 2.23: Schematic of 2-D model test apparatus.

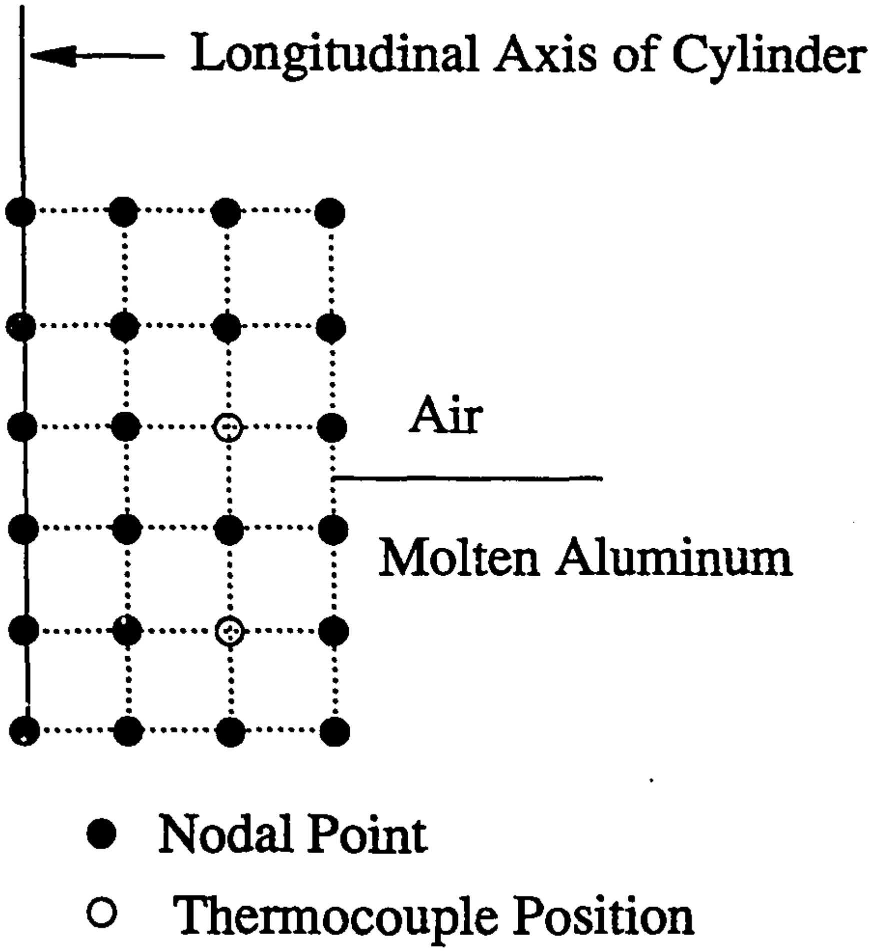

Figure 2.24: The positioning of thermocouples in the 2-D model.

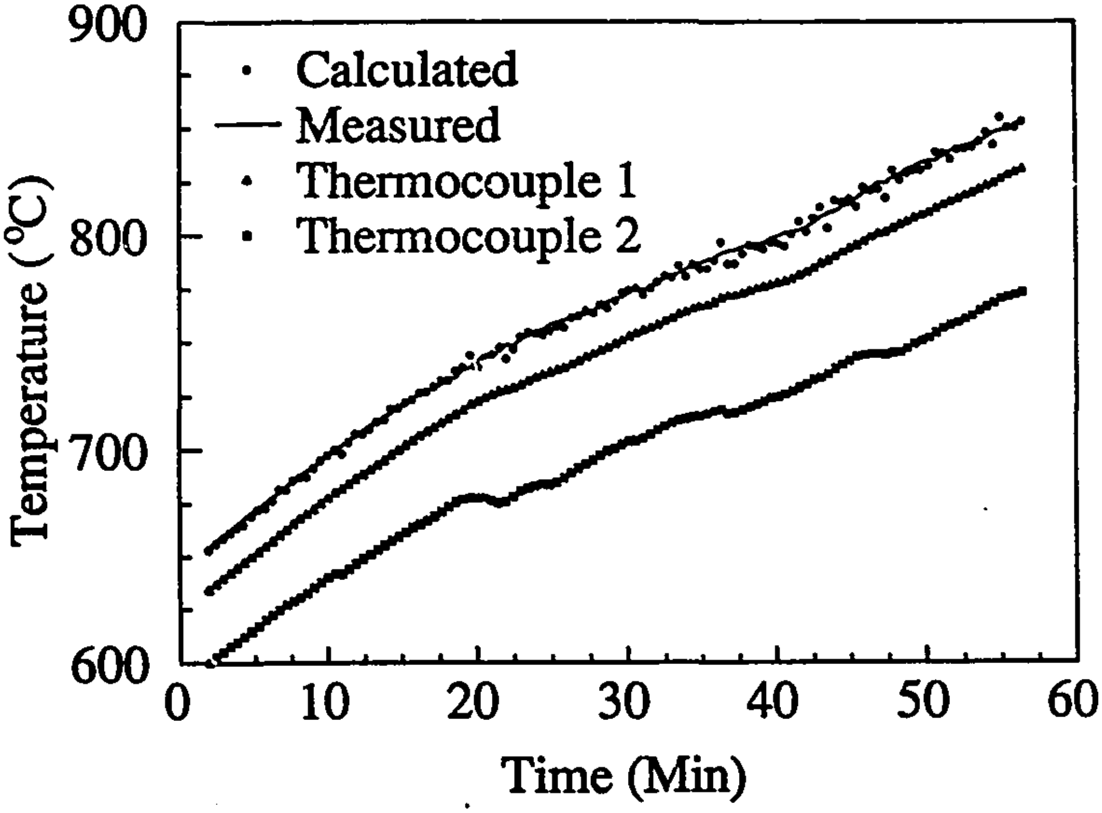

Figure 2.25: Comparison of computed and measured aluminum temperatures using the 2-D cylindrical model when $n = 0.33$.

Chapter 3

Self-Cooling Sleeve

3.1 Introduction

Molten steel in a tundish is covered by a slag layer to capture inclusions and prevent reoxidation of the steel by the atmosphere. In most instances, temperature is measured with an immersion, batch type thermocouple. Continuous temperature measurements in molten steel have been restricted by the severe corrosion which occurs at the slag line on the thermocouple sleeve. The present study was undertaken to determine the feasibility of incorporating heat pipe technology to solidify a thin layer of slag(which is not corrosive to itself) onto the heat pipe and to maintain that layer while it is in operation by the use of heat transport characteristics of the heat pipe.

Heat pipe

The concept of a heat pipe dates back to 1942 when R. Gaugler of GM Corporation, Ohio, USA filed a patent application[64] that applied to refrigeration systems. In 1963, M. Grover received a patent[65] for a device called a *heat pipe* which is more or less identical with that described in Gaugler's patent. However, he added a limited theoretical analysis and described experiments with a stainless steel heat pipe incorporating a wire mesh wick. During 1967 and 1968 several articles were published on the application of heat pipes for cooling electronics , air conditioning, engine cooling and others[66, 67, 68].

Heat pipes have had a great impact on the development of spacecraft where it is vital to redistribute temperature between the hot section and the cold section which is blocked off from the sun's rays[69, 70, 71]. Thermal gradients in the spacecraft can be minimized and the effect of external heating reduced by using heat pipes. First use of the heat pipe for satellite thermal control was on GEOS-B, launched from Vanderburg Airforce Base in 1968[72]. Two aluminum alloy heat pipes with aluminum mesh wicks and Freon 11 as the working fluid were tested to minimize the temperature differences between the various transponders in the satellite. Both showed near isothermal operation and good performance.

By 1970 a variety of heat pipes were available commercially from many companies and in the early 1970's there was growth in the application of heat pipes to solve terrestrial heat transfer problems. One of the largest engineering projects to use heat pipes was the trans-Alaska oil pipeline. About 100,000 heat pipes manufactured by McDonnell Douglas Corp. were installed during the construction to prevent thawing of the permafrost around the pipe supports for elevated sections of the pipeline. The heat pipe developed by McDonnell Douglas[73] operates in the vertical position and uses ammonia as the working fluid. Heat is transported from the ground to the radiator located above ground level. Rapid soil cooling occurs in the autumn and the soil freezes and subcools to full depth in the winter. As air temperature increased in the spring, cooling ceased.

With the technological advances in electronic equipment, devices are tending toward high power, high performance and small size. Poor dissipation of large quantities of heat generated by high power devices can result in a deterioration of performance and a lowering of the reliability of the equipment. Heat pipes have been used in the cooling of electronic elements[74], and as auxiliary cooling systems for computers[75, 76], and electronic motors[77, 78]. The Sony corporation has incorporated heat pipes in its tuner-amplifier products[79]. This is the first large scale use of heat pipes in consumer electronic equipment. The heat pipe in this application was proven to be 50 percent lighter and 30 percent higher in effectiveness as a heat sink than the conventional extruded aluminum unit.

Energy conservation is becoming important as the cost of fuel rises and reserves diminish. Heat pipes have high potential for application in the fields of thermal energy storage[80, 81, 82, 83, 84] and heat recovery systems because they can be operated almost isothermally, i.e. with a small temperature drop. There are many techniques for recovering heat from exhaust air or gas streams[85]. One of the most commonly known methods is the heat exchanger, which transfers heat from hot fluid to a cold one. Heat pipes used in heat recovery units are usually externally finned. Heat is transferred from hot exhaust air to the evaporator of the heat pipe and the heat is recovered in the condenser[86, 87]. The effectiveness of the heat pipe heat exchanger can be very high because a heat pipe can operate almost isothermally. High temperature heat pipes of ceramic material to be used in oxidizing atmospheres at temperatures in the range of 1100 to 1500 K have been tested[88]. An important application for ceramic heat pipe heat exchangers is in the processing of combustion products from industrial furnaces.

Heat pipes are devices capable of transferring large quantities of heat with very small temperature differences. Advantages of the heat pipe used as a heat transmission device are constructional simplicity, flexibility, high heat transport capability, and no need for an external pumping device. The heat pipe consists of a closed evacuated tube, porous wicking material, and a working fluid. Heating one part of the external surface leads to evaporation of the working fluid and the establishment of a pressure gradient within the heat pipe. The resulting pressure difference drives the vapor from the evaporator to the condenser where the pressure and temperature are slightly lower.

Heat transport processes in the heat pipe can be divided into four steps i.e. evaporation of the working fluid at the evaporator, flow of the vapor from the evaporator to the condenser, condensation of vapor at the condenser wall and release of the latent heat of vaporization, and the return of liquid to the evaporator by capillary action of the wick. The effective conductance of the heat pipe is several orders of magnitude higher than that of solid copper of equivalent dimensions.

The theory of heat pipes was well developed and based largely on the work of Cotter[89]. Nonetheless, there are a number of constraints on heat pipe operating parameters which are a result of the processes occurring during the operation of heat pipes. One of the most important constraints is the maximum heat transfer rate. The parameters limiting heat transport are maximum capillary pressure, sonic effect, entrainment and boiling.

In order for the heat pipe to operate continuously without drying out the wick, the maximum capillary pressure drop must exceed the sum of the pressure drop in the vapor liquid path at the working fluid.

$$\Delta P_c \geq \Delta P_l + \Delta P_v + \Delta P_g \tag{3.1}$$

where ΔP_c = surface tension pressure difference acting at the surface of the wick capillary pores that return the liquid to the evaporator from the condenser

ΔP_l = pressure drop due to the liquid flow in the wick

ΔP_v = pressure drop due to the vapor flow

ΔP_g = gravitational head which may be zero, positive or negative

This limitation on the heat transport capability of the heat pipe is known as the *capillary limitation.*

Sonic limitation has been studied by many investigators including Levy [90], Kemme[91], and Deverall et al.[92]. Kemme showed that a heat pipe can operate in a very similar manner to a converging-diverging nozzle. Sodium was used as the working fluid and the pipe was maintained at constant heat input. The heat rejection rate at the condenser was altered by changing the thermal resistance of the gas gap (i.e. varying the argon-helium ratio of the gas). By lowering the condenser temperature, he achieved sonic velocity at the end of the evaporator when it operated under a choked flow condition. Attempts to further increase the heat rejection rate only lowered the condenser temperature since the heat transfer rate of the section could not be increased because of the existence of choked flow. This demonstrated the *sonic limit* of the heat pipe.

The vapor and liquid move in opposite directions in the heat pipe. Thus at the interface between the vapor and liquid a shear force exists. The magnitude of the shear force will depend on the vapor properties and velocity. If the vapor speed is sufficiently high, liquid will be entrained in the vapor and transported to the condenser - a phenomena referred to as the *entrainment limit*. Kemme[93] observed entrainment in a sodium heat pipe and also reported hearing the sound of droplets striking the condenser end of the heat pipe with an abrupt overheating of the evaporator.

At low radial heat flux, heat transfer is primarily by condensation through the flooded wick[94]. As the radial heat flux of the heat pipe at the evaporator increases, vapor bubbles may form in the evaporator wick. The formation of vapor bubbles can cause hot spots and obstruct the circulation of the liquid. Thus there is a heat flux limit for the evaporator of a heat pipe and this limit is termed the *boiling limit*.

Heat pipes can be operated over a wide range of temperatures depending upon the working fluids as shown in Table 3.1[95]. A heat pipe shows maximum performance in the vicinity of a fluid's normal boiling point. Liquid metal working fluid is required to be operated at a relatively high temperature range. In this study sodium was chosen after considering the operating temperature range to use at high temperature. Sodium heat pipes have shown successful operation for several thousand hours using 304 stainless steel tube and screen wick[96, 97, 98, 99].

Table 3.1: Heat pipe working fluids.

Medium	Melting point (°C)	Boiling point at atmospheric pressure (°C)	Useful range* (°C)
Helium	-272	-269	-271 – -269
Nitrogen	-210	-196	-203 – -160
Ammonia	-78	-33	-60 – 100
Freon 11	-111	24	-40 – 120
Acetone	-95	57	0 – 120
Methanol	-98	64	10 – 130
Ethanol	-112	78	0 – 130
Water	0	100	30 – 200
Toluene	-95	110	50 – 200
Thermex	12	257	150 – 395
Mercury	-39	361	250 – 650
Cesium	29	670	450 – 900
Potassium	62	774	500 – 1000
Sodium	98	892	600 – 1200
Lithium	179	1340	1000 – 1800
Silver	960	2212	1800 – 2300

* The useful operating temperature range is indicative only.

Thermosyphon

A special type of heat pipe which does not use any wick structure is usually called a thermosyphon. A closed two phase thermosyphon, sometimes called a gravity assisted heat pipe, is a high-performance heat transfer device with small temperature differences associated with the latent heat of evaporation and condensation. A thermosyphon can be divided into the following three distinct zones: bottom part of the tube(evaporator zone) receives heat and generates vapor, an insulated part where counter current flow of liquid and vapor occurs (adiabatic zone), and upper portion of the tube where the vapor rises to and is condensed (condenser zone). The basic difference between heat pipes and thermosyphons is the wick structure. Because there is no wick in the thermosyphon, external forces such as gravity in most cases or centrifugal forces are required to return condensate to the evaporator section while the heat pipe uses capillary forces. Thus the evaporator zone should be lower than the condenser to enable condensate to return by gravity. Since the thermosyphon does not use a wick, it has the advantages of simplified construction, a capability of transferring large heat fluxes because of the smaller thermal resistance, wide operating limits, and low manufacturing cost.

The performance of the thermosyphon has been investigated in many publications. Much of the work is experimental in part because of the complexity involved in heat transport processes of boiling and condensation occurring in a confined space and can be classified into the following two groups.

- investigation of maximum heat transfer capacity[100, 101, 102].
- investigation of evaporation and condensation heat transfer inside the

thermosyphon[103, 104, 105, 106, 107, 108].

Maximizing heat transfer capability has received much attention by many investigators. Heat transfer capacity depends upon many variables such as geometric dimensions(shape, length and inner diameter of the tube, thickness, surface structure of the inside wall), the type and quantity of working fluid, heat flow rate, inclination angle, and operating temperature.

Nguyen-Chi and Groll[109] reviewed three operating limitations of the thermosyphon where heat transport limitations depend upon geometric dimensions, type and fill charge of working fluid, and radial heat flux. In most cases, one of the limitations of dry-out, burn-out, or entrainment (flooding) occurred.

The *dry out limit* usually occurs at the bottom of the tube and prevails for a relatively small liquid fill charge and lower radial heat flux. Dry out occurs when the quantity of the working fluid is not sufficient to complete the liquid circuit.

For relatively large fill charges and high radial heat fluxes, the *burn-out limit* may occur and is associated with pool boiling. Vapor bubbles generated in the liquid pool of the evaporator section combine to form a vapor film on the wall at certain critical heat fluxes. Because of the low thermal conductivity of the vapor a sudden increase of the evaporator wall temperature occurs.

Entrainment limit sometimes called the flooding limit is a well known operating limit in countercurrent two phase flow. It occurs for a large fill charge, high axial heat flow, but small radial evaporator heat flux. At relatively small flow rates of liquid and vapor, the liquid film is smooth and continuous. As the vapor flow is increased, the shear stress at the vapor/liquid interface increases, and the liquid film becomes wavy and unstable. The large liquid waves and instability of liquid leads to entrainment of the liquid in the vapor. The entrained liquid is carried by the vapor to the condenser and collected there. High shear stress also causes the returning of condensate flow to be stopped and leads to local dry out and ultimately to a complete dry out of the evaporator.

Lee and Mital[101] studied the effect of varying the quantity of working fluid on the resultant maximum heat fluxes. Maximum heat transfer coefficient and maximum heat flux increase with an increase in the amount of working fluid up to a certain quantity and then are independent of the amount of working fluid. Harada et al.[110] suggested that $V_e^+ = 0.25 \sim 0.3$ is desirable. By taking into account the liquid existing as a film on the condenser and adiabatic wall and as vapor in the core, H. Imura et al.[100] proposed Eq. 3.2 for calculating adequate liquid fill charge using the critical heat flux criteria which falls in the burn-out regime. Such was chosen because the critical heat flux in the burn-out regime is greater than that of the dry-out regime.

$$V_e^+ = \left[\frac{1}{5} \sim \frac{1}{3}\right] + \left[\frac{0.8l_c + l_a}{l_e} \frac{4}{d_i} \left(\frac{3\mu_l \, l_e \, q_c}{\rho_l^2 \, g \, \Delta H_v}\right)^{1/3}\right]$$

$$+\frac{\rho_g}{\rho_l}\left[\frac{l_c + l_a}{l_e} - \frac{0.8l_c + l_a}{l_e} \frac{4}{d_i} \left(\frac{3\mu_l \, l_e \, q_c}{\rho_l^2 \, g \, \Delta H_v}\right)^{1/3}\right] \tag{3.2}$$

where: V_e^+ = dimensionless fill charge: volume of working fluid divided by the volume of heated section

d_i = inside diameter of the thermosyphon tube

ΔH_v = latent heat of vaporization

l_c = length of thermosyphon condenser

l_e = length of thermosyphon evaporator

l_a = length of thermosyphon adiabatic section

q_c = critical heat flux

ρ_v = density of vapor

ρ_l = density of liquid

μ_l = dynamic viscosity of liquid

Assuming the film thickness to be much less than the radius of the tube, they derived Eq. 3.2 from the Nusselt film condensation theory. The second term on the RHS of Eq. 3.2 is the quantity of liquid film, and the third term is the quantity of vapor.

In general it is necessary to fill more than 25% of evaporator volume with working fluid to get a high heat transfer rate. Negishi and Swada[105] found that at a fill ratio of more than 70%, there were bursting sounds and violent oscillations of the tube. Those sounds were caused by a large mass of working fluid which having been pushed up to the end of the condenser by the explosive expansion of a bubble, collided with the end of the condenser. To avoid these phenomena, they recommended limiting the fill ratio to less than 60% of the evaporator volume. Water was used as the working substance in their trials.

Hahne and Gross[111] studied the influence of inclination angle on the performance of a closed two phase thermosyphon with commercial steel tube and refrigerant R 115 as a working fluid. Maximum heat flow rate was achieved when the heat pipe was tilted at a angle of 40 to 50° from the vertical. Similar results were obtained by M. Groll and Spendel[112] and Kobayashi et al.[113]. For small angles (i.e. larger tube inclination) the maximum heat flow rate decreases, however the smallest heat flow rates occur when tube is almost horizontal. It should be noted at this point that 'downhill' heat flow is not possible with a thermosyphon.

The phenomena of boiling and condensation occurring in a thermosyphon have also been studied by many investigators[103, 106, 114, 115]. Under maximum heat transport capacity, heat transfer occurs from the heating zone by nucleate boiling with very large heat transfer coefficients to the cooling zone by film condensation with much smaller heat transfer coefficients than the former one. In this case, the resistance of heat transport is dominated by the condensation process. The mechanism of film condensation heat transfer depends upon film flow which can be characterized by the film Reynolds number.

$$Re = \frac{u\delta}{\nu} \tag{3.3}$$

where u, δ, and ν are the mean velocity, thickness and kinematic viscosity of the condensate film. Mean condensation heat transfer coefficients are usually calculated from the following equation:

$$h_c = \frac{\dot{Q}}{A_c(T_v - T_c)} \tag{3.4}$$

where T_c, T_v, and A_c represent the mean temperature of cooling zone, the vapor temperature, and the area of the cooling zone respectively. In the small Re number region (Re $\leq$ 350), film flow is laminar; transition to turbulent flow occurs at high Re number(Re $\geq$ 350).

In the laminar region, the condensation heat transfer coefficient decreases when the film thickness increases due to the larger resistance of a thicker film. On the other hand, the condensation heat transfer coefficient increases as the film thickness increases in turbulent regime because turbulent exchange improves in a thicker film. Thus, an increase of heat flow rate and/or a decrease of inclination angle causes the film thickness to increase and thus would decrease the heat transfer coefficient if the film flow is laminar, but would increase it if turbulent. These phenomena were confirmed by many experimental investigations[103, 106, 114, 115] even though most were carried out in the low Re number regime.

The effect of inclination angle on a heat transfer coefficient has been studied by many investigators[106, 109, 111, 116, 117]. Andros[117] showed that as inclination angle increases, the average film thickness decreases which for laminar flow causes the heat transfer coefficient to increase. For high flow rate as inclination angle increases, heat transfer coefficient decreases because of a decrease in film thickness. Hirshberg[118] showed that the optimum angle is between 60° and 70° with low pressure($P/P_{cr} < 0.25$) while Grob[115] suggested a range of 20° to 40° at high pressure($P/P_{cr} > 0.8$).

3.2 Experimental Apparatus and Procedure

3.2.1 Material Selection

As explained in the preceding section, the three basic components of heat pipes are the working fluid, the wick or capillary structure and the container. The choice of the working fluid will normally be made based on a number of factors of which the pipe operating temperature is of major importance. Table 3.1 shows useful ranges for some working fluids. Within the approximate temperature range there may be several possible working fluids each of which in then considered with respect to the following requirements[95].

- compatibility with wick and wall materials
- good thermal stability
- wettability of wick and wall materials
- vapor pressures not too high or low over the operating temperature range
- high latent heat of vaporization
- high thermal conductivity
- low liquid and vapor viscosities
- high surface tension

A simple method for quickly comparing working fluids is to consider the Merit number[95], M, as defined by Eq. (3.5); however a high Merit number is not the only criterion. For example potassium may be chosen rather than cesium because it is more economical than cesium. Over the temperature range of 1200 - 1800 K, lithium has a higher Merit number than most metals.

However, the pipe must be made from an expensive lithium resistant alloy while sodium, on the other hand, can be used with stainless steel. Thus it may be cheaper and more convenient to use a low performance stainless steel heat pipe with sodium as the working fluid.

$$M = \frac{\rho_l \, \sigma_l \, \Delta H_v}{\mu_l} \tag{3.5}$$

where: ρ_l = density of the working fluid
σ_l = surface tension
ΔH_v = latent heat of vaporization
μ_l = viscosity of the working fluid

Water was chosen for low temperature heat pipe in the present study because of its high latent heat, surface tension and Merit number and sodium was used as the working fluid for the high temperature heat pipe.

Several factors affecting the choice material from which to fabricate the pipe are the following:

- compatibility (both with working fluid and the external environment)
- strength
- thermal conductivity
- ease of fabrication including weldability and machinability
- wettability

The temperature drop across the container wall is proportional to the wall thickness and inversely proportional to the thermal conductivity. Thus, to achieve a small temperature drop across the wall the material having a large conductance parameter, which is the product of thermal conductivity and ultimate tensile stress, is usually selected. In present study for the low temperature heat pipe, copper was chosen at first because it is compatible with water and has a high thermal conductance parameter value around the boiling point of water. Stainless steel was chosen as the pipe material for the high temperature heat pipe with sodium as the working fluid. The compatibility of stainless steel and sodium has been demonstrated by many investigators including Basiulis et al.[96] and Yamamoto[97, 119].

3.2.2 Water Heat Pipe

Copper heat pipe

A schematic of the experimental apparatus using the heat pipe made of copper is shown in Figure 3.1 and dimensions are tabulated in Table 3.2. Copper rod of 0.68 cm in diameter was placed at the center of the tube to simulate an annulus type heat pipe.

A small copper tube 0.635 cm in diameter was welded to the upper cap. The tube was used to connect to the vacuum pump and pressure transducer with SWAGELOK tube fittings. After charging 58 grams of distilled water into the heat pipe, the bottom part of the pipe was placed in dry ice until the water was frozen. The pipe was connected to a vacuum pump. Once the pipe was evacuated the valve was closed.

Tap water was used to provide cooling. A valve was used to control the flow rate and a flow meter was used to measure flow rate of cooling water. The inlet and outlet water temperatures were measured with K-type thermocouples. The heat pipe was tested in a bath of molten tin. Pure tin

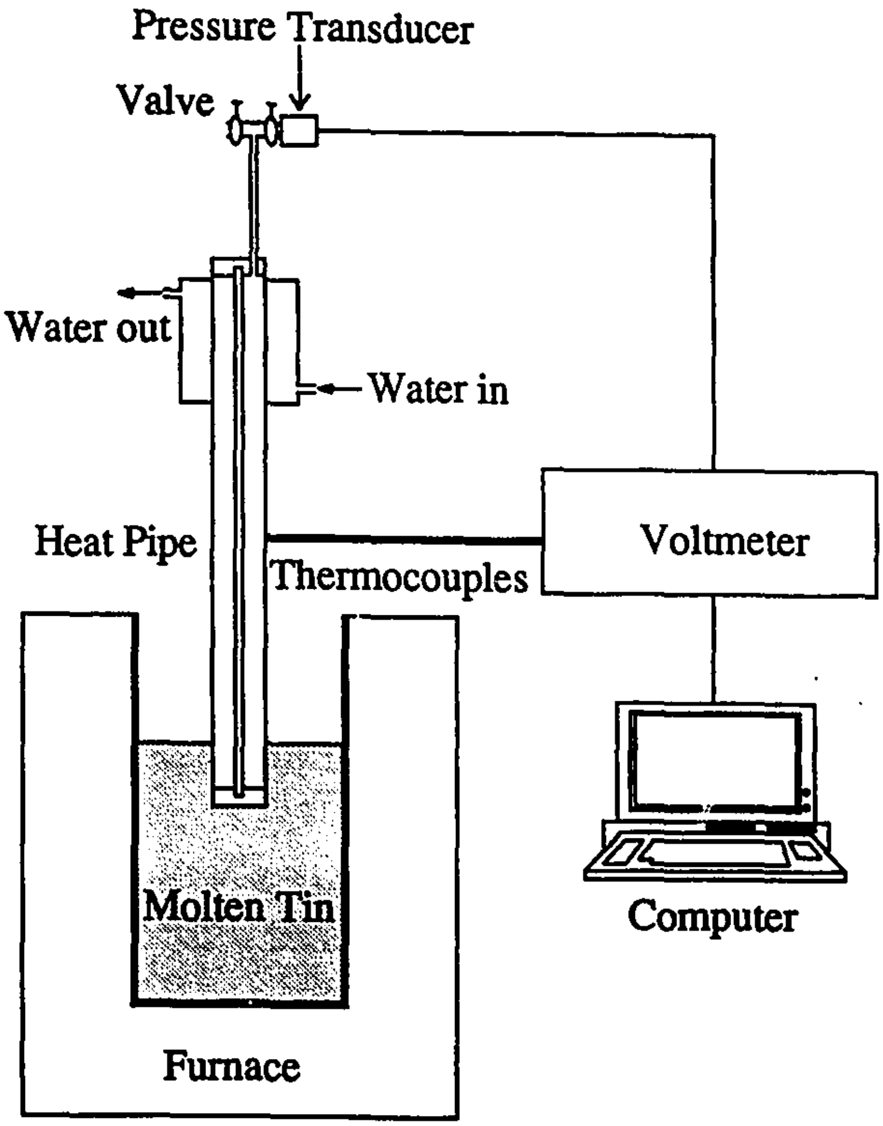

Figure 3.1: Schematic of copper heat pipe with water.

Table 3.2: Dimensions of the thermosyphons.

Pipe material	Stainless steel Type 304	Copper	Stainless steel Type 304
Working fluid	Sodium	Water	Water
Outer diameter	2.67 cm	2.86 cm	2.67 cm
Inner diameter	2.24 cm	2.606 cm	2.24 cm
Wall Thickness	0.215 cm	0.127 cm	0.215 cm
Length	60 cm	70 cm	60 cm

weighing 22 kg was charged in a crucible of 14 cm inner diameter and melted in a resistance furnace. A portion of the heat pipe was immersed in the molten tin. After reaching steady state operation, the heat pipe with a layer of frozen tin on the evaporator portion of the pipe was pulled out from the melt and a picture was taken to measure the thickness of the solid crust.

Stainless steel heat pipe

A heat pipe of 304 stainless steel was made wherein water was used as the working fluid. When water is employed as the working fluid, copper is normally used as the pipe material as was done for the previous experiments. However one of the factors in the selection of the pipe material is compatibility with the external environment. In the present study, a copper heat pipe was immersed in the molten tin bath. The copper heat pipe withstood well against dissolution once some tin was frozen onto its surface. However, the solidification of a layer of tin is not instantaneous because it takes time for the heat pipe to start up. Before the heat pipe was immersed, the bath temperature of the tin was approximately 50 °C higher than that reached after immersion and at steady state operation. Elevated melt superheat was necessary to prevent the whole bath from freezing. Some time was required to reach steady state after immersion of the heat pipe. During this time the copper heat pipe was contacted by molten tin which caused a gradual dissolution of copper into the molten tin because of the eutectic reaction.

Many researchers have built water heat pipes using stainless steel[96, 120, 121, 122, 123] and reported hydrogen evolution except with type 347 stainless steel. Hydrogen gas is non-condensable at usual operating temperatures of water heat pipes. However, the kinetics are slow and are extended over long periods of time(several thousand hours). Thus, in the present study, the evolution of hydrogen has been neglected because of the short testing times.

Stainless steel parts were cleaned by the same procedures explained in the following section and similar procedures were undertaken to assemble the heat pipe. A charge of 28 grams of distilled water was introduced into the heat pipe. The outer diameter, thickness, and the length of the pipe were 2.67, 0.215, and 60 cm respectively. A stainless steel water jacket 8.9 cm in diameter and 10 cm in length was welded to the top end of the pipe. Five K type thermocouples were spot welded on the outside and two on the inside of the water jacket of the heat pipe. Inlet and outlet water temperatures were measured to calculate the amount of the heat removed by the heat pipe.

The bath temperature was varied between 240 and 270 °C. Water flow rate ranged between 0.6 l/min and 1.9 l/min.

3.2.3 Sodium Heat Pipe

A schematic of the heat pipe is shown in Figure 3.2 and dimensions are shown in Table 3 2. A stainless steel rod that was 0.369 cm in diameter was placed at the center of the tube to simulate an annular heat pipe. Stainless steel pipe of 1.375 cm in diameter was welded to the heat pipe. A SWAGELOK to male pipe weld connector was attached to the other end of this pipe to link the valves and the pressure transducer.

The presence of contaminants either in solid, liquid or gaseous state can be harmful to heat pipe performance and life. Thus a thorough cleaning was undertaken to remove any solids and to degrease the inside of the pipe prior to assembling the parts. Stainless steel parts were cleaned by the following procedures[124]:

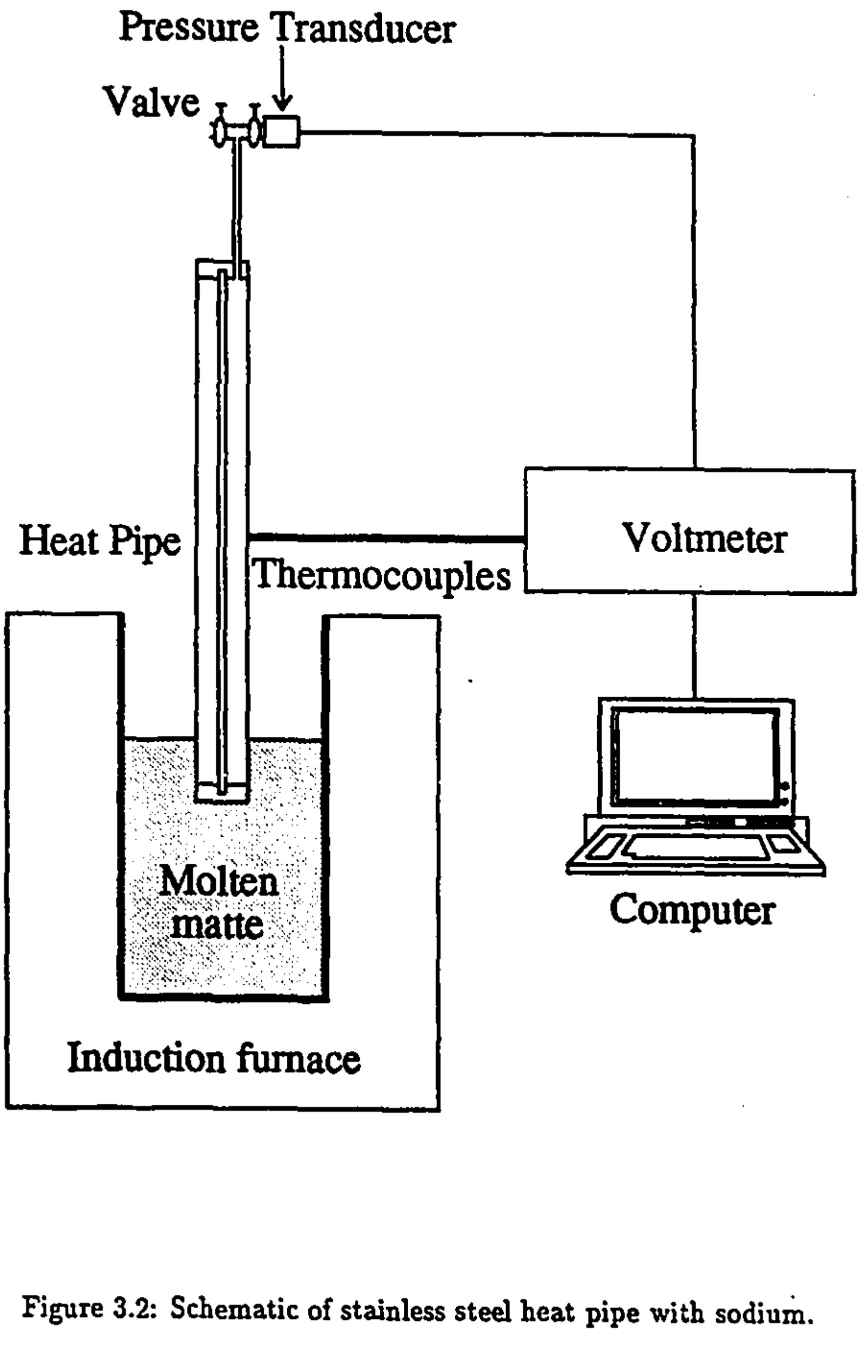

Figure 3.2: Schematic of stainless steel heat pipe with sodium.

1. Clean in 1,1,1-trichloroethane and periodically agitate and brush with bristle brush.
2. Rinse with cold trichloroethane and force dry with air.
3. Immerse in a passivating solution of sodium dichromate (7.5-30 kg/m^3) and nitric acid(15-30 % by volume)-at room temperature for 30 minutes to 2 hours followed by a tap water rinse.
4. Thoroughly dry with forced air.
5. Rinse with anhydrous isopropyl alcohol.
6. Insert wick, rinse with isopropyl alcohol, and dry as in step 4.

Two turns of 66 mesh stainless steel screen were inserted as the wick at the last stage of the cleaning process. Various methods may be used to fill the pipe with sodium which is a very reactive element. After cleaning the components of the heat pipe, pure sodium was cut into small pieces in a closed space of nitrogen gas environment to prevent oxidation of the sodium. The pieces were then put into the pipe into which nitrogen was blowing during the cutting process. One end cap of the pipe was left unwelded for easy charging of sodium and was welded immediately after charging 48.5 grams of sodium. After welding the end cap, the pipe was evacuated. The valve that was connected to the vacuum pump was closed and the side to which the valve was connected to the pump was closed by a SWAGELOK plug to prevent accidental opening.

Another bellows valve was connected to the heat pipe using SWAGELOK tube fittings and a strain gauge type pressure transducer (OMEGA, PX 176-

025A5V) was attached to measure the pressure inside the pipe. Six chromel-alumel thermocouples were placed on the outside of the pipe at 10, 15, 25, 35, 45, and 53 cm away from the bottom edge of the pipe. Thermocouples and pressure transducer outputs were monitored and recorded continuously by the HP 3497A data acquisition/control unit and the HP 85A microcomputer.

Although the heat pipe was designed to operate in molten steel, it was first tested without immersing it into molten metal. The lower part of the heat pipe was heated in an induction coil(TOCCO). Lower 8 cm of the pipe was exposed to the induction field.

In addition to the above testing, the heat pipe was also tested in a bath of molten copper matte. The heat pipe was lowered into the copper matte to an initial depth of 3.5 cm. It was pulled out from the molten matte and the thickness of the solid crust was measured. After measuring the thickness of the solid crust, the heat pipe was put into the molten matte to a depth of 7.0 cm. The heat pipe was pulled out after reaching steady state and thickness measurements were again made.

3.3 Results and Discussions

3.3.1 Heat Pipes Using Water

Copper heat pipe

Table 3.3 shows calculated results from the copper heat pipe experiments. Since the copper pipe was dissolved gradually into the tin bath by the eutectic reaction, only two different experiments were performed successfully. The immersion depth of the heat pipe was 6.5 cm and the tin bath temperature was 260 °C. Heat flow rates were calculated with cooling water flow rates and temperature differences between inlet and outlet water. Condensation heat transfer coefficients(h_c) were calculated using Eq. (3.4). Vapor temperature at the cooling zone was taken from the temperature of the thermocouple located at the adiabatic section. Cooling zone temperature was taken from the thermocouple reading located at the cooling chamber.

Figures 3.3 and 3.4 show the temperature and pressure changes of the heat pipe and the solid tin crust after reaching steady state operation. Once the heat pipe was removed from the tin bath, the pressure inside the pipe decreased rapidly and the bath temperature of the liquid tin increased. In general, the heat pipe was operating around 110 °C and transporting about 2 kW of energy.

To estimate the thickness of the solid tin shell, a simple calculation can be done as follows. From the known heat flow rate and the wall temperature inside the tin shell, the shell thickness was calculated assuming one-dimensional heat conduction. Energy equation for cylindrical coordinates can be written as

$$\frac{1}{r}\frac{\partial}{\partial r}\left(kr\frac{\partial T}{\partial r}\right)+\frac{1}{r^2}\frac{\partial}{\partial \phi}\left(k\frac{\partial T}{\partial \phi}\right)+\frac{\partial}{\partial z}\left(k\frac{\partial T}{\partial z}\right)+\dot{q}=\rho C_p\frac{\partial T}{\partial t} \qquad (3.6)$$

For steady state condition, with no heat generation, the appropriate 1-D form of the heat equation is

$$\frac{1}{r}\frac{\partial}{\partial r}\left(kr\frac{\partial T}{\partial r}\right)=0 \qquad (3.7)$$

From Fourier's first law, the rate of energy transferred across the cylindrical surface in the solid is

$$q_r = -kA\frac{\partial T}{\partial r} = -k(2\pi rL)\frac{\partial T}{\partial r} \tag{3.8}$$

where $A(= 2\pi rL)$ is the area normal to the direction of the heat flow and k is thermal conductivity. The temperature distribution throughout the solid can be determined by solving Eq. (3.7). Assuming k is constant, Eq. (3.7) can be integrated twice to arrive at the general solution such that

$$T_r = C_1 lnr + C_2 \tag{3.9}$$

Two boundary conditions are

$$T_{r_1} = T_1 \qquad\qquad T_{r_2} = T_2 \tag{3.10}$$

By applying these two boundary conditions in Eq. (3.9), T_r can be determined as:

$$T_r = \frac{T_1 - T_2}{ln(r_1/r_2)}\, ln\left(\frac{r}{r_2}\right) + T_2 \tag{3.11}$$

By substituting Eq. (3.11) into Fourier's law, Eq. (3.8), the heat flow rate can be expressed as:

$$q_r = \frac{2\pi Lk(T_1 - T_2)}{ln(r_2/r_1)} \tag{3.12}$$

From Eq. (3.12), the ratio of the radii can be calculated with known heat flow rate(q_r), thermal conductivity of the tin(k), and the temperature difference between the solidification temperature of the tin and the thermocouple reading taken on the heat pipe surface underneath the tin shell. The heat pipe depth(L) is the equivalent depth which takes into account the immersion depth and the area of the end cap. Thus

$$L = L_i + \frac{d_o}{4}$$

where L_i is the immersion depth and d_o is the outer diameter of the pipe. Thus, from Eq. (3.12) the ratio of the radii can be estimated.

In both cases the estimated values of the ratio of the radii were smaller than those of experiments. Table 3.3 also shows the Nusselt numbers for the condensation process occurring in the condenser section. The details of the Nusselt number can be found in next section. Nusselt numbers from the experiments are comparable with those that were calculated.

Table 3.3: Calculations of some variables relevant to copper heat pipe experiment.

Exp. #	Water flow rate l/min	Inlet water temperature °C	Outlet water temperature °C	Heat flow rate W
C-1	0.915	24.7	53.3	1824
C-12	1.88	21.7	37.1	2019

Exp. #	Heat flow rate W	Wall temperature °C	r_2/r_1 Experimental	r_2/r_1 Calculated
C-1	1824	193.3	2.7	1.8
C-12	2019	175.4	3.1	2.2

Exp. #	Heat flow rate W	T_v °C	T_c °C	h_c W/m^2 °C
C-1	1824	115.2	98.2	6579.8
C-12	2019	107.4	80.5	4594.2

Exp. #	Re	Nu Experimental	Nu Calculated	Nu_{cal}/Nu_{exp}
C-1	35.5	0.20	0.21	1.05
C-12	39.3	0.14	0.20	1.42

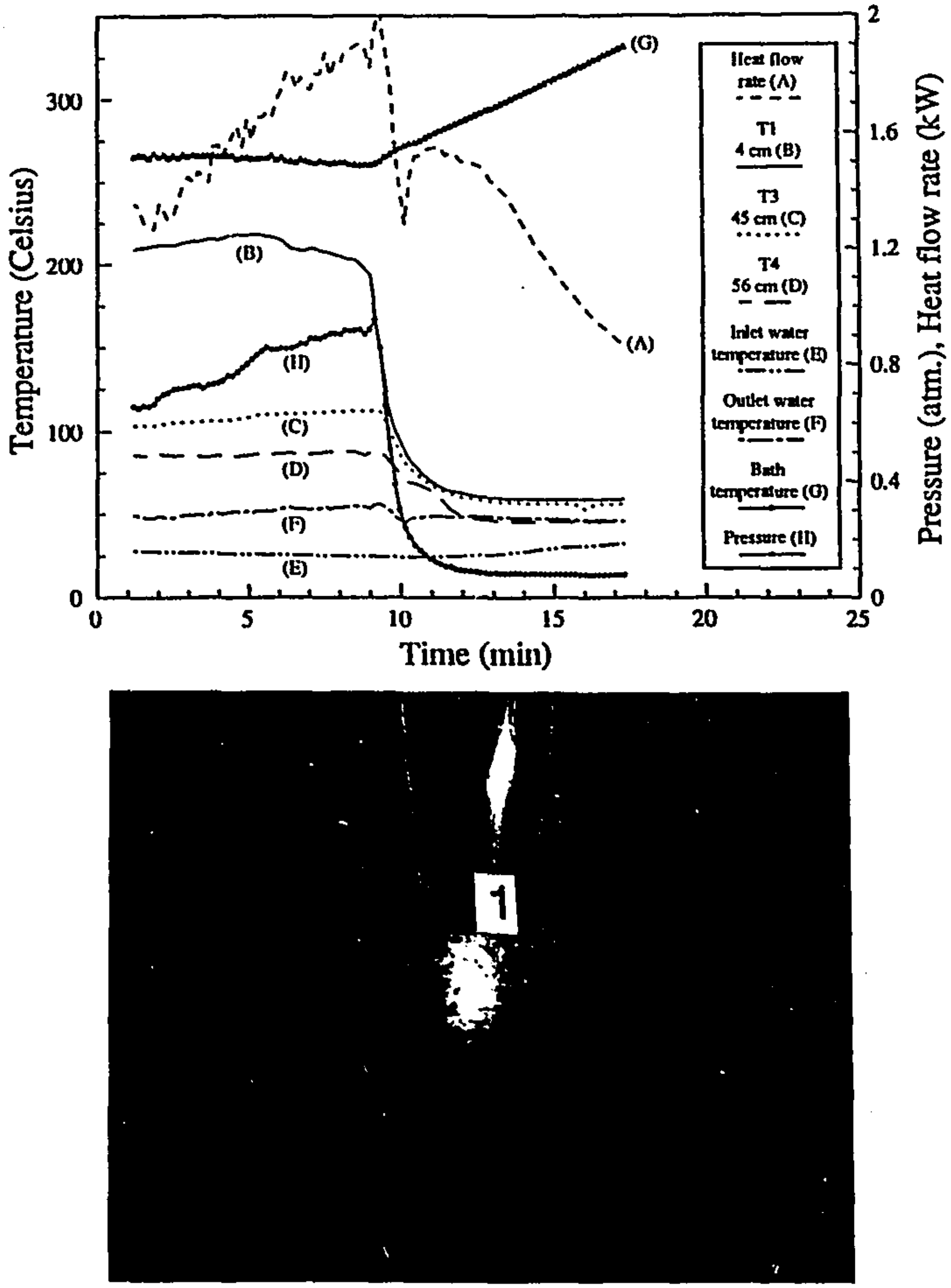

Figure 3.3: Temperature and pressure response curves for Exp. C-1. Also shown is a photograph of the solid tin crust at the end of the experiment.

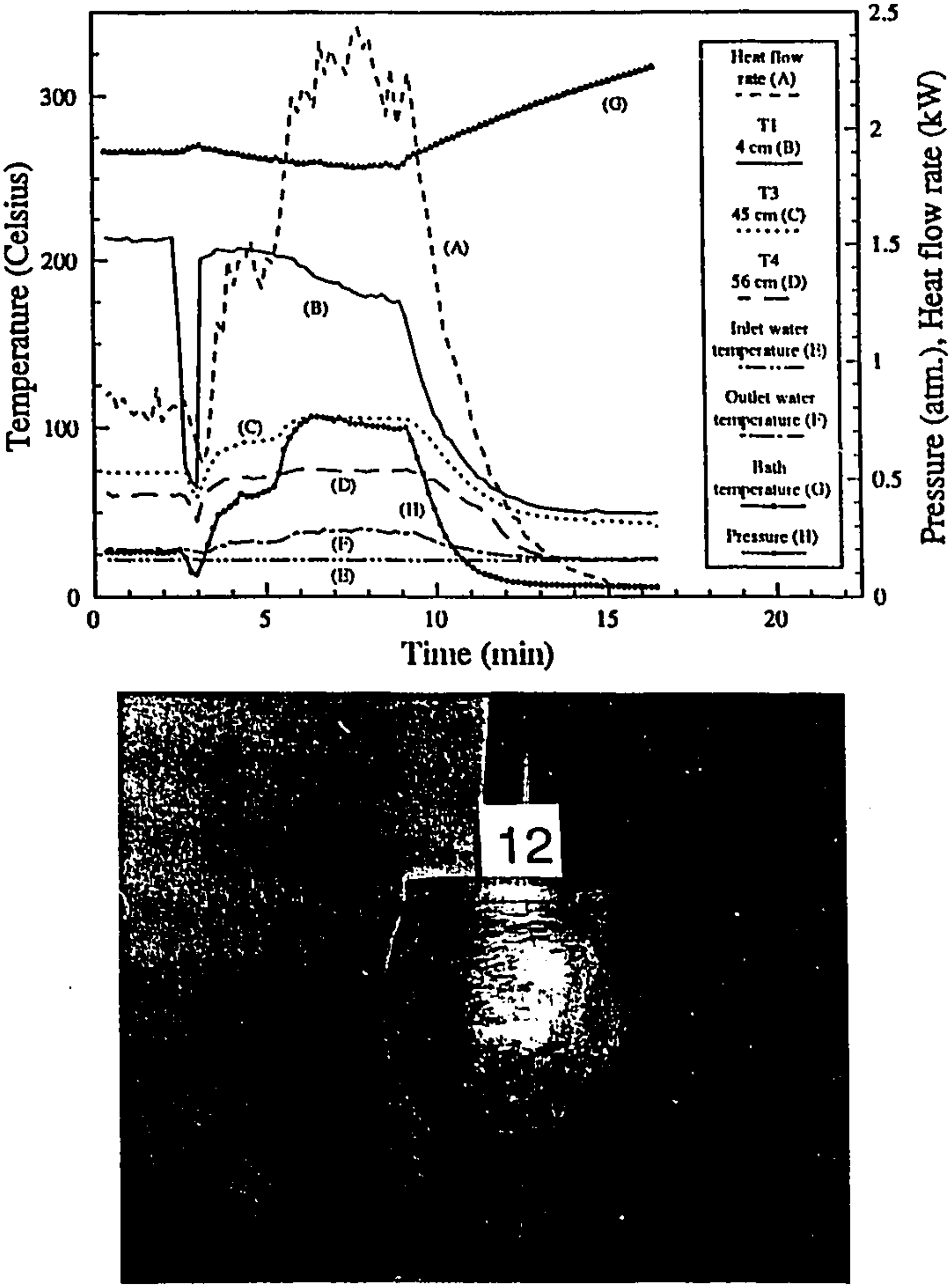

Figure 3.4: Temperature and pressure response curves for Exp.C-12. Also shown is a photograph of the solid tin crust at the end of the experiment.

Stainless steel heat pipe

Tests were conducted with the stainless steel heat pipe for a range of conditions. Experimental conditions are tabulated in Table 3.4. The depth of immersion of the heat pipe was set at two different values and the flow rate of water in the cooling chamber was varied over three values. The bath temperature of the molten tin was varied over a range from 240 to 270 °C.

Results for these experiments are shown in Figures 3.7 through 3.19. Each figure consists of a photograph and graph showing the changes in the system as it moved toward steady-state operation. The photographs were used to measure the thickness of the tin shell.

Calculations of heat flow rates are shown in Table 3.5. The heat pipe was carrying energy over a range of 700 to 1400 W.

Figures 3.5 and 3.6 show the effect of bath temperature on heat pipe wall temperature distribution along the pipe. As the bath temperature increases the wall temperature under the solid shell increases. However the wall temperature of the adiabatic section (46 cm away from the bottom) shows relatively constant temperature with respect to the bath temperature changes.

Both operating temperature of the pipe and the temperature of the cooling chamber are decreased by increasing cooling water flow rate. The higher cooling water flow also causes lower internal vapor pressure and lower heat flow rate. Lower heat flow rates at higher cooling water flow are due to the lower internal vapor pressure.

Table 3.4: Experimental Conditions of experiments with stainless steel heat pipe.

Exp. #	Bath temperature °C	Water flow rate l/min	Immersion depth cm
1	272	1.2	5
2	249	0.6	5
3	261	1.2	5
4	249	1.2	7.5
6	263	1.2	7.5
8	240	1.9	7.5
9	247	1.9	7.5
10	261	1.9	5
11	260	1.2	5
12	249	1.2	5
13	255	1.9	5
14	243	1.2	5
15	252	1.9	5

Table 3.5: Calculations of heat flow rate.

Exp. #	Water flow rate l/min	Inlet water temperature °C	Outlet water temperature °C	Heat flow rate W
1	1.2	14.4	26.8	1029
2	0.6	16.5	33.1	716
3	1.2	13.7	24.1	858
4	1.2	15.2	32.4	1421
6	1.2	14.8	30.5	1296
8	1.9	6.8	17.3	1396
9	1.9	6.7	14.3	1006
10	1.9	6.5	13.0	861
11	1.2	8.3	20.6	1018
12	1.2	8.4	23.5	1252
13	1.9	6.9	12.9	807
14	1.2	8.3	20.6	1018
15	1.9	7.1	12.3	698

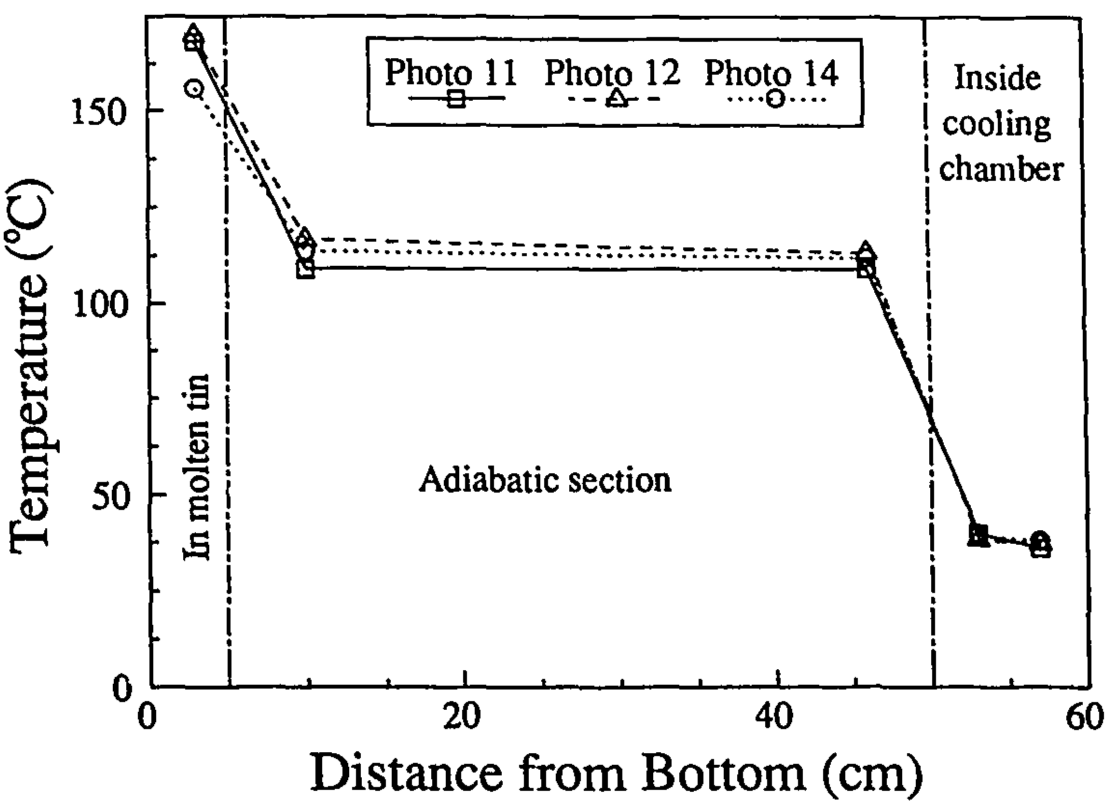

Figure 3.5: Effect of bath temperature on heat pipe wall temperature distribution (Water flow rate = 1.2 *l*/min).

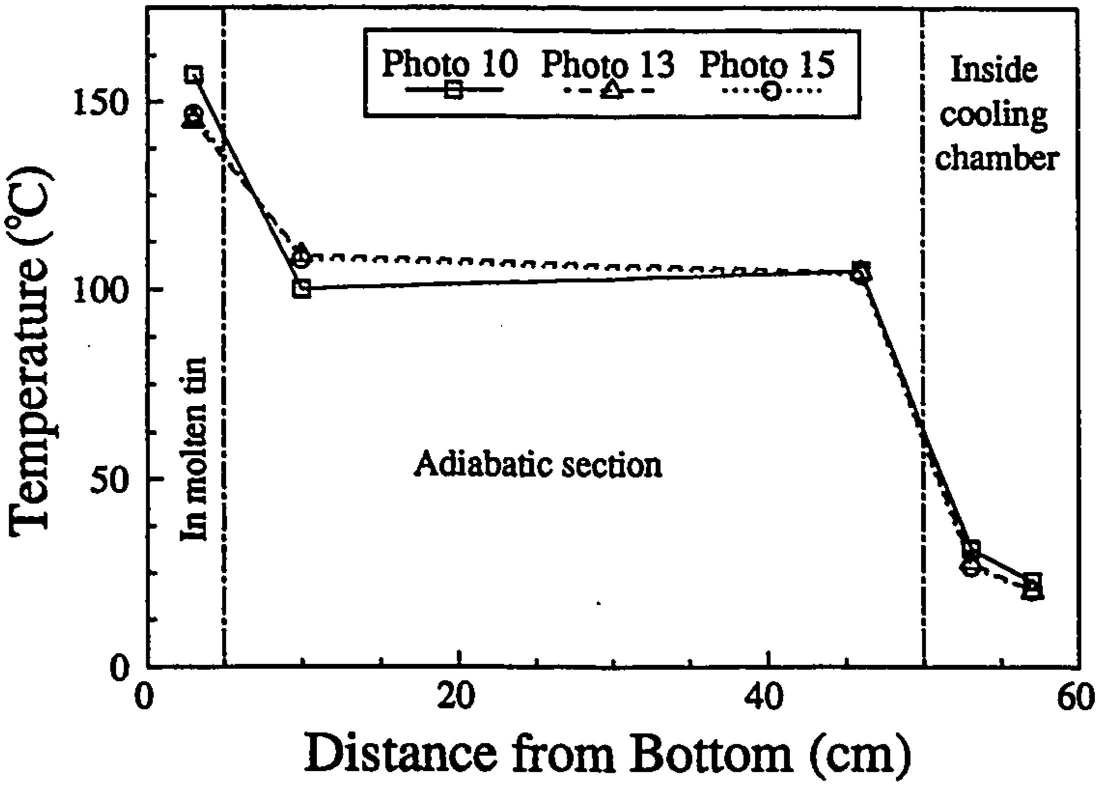

Figure 3.6: Effect of bath temperature on heat pipe wall temperature distribution (Water flow rate = 1.9 l/min).

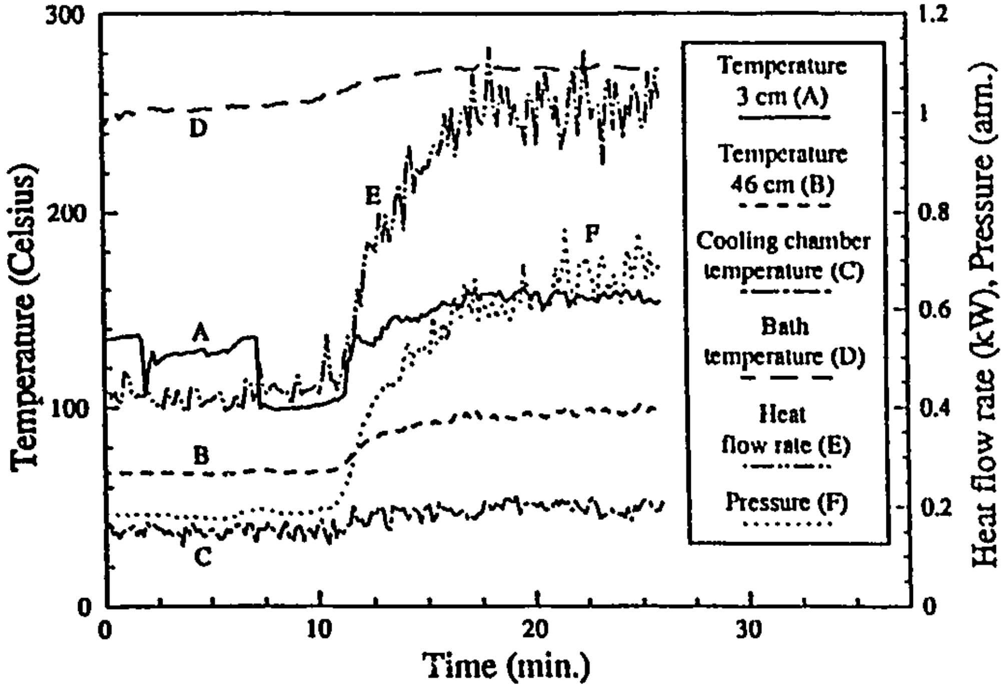

Photo 1

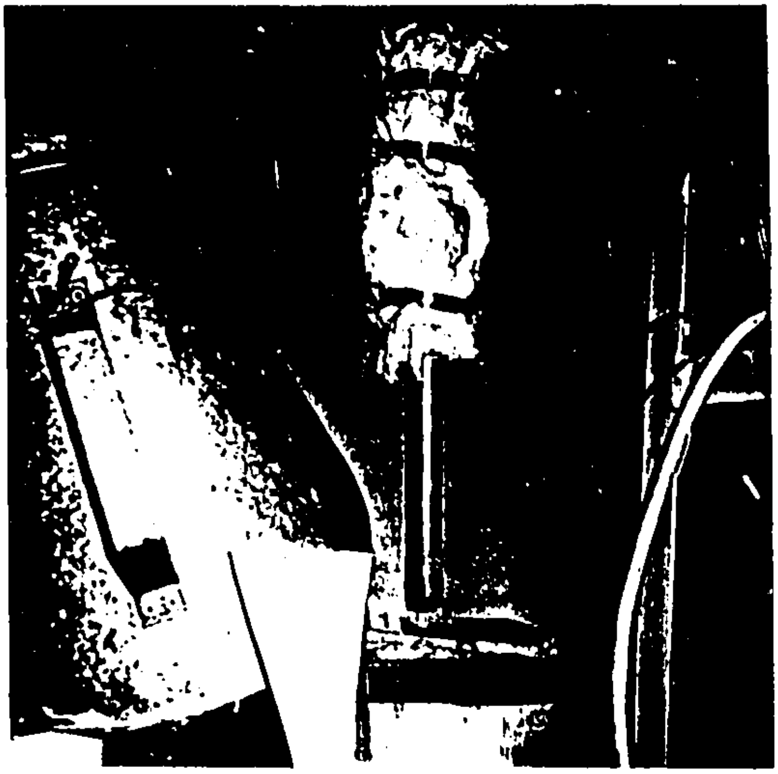

Figure 3.7: Temperature and pressure response curves for Exp. 1. Also shown is a photograph of the solid tin crust at the end of the experiment.

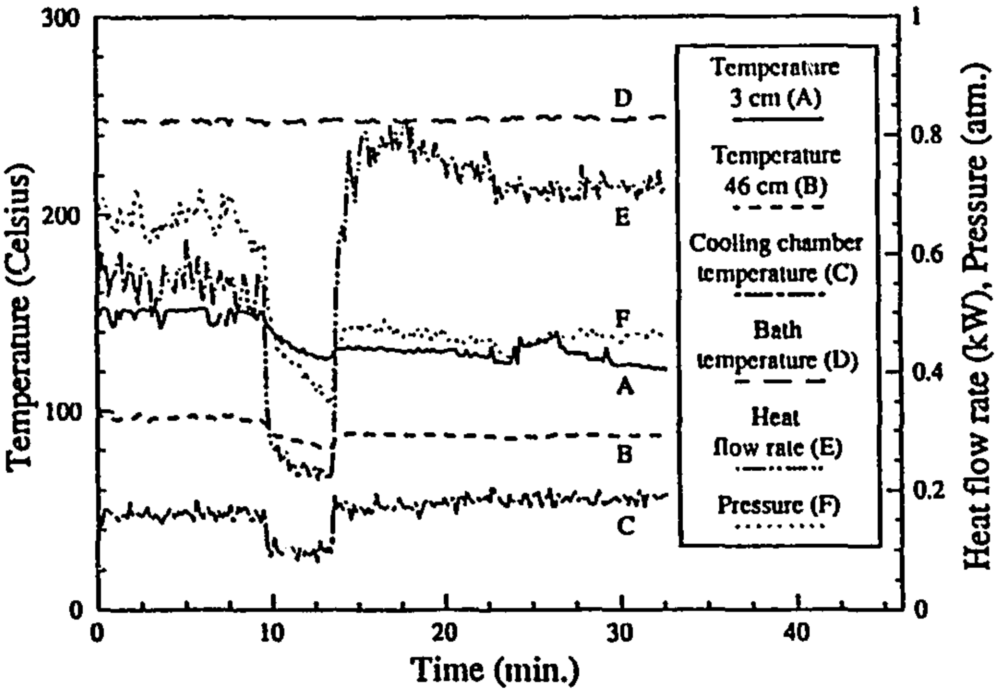

Photo 2

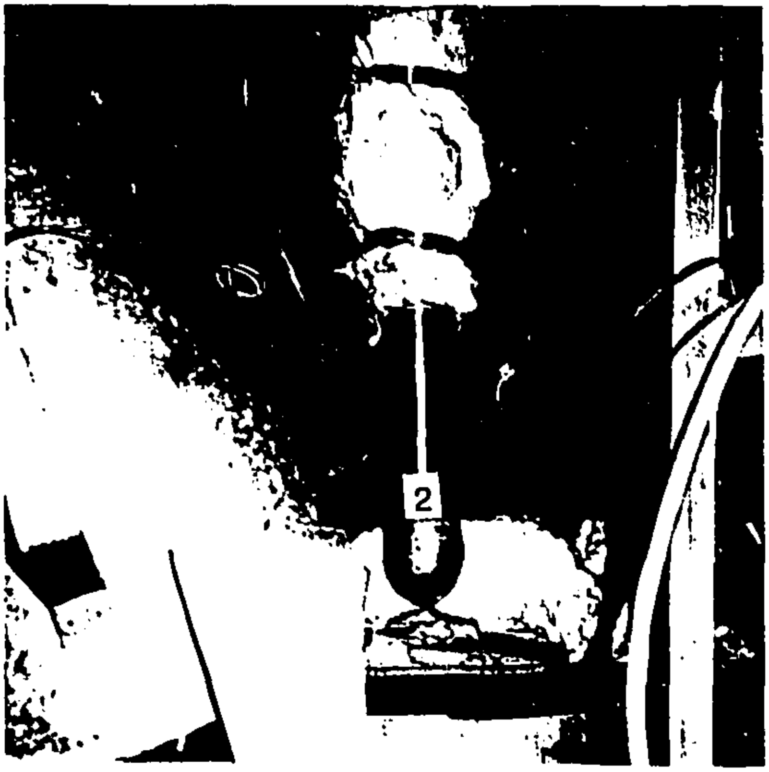

Figure 3.8: Temperature and pressure response curves for Exp. 2. Also shown is a photograph of the solid tin crust at the end of the experiment.

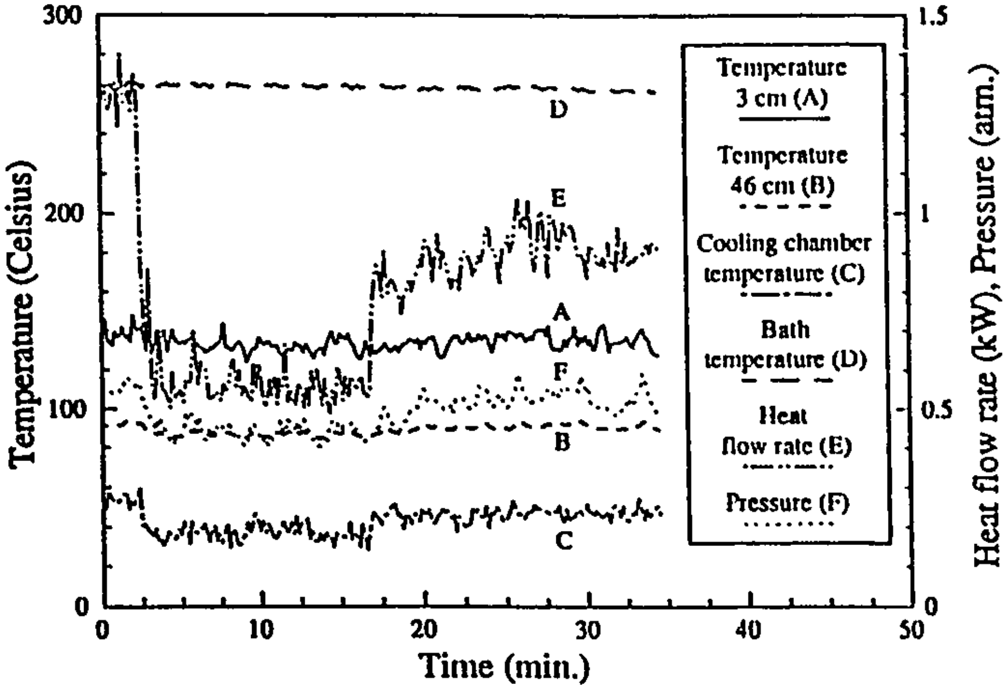

Photo 3

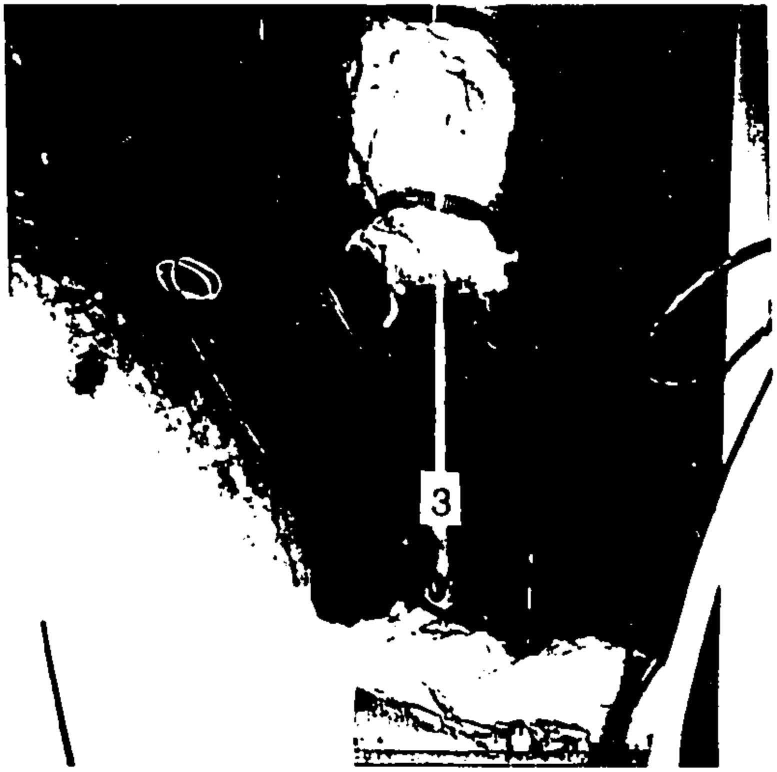

Figure 3.9: Temperature and pressure response curves for Exp. 3. Also shown is a photograph of the solid tin crust at the end of the experiment.

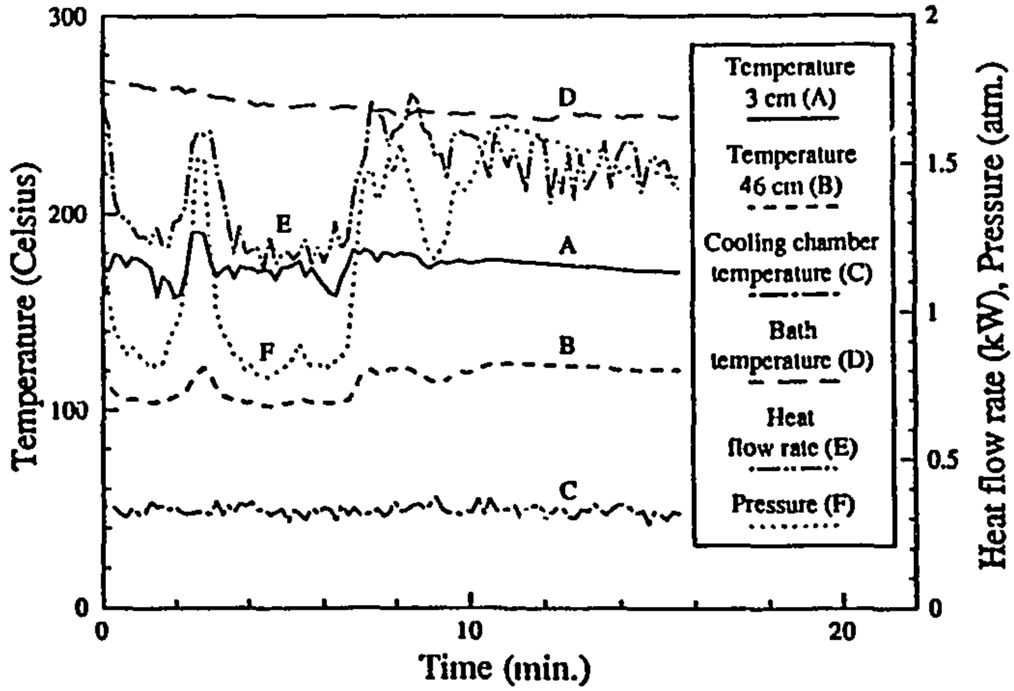

Photo 4

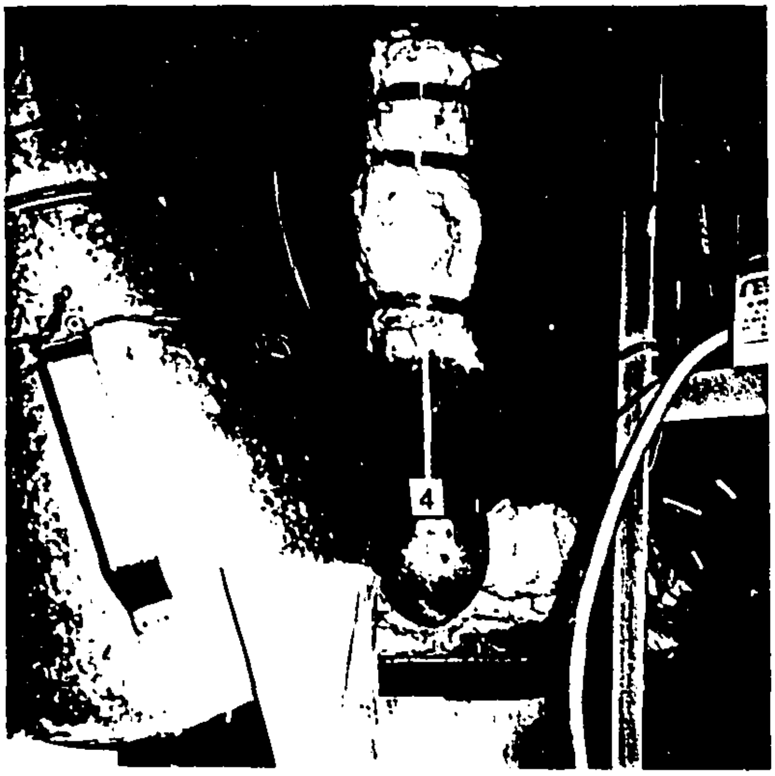

Figure 3.10: Temperature and pressure response curves for Exp. 4. Also shown is a photograph of the solid tin crust at the end of the experiment.

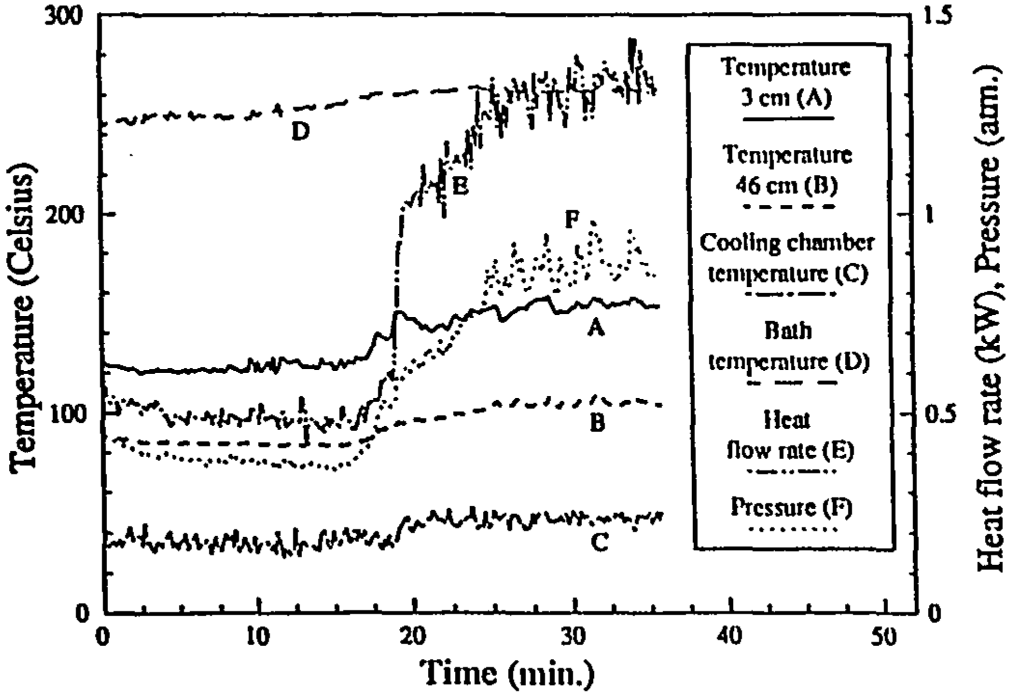

Photo 6

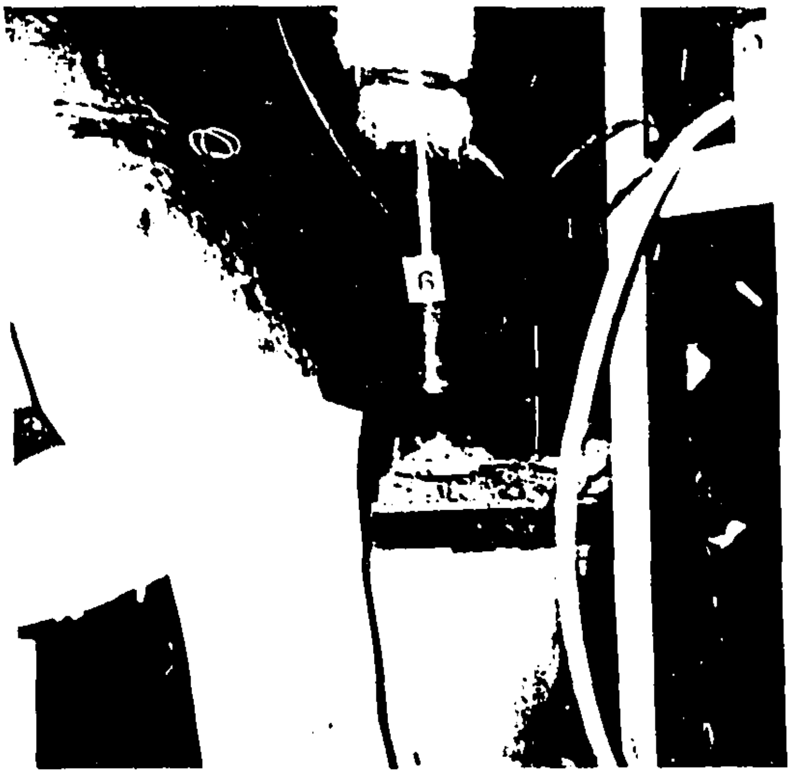

Figure 3.11: Temperature and pressure response curves for Exp. 6. Also shown is a photograph of the solid tin crust at the end of the experiment.

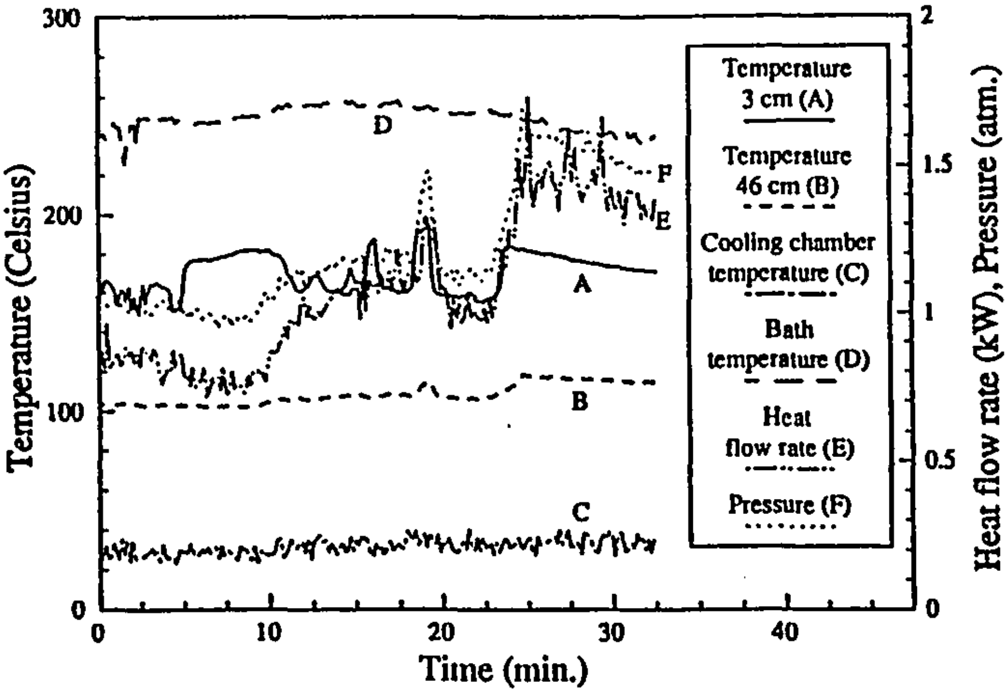

Photo 8

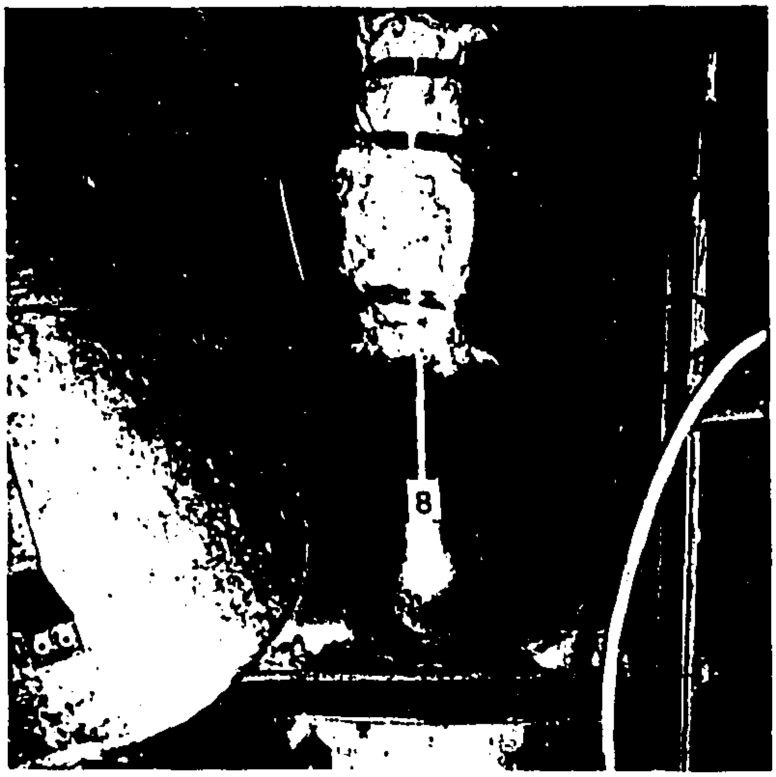

Figure 3.12: Temperature and pressure response curves for Exp. 8. Also shown is a photograph of the solid tin crust at the end of the experiment.

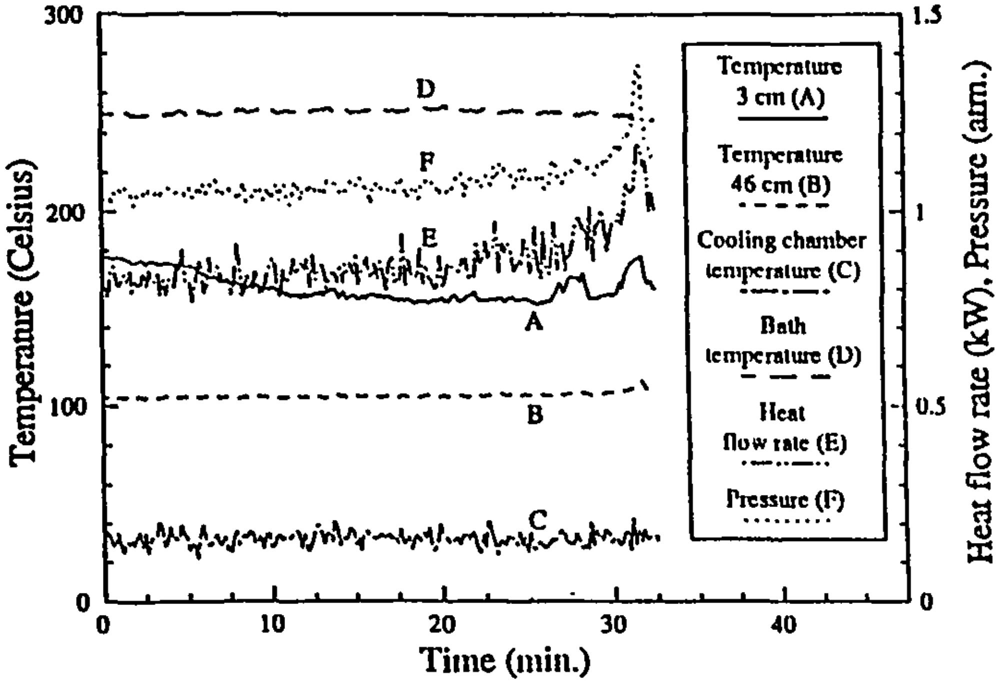

Photo 9

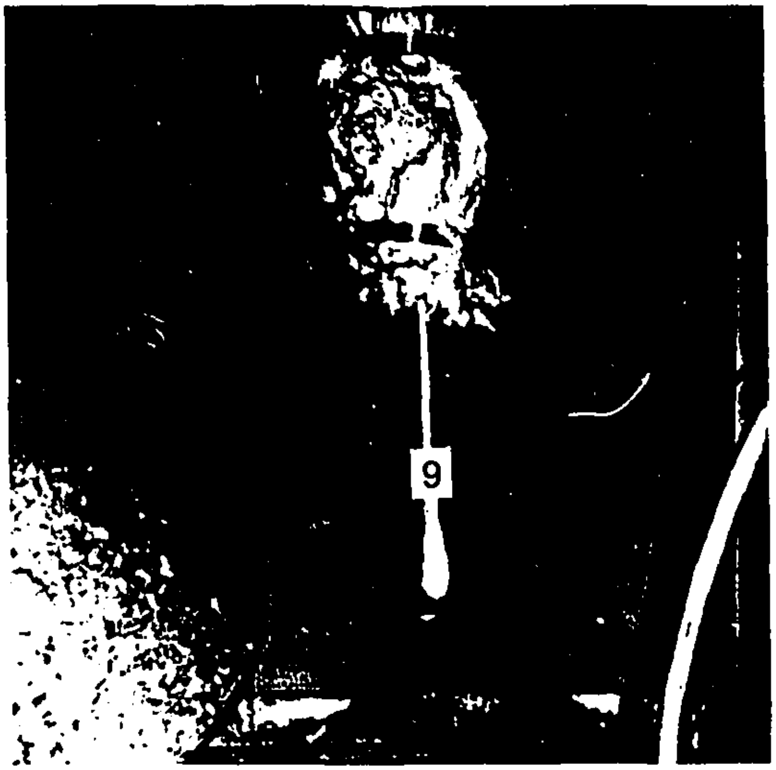

Figure 3.13: Temperature and pressure response curves for Exp. 9. Also shown is a photograph of the solid tin crust at the end of the experiment.

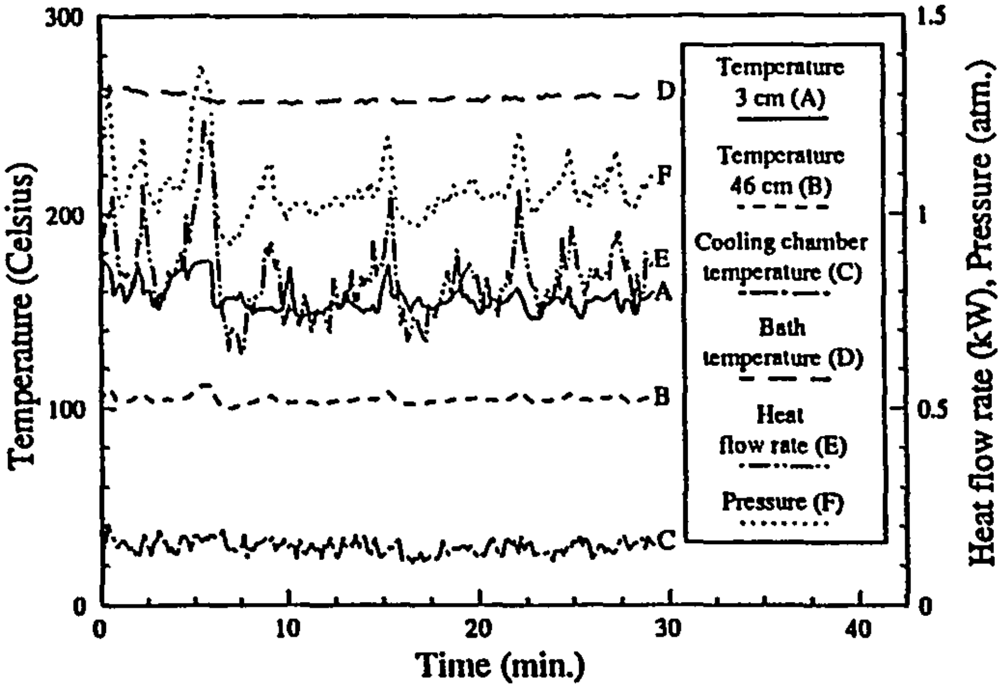

Photo 10

Figure 3.14: Temperature and pressure response curves for Exp. 10. Also shown is a photograph of the solid tin crust at the end of the experiment.

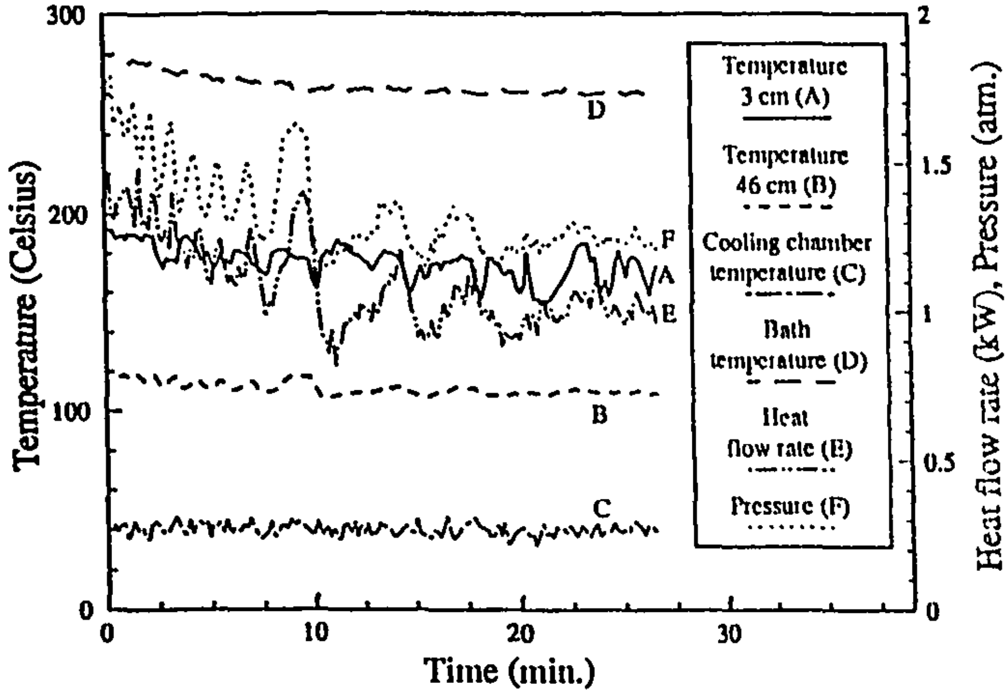

Photo 11

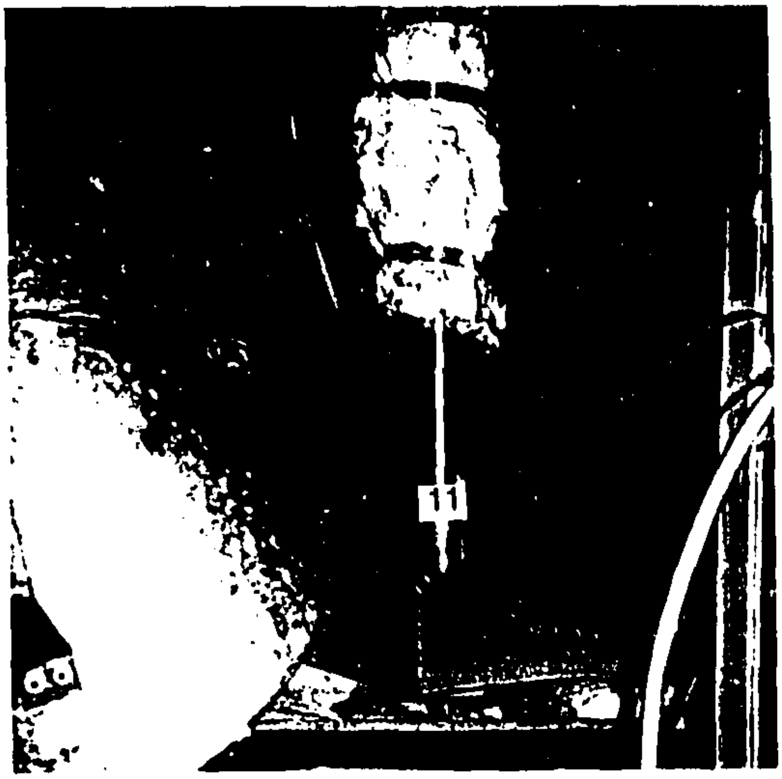

Figure 3.15: Temperature and pressure response curves for Exp. 11. Also shown is a photograph of the solid tin crust at the end of the experiment.

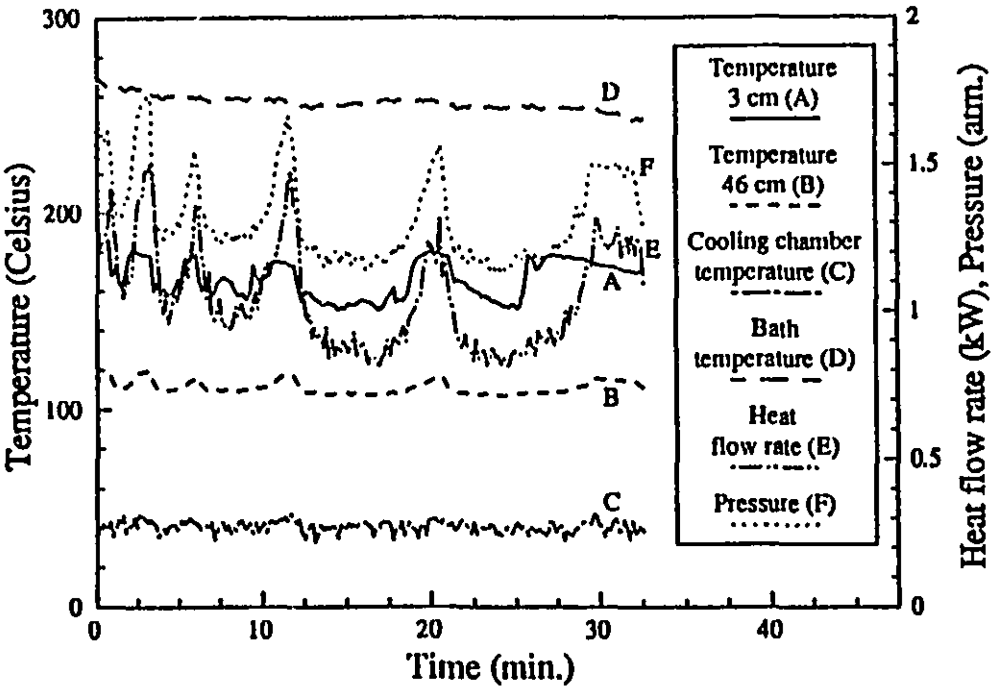

Photo 12

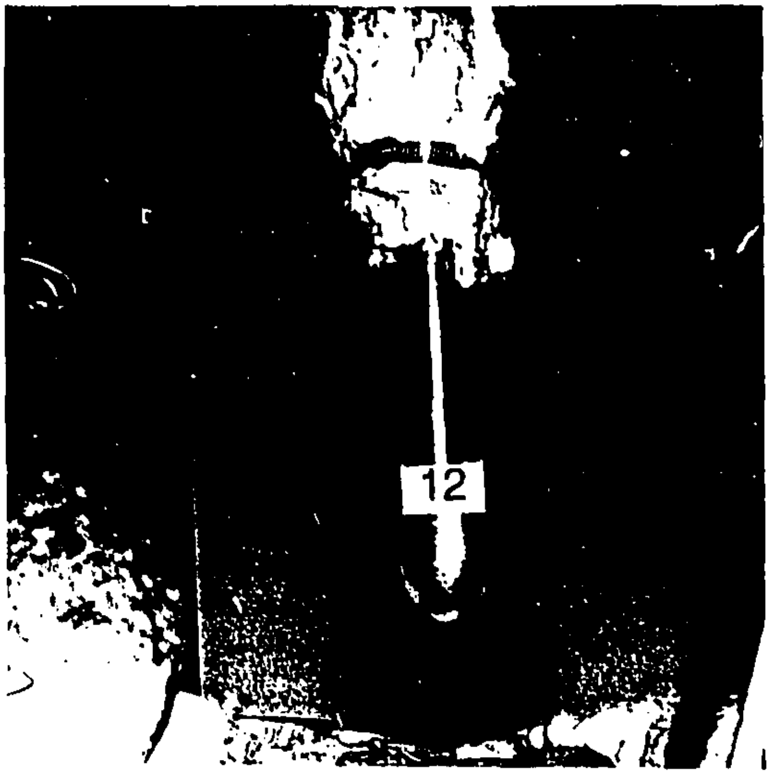

Figure 3.16: Temperature and pressure response curves for Exp.12. Also shown is a photograph of the solid tin crust at the end of the experiment.

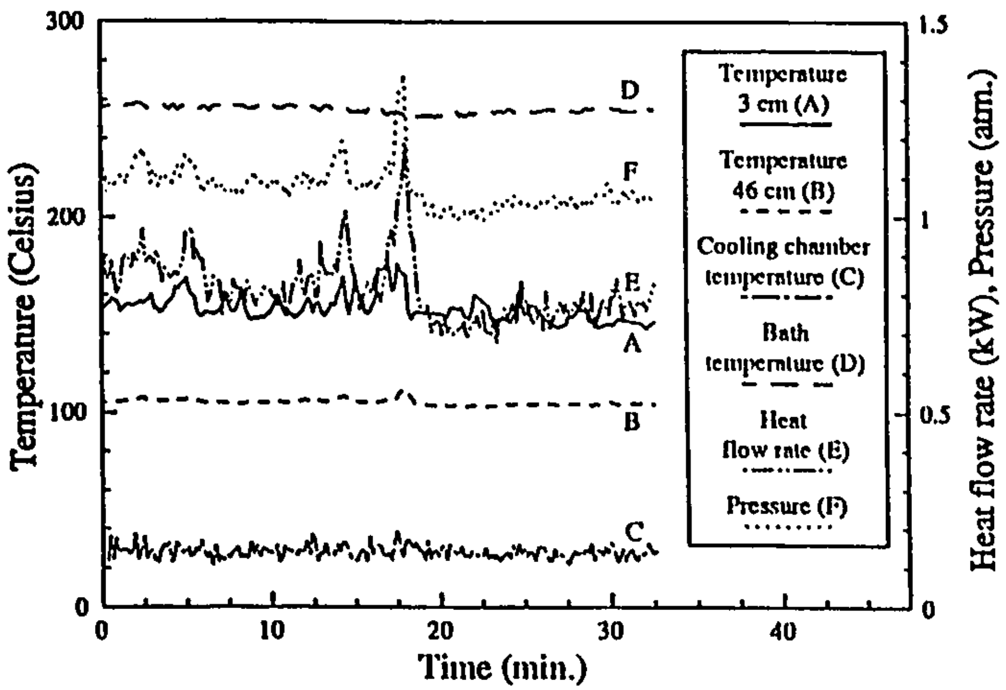

Photo 13

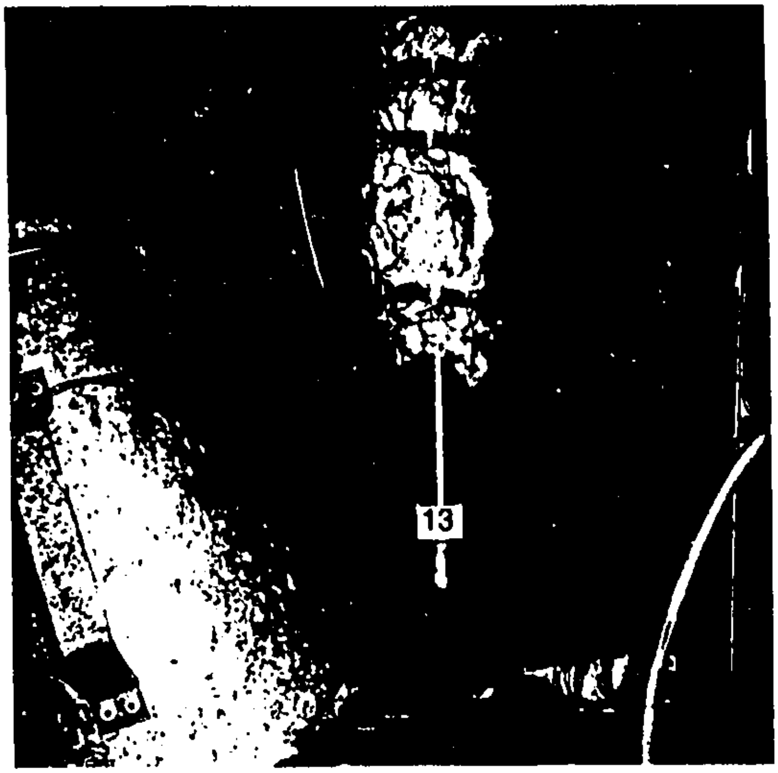

Figure 3.17: Temperature and pressure response curves for Exp. 13. Also shown is a photograph of the solid tin crust at the end of the experiment.

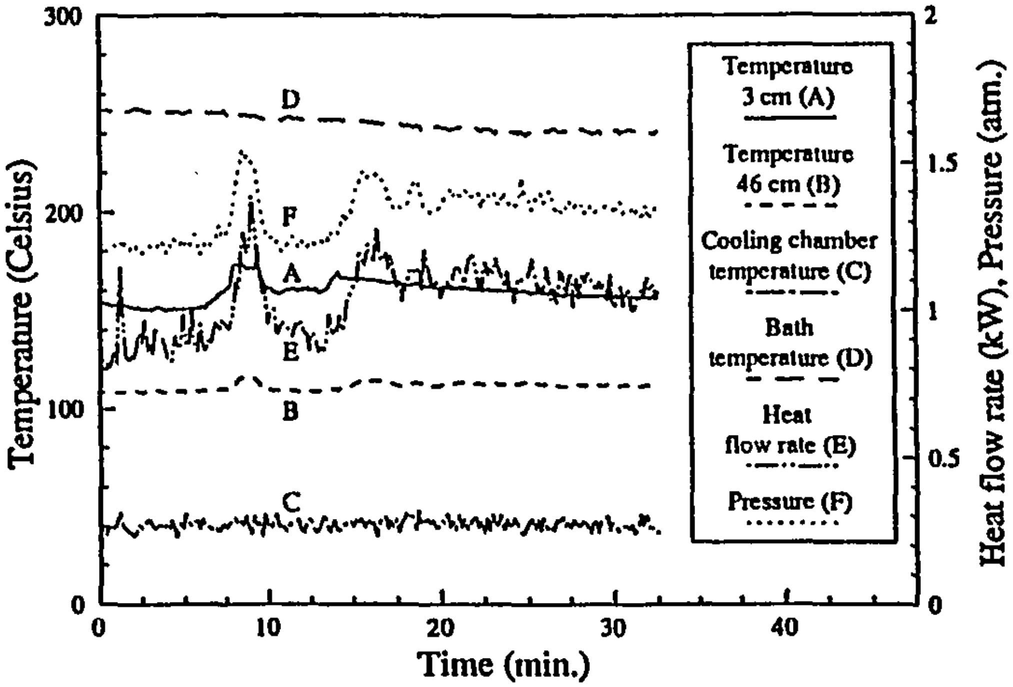

Photo 14

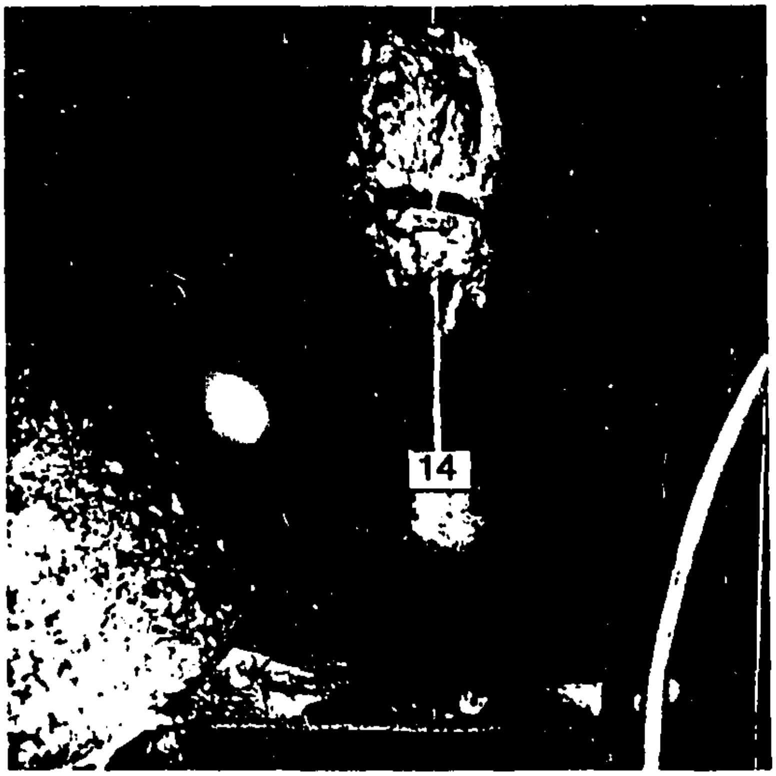

Figure 3.18: Temperature and pressure response curves for Exp. 14. Also shown is a photograph of the solid tin crust at the end of the experiment.

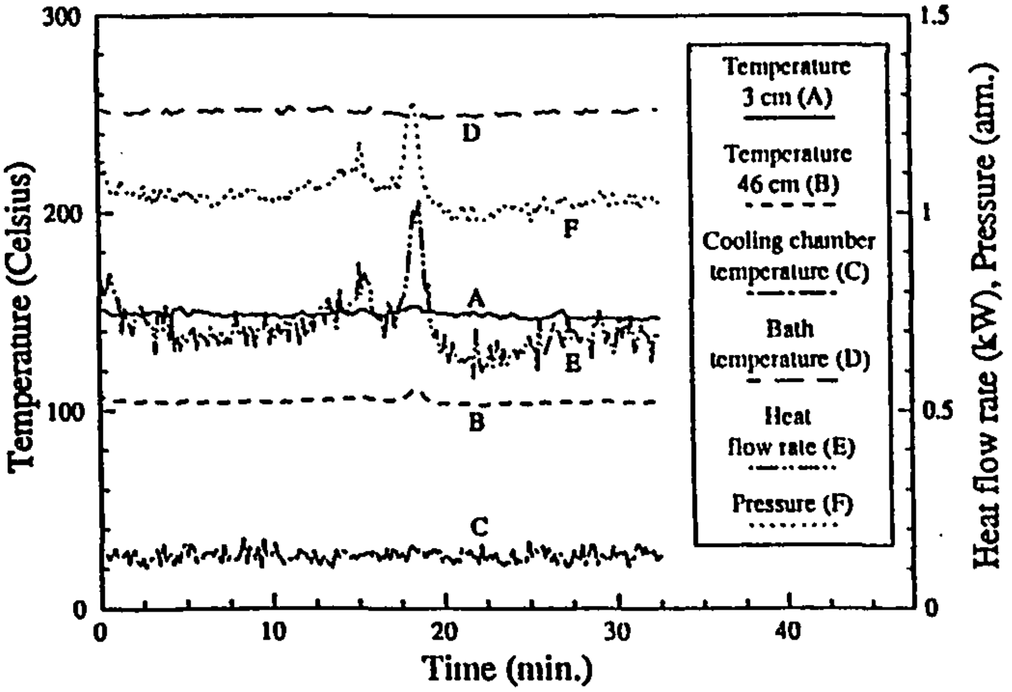

Photo 15

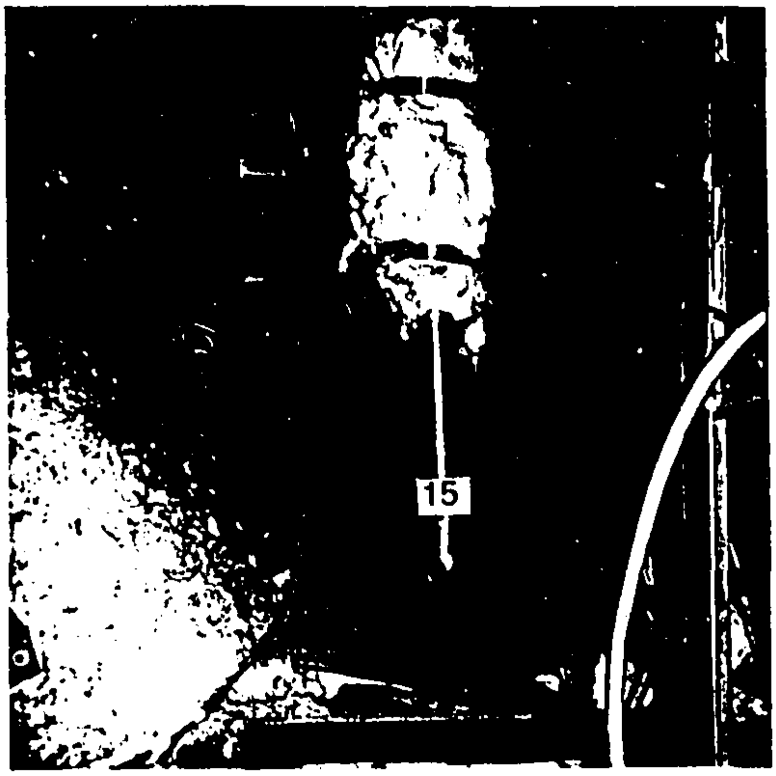

Figure 3.19: Temperature and pressure response curves for Exp. 15. Also shown is a photograph of the solid tin crust at the end of the experiment.

The effects of operating temperature on heat flow rates are shown in Figures 3.20 and 3.21. The heat flow rate increases appreciably with an increase in operating temperature. This was expected because the boiling heat transfer coefficient increases with increasing pressure.

Calculations of solid shell thickness

Table 3.6 shows the calculated and experimental ratios of radii using Eq. (3.12). Calculated values are substantially larger than experimental ones except for those of experiments #4, 8, 12, and 14. The differences between the calculated and experimental values are considered mainly due to the contact resistance occurring at the two adjacent metals. When heat conducts through two adjacent metals, it is usually necessary to consider a contact resistance since it creates a temperature gradient at the interface. Figure 3.22 shows the gap between two metals in contact.

Interfacial conductance is defined as

$$h_{ic} = \frac{q_r}{\Delta T_i \, A_c} \tag{3.13}$$

A fictitious interfacial temperature drop (ΔT_i) is taken as the temperature difference between T_1 and T_2. For perfect contact the temperature drop (ΔT_i) vanishes and $h_{ic} \rightarrow \infty$: in this case the interface boundary condition is that of temperature continuity, that is $T_1 = T_2$.

T_1 was calculated using Eq. (3.12) with the heat flow rate and inside and outer diameters of the stainless steel pipe. Inside temperature of the pipe was taken as vapor temperature. T_2 was calculated using the same equation with known heat flow rate, measured diameter of the solid tin shell, and outer

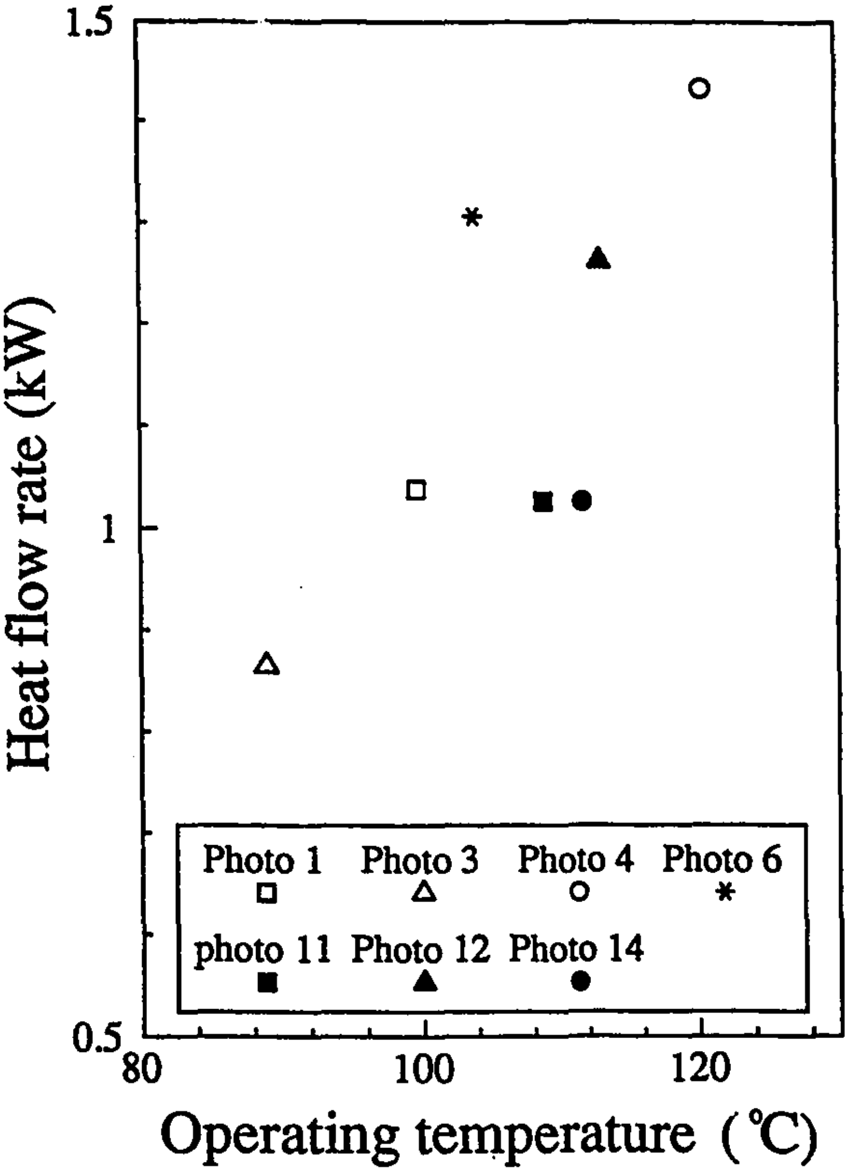

Figure 3.20: Effect of operating temperature on heat flow rate (Water flow rate = 1.2 l/min).

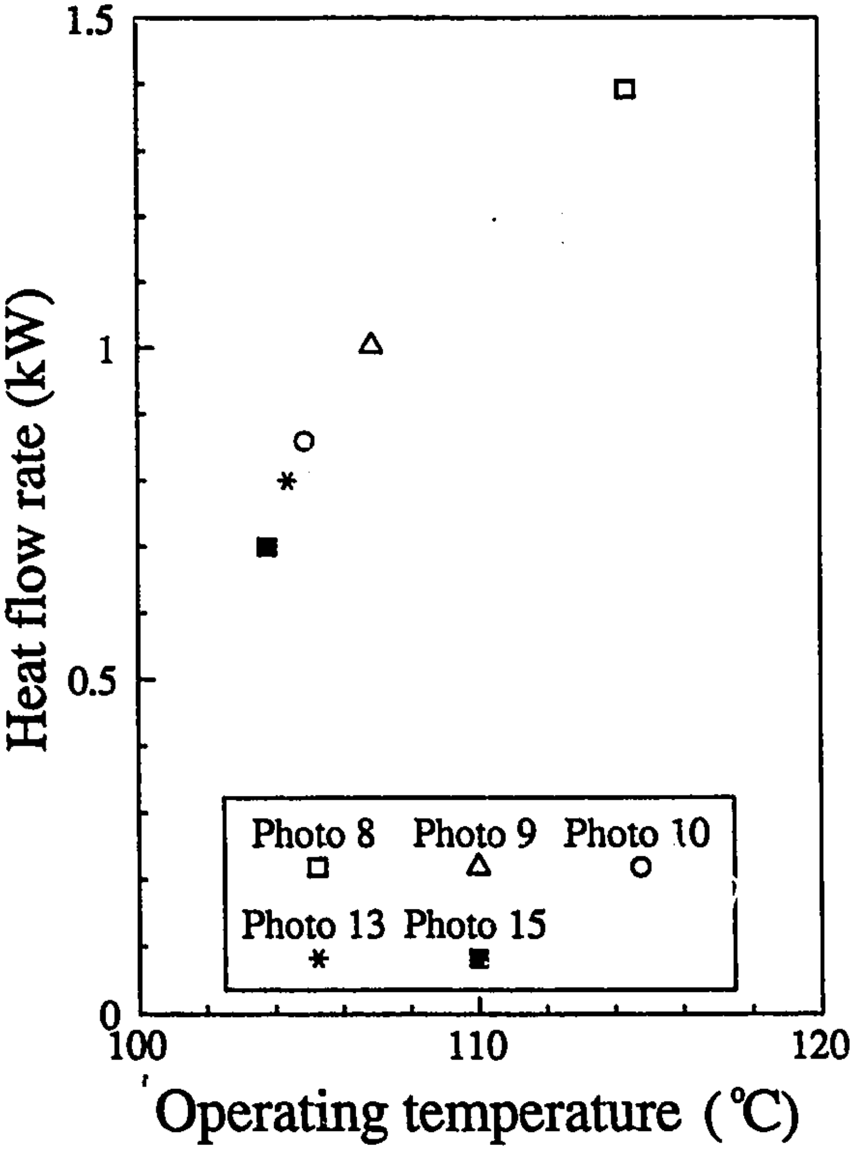

Figure 3.21: Effect of operating temperature on heat flow rate (Water flow rate = 1.9 l/min).

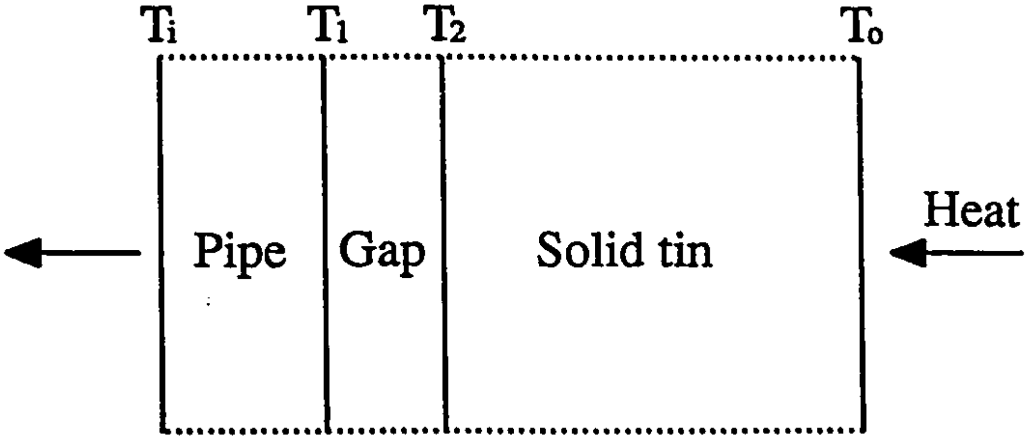

Figure 3.22: Schematic of interfacial contact.

diameter of the pipe. Outer temperature of the tin solid shell was taken as the solidification temperature of the tin.

Calculated interfacial thermal conductance was tabulated using Eq. (3.13) from known heat flow rate and calculated T_1 and T_2. As shown in Table 3.6, the temperature of the thermocouple on the heat pipe ranges between T_1 and T_2. When the thermocouple reading was close to T_2, the calculated ratio of radii was close to experimental value. In these instances, the interfacial conductance shows a high value. For these cases the temperature differences between T_1 and T_2 were smaller than for the cases that yielded little solid tin on the heat pipe. When the thermocouple reading was close to T_1, the interfacial contact resistance was high and showed lower interfacial conductance values.

Calculations of heat transfer coefficient

To understand the heat transfer characteristics of the heat pipe, film condensation occurring in the condenser section was studied. Film condensation problem was first investigated by Nusselt [125] with following assumptions:

1. The plate is maintained at a uniform temperature that is less than the saturation temperature of the vapor.
2. The downward flow is laminar.
3. Fluid properties are constant.
4. Heat transfer across the condensate layer is by pure conduction, hence the liquid temperature distribution is linear.

Table 3.6: Calculations of interfacial thermal contact conductance and radius ratio.

Exp. #	T_v °C	T_1 °C	T_2 °C	h_{ic} W/m^2 °C
1	99.6	133.8	223.9	2403.6
2	87.3	111.2	200.6	1682.1
3	89.0	117.5	224.0	1693.2
4	120.5	153.2	171.7	16135.7
6	103.9	133.7	223.4	3039.1
8	114.4	146.5	171.6	11709.4
9	106.9	130.1	213.7	2529.1
10	104.9	133.5	220.5	2082.5
11	108.8	142.6	224.0	2629.4
12	113.1	154.7	183.1	9264.5
13	104.4	131.2	226.5	1778.9
14	111.7	145.5	163.3	11995.7
15	103.8	127.0	224.2	1507.2

Exp. #	Heat flow rate W	Wall temperature °C	r_2/r_1 Experimental	r_2/r_1 Calculated
1	1029.4	154.0	1.2	5.1
2	715.7	120.9	2.5	28.1
3	857.8	126.7	1.2	14.0
4	1421.3	170.4	3.7	3.8
6	1295.9	153.2	1.2	6.6
8	1395.9	170.8	3.8	3.9
9	1006.3	160.6	1.7	9.0
10	861.4	157.3	1.3	6.4
11	1017.9	168.1	1.2	3.9
12	1251.7	169.9	2.3	2.9
13	806.9	145.0	1.2	10.1
14	1017.9	155.9	4.2	5.0
15	697.5	146.6	1.3	13.9

Because the liquid film thickness is much smaller than the tube radius, analysis for the vertical plate can be used. Following Nusselt theory, the local heat transfer coefficient for the vertical wall can be expressed as[126]

$$h_c = \left(\frac{\rho_l g k_l^3}{3\mu_l Q_f}\right)^{1/3} \tag{3.14}$$

where Q_f is volumetric flow rate per unit perimeter($Q_f = u\delta$). The condensation heat transfer coefficient is calculated using

$$h_c = (\dot{Q}/A_c)/(T_v - T_c) \tag{3.15}$$

where A_c is area of the cooling zone,

T_v is vapor temperature and is chosen as the wall temperature of the thermocouple 47 cm away from the bottom,

T_c is mean temperature of inner surface area that was calculated using Eq. (3.12) with known $\dot{Q}$ value and mean outer temperature,

$\dot{Q}$ is heat flow rate.

It is worth noting that the vapor temperature was assumed uniform in the condenser. Inaccuracy on the calculation of the heat transfer coefficient may increase if there are axial gradients through the wall and vapor segments. However this effect would be insignificant because the temperature difference across the film is of the order of 10 °C and the axial temperature change is of the order of 1 °C. Film Reynolds numbers defined by Eq. (3.16) are shown in Table 3.7.

$$Re = \frac{u\delta}{\nu} = \frac{\dot{Q}}{\pi\, d_i\, \Delta H_v\, \mu_l} \tag{3.16}$$

Film Nusselt number can be introduced as [106, 127]

$$Nu = \frac{h_c}{k}\left(\frac{\nu_l^2}{g}\right)^{1/3} \tag{3.17}$$

After incorporating Eq. (3.14) and (3.16) into Eq. (3.17), condensation heat transfer over a vertical wall can be written as

$$Nu = 1/(3Re)^{1/3} \tag{3.18}$$

Some variables necessary to calculate film Reynolds and Nusselt numbers are found in Table 3.7.

The theoretical Nusselt solution is plotted with experimental data in Figure 3.23. As shown in the figure, the experimental data are quite scattered and lower than Nusselt's solution. There are several factors that cause low values for the heat transfer coefficient at the top of the device.

If any non-condensable gases are present, they will move upward and accumulate at the top of the condenser. Thus the non-condensable gas blocks active condenser area. Furthermore the gas front will spread toward the bottom of the condenser and thus cause a diffusive resistance to vapor moving to the interface that reduces condensation.

Table 3.7: Calculations of heat transfer coefficients for condensation.

Exp. #	Heat flow rate W	T_v °C	T_c °C	h_c W/m^2 °C
1	1029	99.6	75.7	6100.7
2	716	87.3	71.7	6514.0
3	858	89.0	63.5	4783.1
4	1421	120.5	80.1	5003.8
6	1296	103.9	76.5	6738.6
8	1396	114.4	60.5	3680.2
9	1006	106.9	47.3	2400.6
10	861	104.9	43.1	1982.7
11	1018	108.8	57.0	2797.0
12	1252	113.1	61.2	3433.9
13	807	104.4	39.0	1755.5
14	1018	111.7	57.8	2683.9
15	698	103.8	36.4	1473.2

Exp. #	Re	Nu Experimental	Nu Calculated	Nu_{cal}/Nu_{exp}
1	23.28	0.18	0.24	1.3
2	16.20	0.20	0.27	1.3
3	19.41	0.14	0.26	1.7
4	32.15	0.15	0.22	1.4
6	29.32	0.20	0.22	1.1
8	31.59	0.11	0.22	1.9
9	22.76	0.07	0.24	3.3
10	19.48	0.06	0.26	4.3
11	23.03	0.08	0.24	2.8
12	28.33	0.10	0.23	2.1
13	18.26	0.05	0.26	4.9
14	23.03	0.08	0.24	3.0
15	15.79	0.04	0.28	6.2

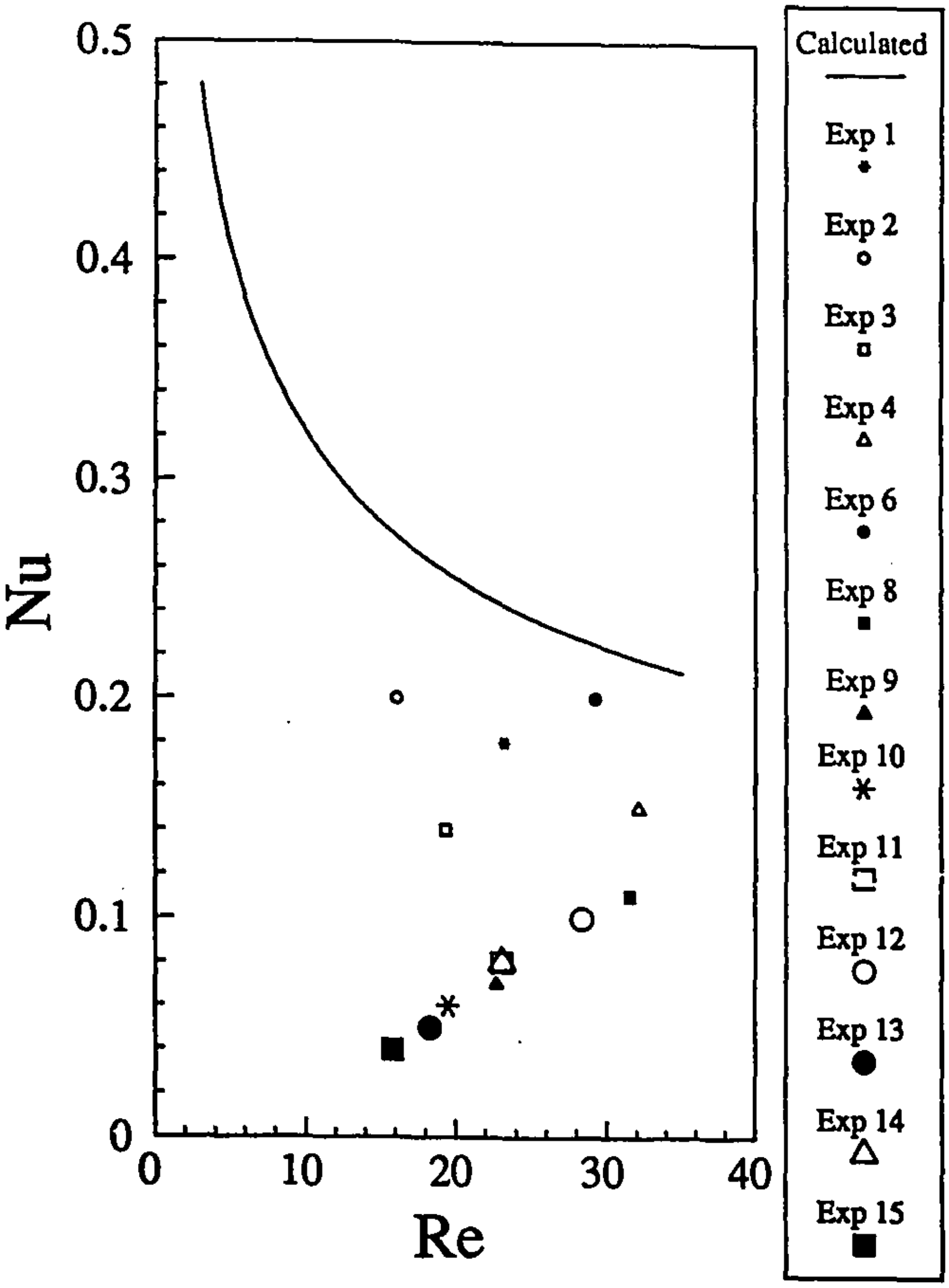

Figure 3.23: Nu number vs. Re number.

Another possible explanation is that there may be no liquid film at the top of the condenser. For some test runs, heat transfer was very small. The wall temperature was observed to be close to the cooling water temperature. In the experimental setup, two thermocouples were located in the cooling chamber exposed to the cooling water at 53 and 57 cm away from the bottom of the pipe. When the temperature of the thermocouple located in the upper zone (57 cm away from the bottom) was lower than that located in the lower zone (53 cm away from the bottom) heat transfer was very low. In those cases, the inside wall temperature was relatively low. This indicates that little condensation was occurring in this region of the device and a liquid film may have not existed.

Heat flow rate vs. pressure

A physical model based on a stability analysis at the liquid-vapor interface was developed by Prenger[128] to predict the performance limit of the gravity-assisted heat pipe. The model developed by Prenger is explained next. The interface between the counterflowing vapor and liquid is distorted due to local disturbances in the flow. Centrifugal forces are produced in both the vapor and liquid which produce a pressure component normal to the interface as described in Figure 3.24. These pressure forces are counteracted by the surface tension of the interface. The centrifugal force is described as

$$\frac{\partial P}{\partial n} = -\frac{\rho U^2}{R} \tag{3.19}$$

where R is the radius of the curvature of the interface and n is the normal to the interface. The wavelength(Γ) of the disturbance is large compared to the thickness of the film(δ). Thus the wave length of the disturbance and the radius of the curvature along the flow axis are written as

$$\Gamma = \pi D \qquad\qquad R = \Gamma^2/\delta \tag{3.20}$$

The centrifugal forces in the vapor can be expressed as

$$\frac{\Delta P_g}{D/2} = \frac{\rho_g U_g^2}{R} \tag{3.21}$$

Eqs. (3.20) and (3.21) can be combined and rewritten as

$$\Delta P_g = \frac{1}{2\pi}\frac{\delta}{\Gamma}\rho_g U_g^2 \tag{3.22}$$

The centrifugal force for the liquid is

$$\frac{\Delta P_f}{\delta} = \frac{\rho_f U_f^2}{R} \tag{3.23}$$

or using Eq. (3.20)

$$\Delta P_f = \left(\frac{\delta}{\Gamma}\right)^2 \rho_f U_f^2 \tag{3.24}$$

The pressure forces at the interface are balanced by the surface tension at the interface ($\Delta P_\sigma = \sigma/R$), thus

$$-\Delta P_g - \Delta P_f + \Delta P_\sigma = 0 \tag{3.25}$$

By incorporating Eqs. (3.22) and (3.24) this becomes

$$\frac{2\pi\delta}{\Gamma}\rho_f U_f^2 + \rho_g U_g^2 = \frac{2\pi\sigma}{\Gamma} \tag{3.26}$$

This equation is almost identical to a result obtained by Hewitt and Hall-Taylor[126]. When the inside surface of the heat pipe is smooth, the vapor inertia is large compared to the liquid inertia. It is assumed that liquid is distributed uniformly around the internal surface and is therefore thin. Under these conditions neglecting the liquid inertia Eq. (3.26) becomes

$$\rho_g U_g^2 = \frac{2\pi\sigma}{\Gamma} \tag{3.27}$$

The above equation can be written in dimensionless form using a dimensionless heat flux and an entrainment parameter[129] defined respectively as

$$Q_e = \frac{q}{\rho_g A_v h_{fg}^{1.5}} \tag{3.28}$$

and

$$E_t = \frac{\sigma}{\rho_g h_{fg} \Gamma} \tag{3.29}$$

where Γ is a characteristic dimension describing the liquid film which Kutateladze [130] showed, based on a hanging film model, that

$$\Gamma = \left[\frac{\sigma}{(\rho_f - \rho_g)g}\right]^{1/2} \tag{3.30}$$

Using Eqs. (3.28) and (3.29), Prenger derived Eq. (3.31) from Eq. (3.27).

$$Q_e = \sqrt{2\pi} E_t^{1/2} \tag{3.31}$$

From this equation, heat flow rate is proportional to the $\sqrt{\rho_g}$ by neglecting the change of density of the gas in the Γ and can be written as

$$q \propto \sqrt{\rho_g} \tag{3.32}$$

A similar expression has been obtained for heat pipes when considering only capillary limitations[131].

For the present study, it was assumed that the vapor was saturated and that the classical Clausius-Clapeyron relationship between saturation pressure and temperature applies. Thus, Eq. (3.32) has been rewritten as

$$q = \sqrt{C_1 p_v + C_2 p_v \, ln \, p_v + C_3} \tag{3.33}$$

where p_v is the vapor pressure in the heat pipe. This equation has been derived in an effort to allow for the prediction of the heat flow rate from the pressure transducer readings. Changes of heat flow rate with respect to the internal pressure are shown in Figures 3.25 to 3.29. Regression curves for the different experiments are shown in Figure 3.30. Coefficients of Eq. (3.33) for different experiments are shown in Table 3.8.

As can be seen in Figure 3.30, the experiments can be divided into two groups such as from experiments 1 to 6 and 8 to 15. This difference seems caused by the difference in the cooling water temperature as shown in Table 3.5. In the case of experiments 1 to 6, cooling water temperatures were higher than those of the other case which results in higher condenser wall temperature, and therefore a smaller temperature difference between the vapor and the condenser wall. Heat transfer coefficient of the cooling section decreases with increasing temperature difference between the vapor and condenser wall[108]. However the heat flow rate is proportional to the product of the heat transfer coefficient and the temperature difference. It seems that the decrease of the heat transfer coefficient has a dominating effect over the increase of the temperature difference. Another possible explanation is that due to the higher pressure in experiments 8 to 15 which in turn implies higher vapor velocity, entrained droplets may cause the lower heat transfer coefficients.

The difference in experimental conditions between experiments 1 to 3 and 4 to 6 is the immersion depth (Table 3.4). Immersion depth for experiments 4 and 6 is higher than that for experiments 1 to 3 and as a consequence the heat pipe transports more energy and operates at higher pressure. The same explanation can be applied to explain the difference between experiments 8 and 9 and the subsequent group of experiments 10 to 15. Eq. (3.33) can be used to predict the heat flow rate from the pressure readings for a specific operating condition(e.g. constant depth and cooling water temperature).

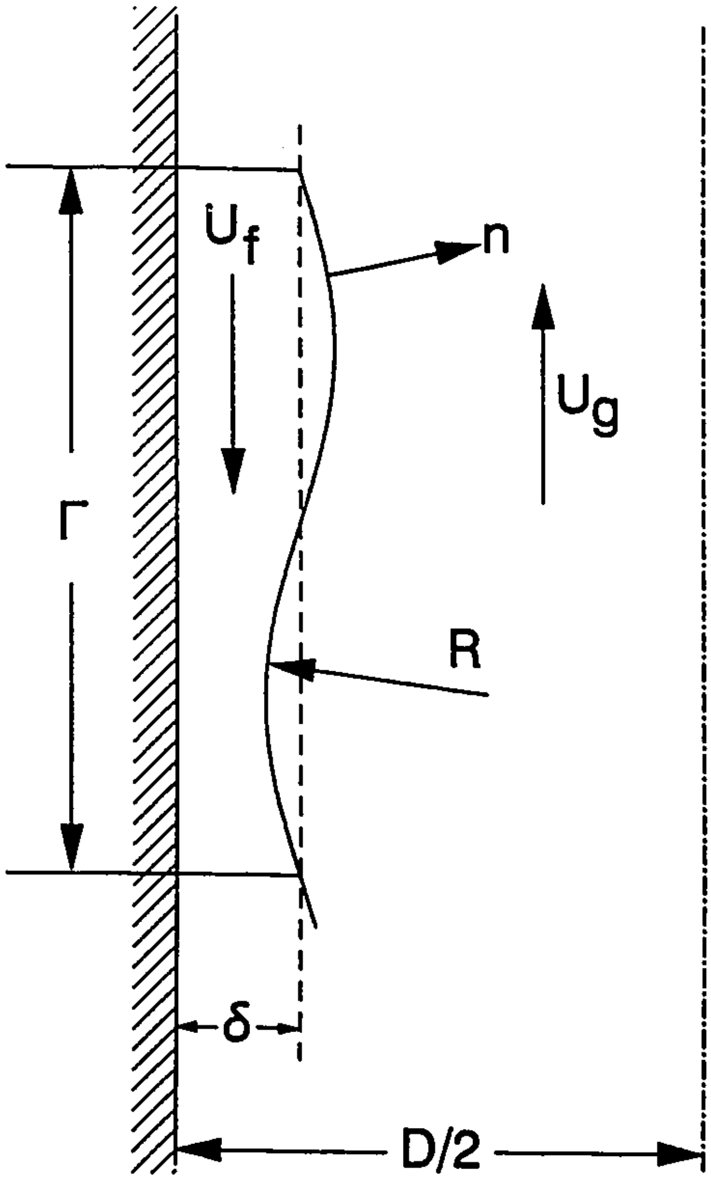

Figure 3.24: Geometry of the liquid-vapor interface.

Table 3.8: Coefficients of the regression for the experiments.

Exp. #	C_1	C_2	C_3
Exp. 1,2,3	3.6046	-3.5240	-2.3072
Exp. 4,6	4.2789	-2.6975	-2.3739
Exp. 8,9	3.6963	-0.8404	-3.1115
Exp. 10 to 15	1.5032	0.5325	-1.0502

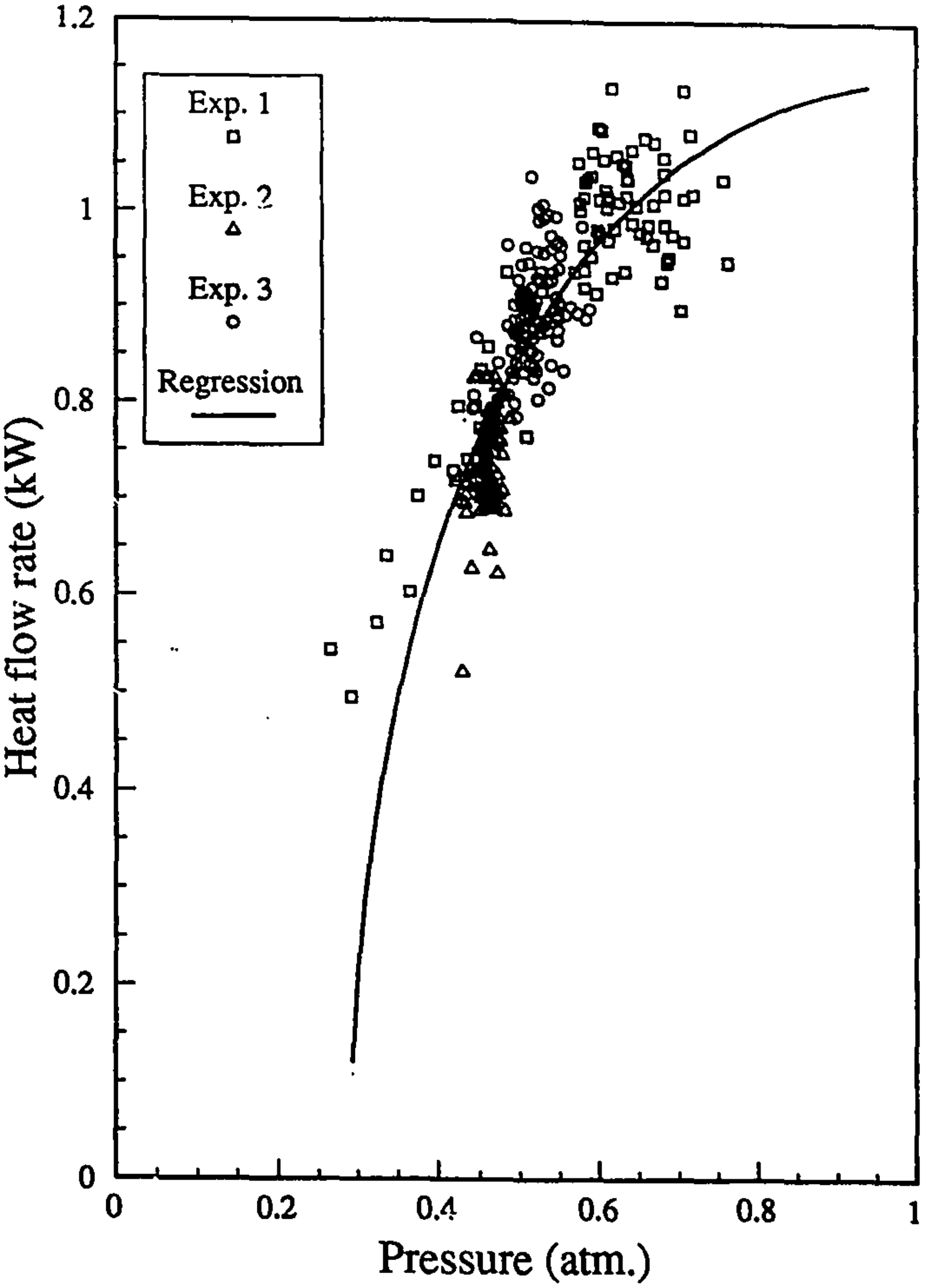

Figure 3.25: Heat flow rate vs. pressure for Exp. 1, 2, and 3.

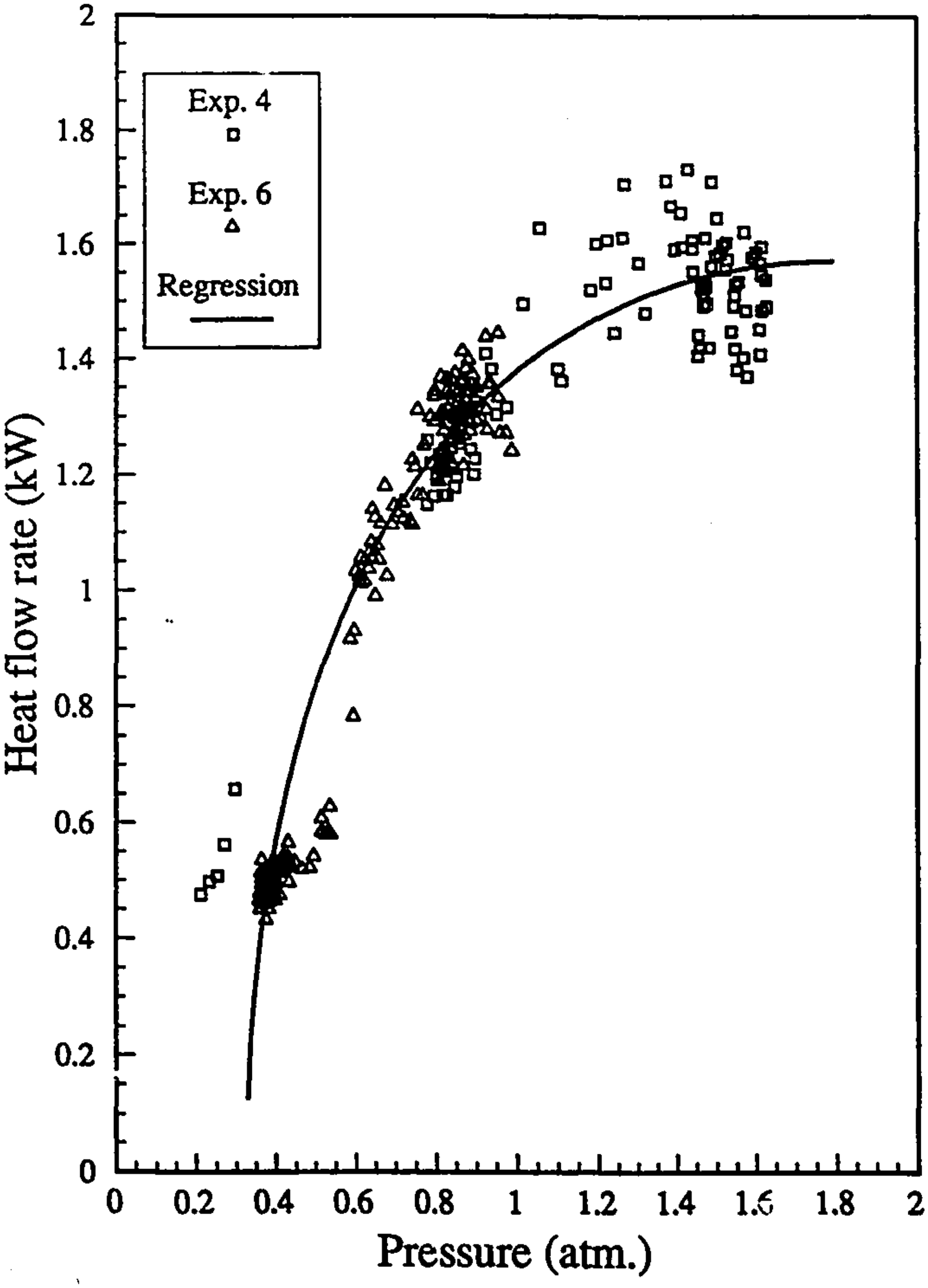

Figure 3.26: Heat flow rate vs. pressure for Exp. 4 and 6.

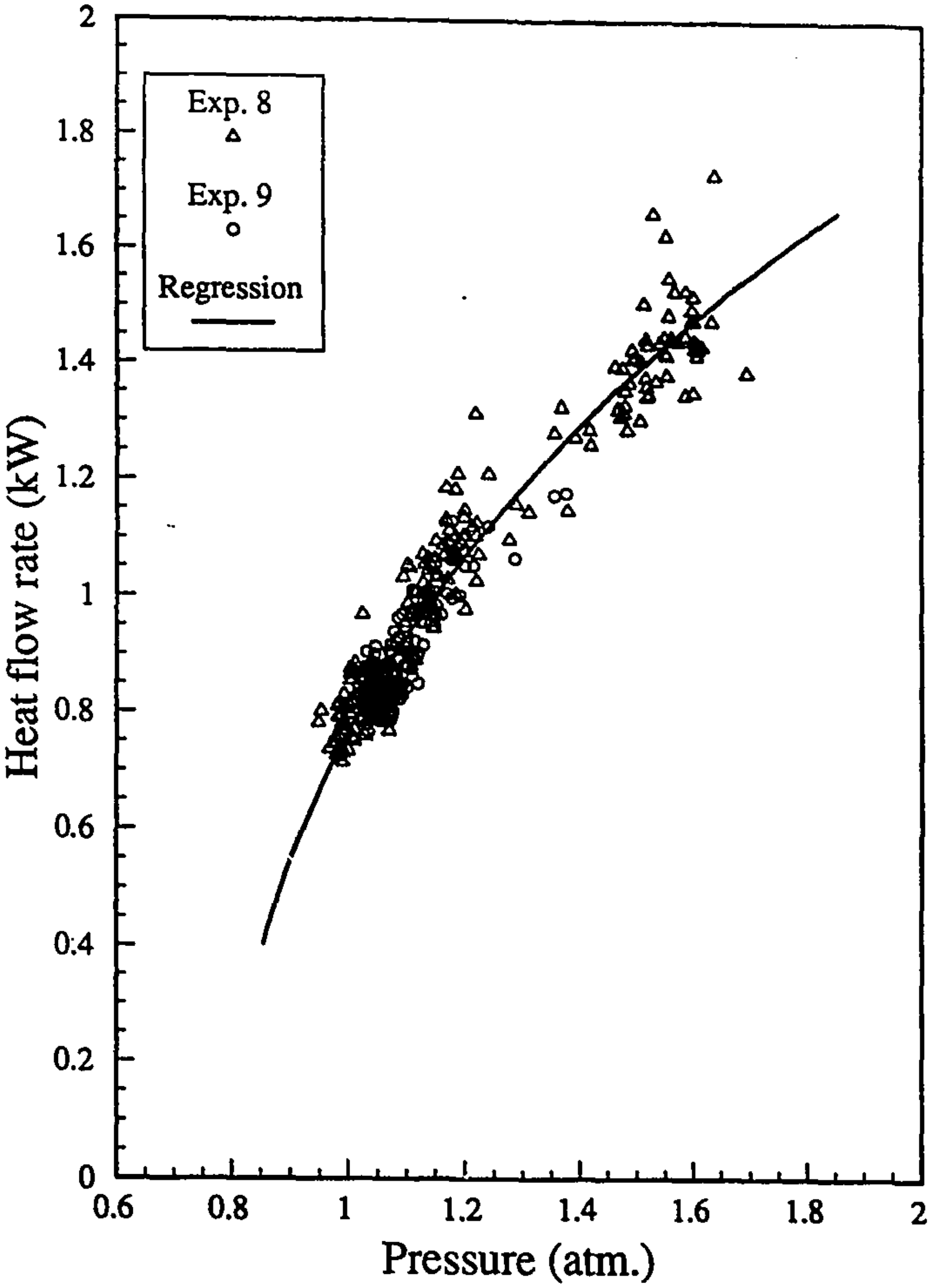

Figure 3.27: Heat flow rate vs. pressure for Exp. 8 and 9.

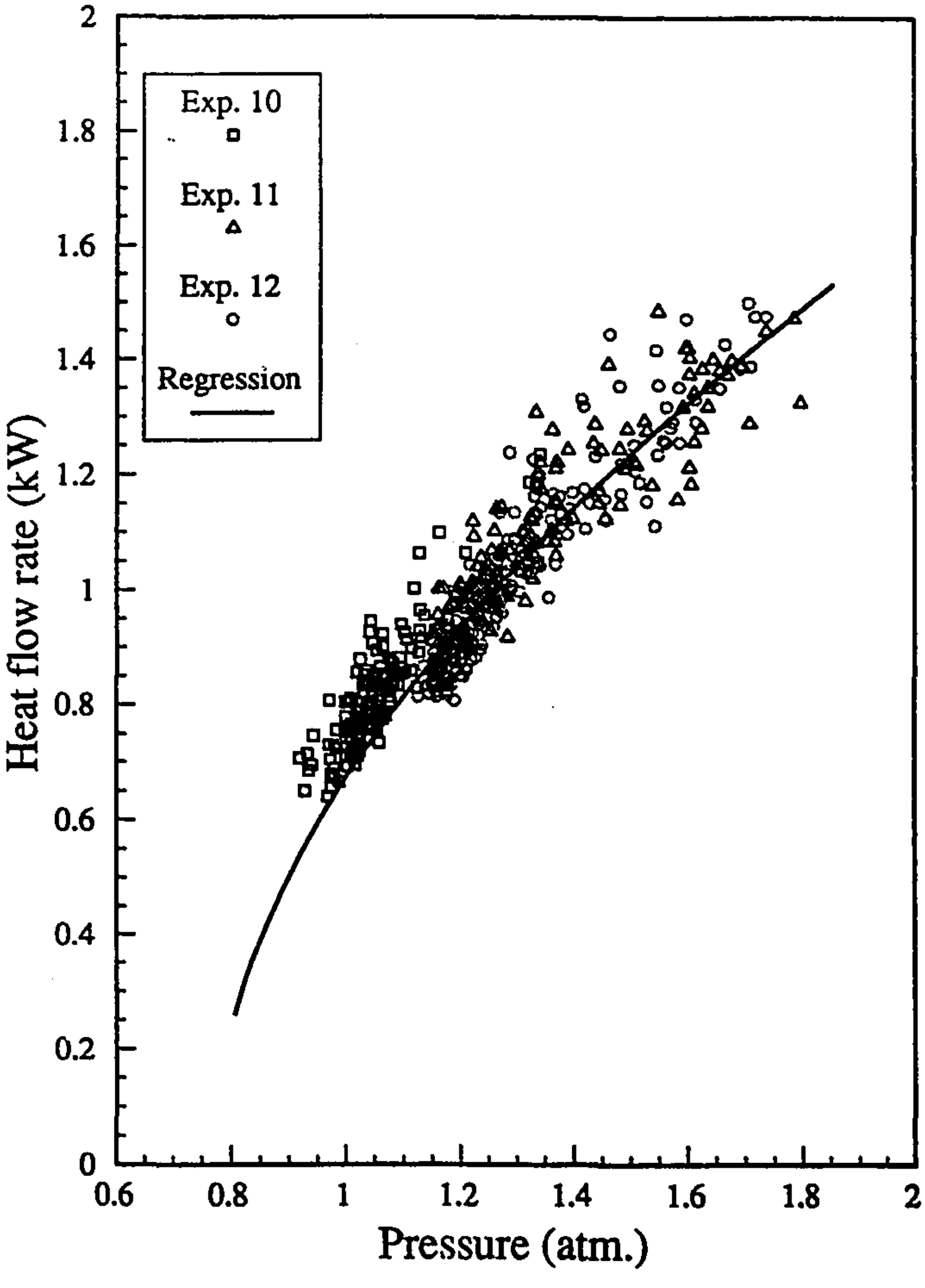

Figure 3.28: Heat flow rate vs. pressure for Exp. 10, 11, and 12.

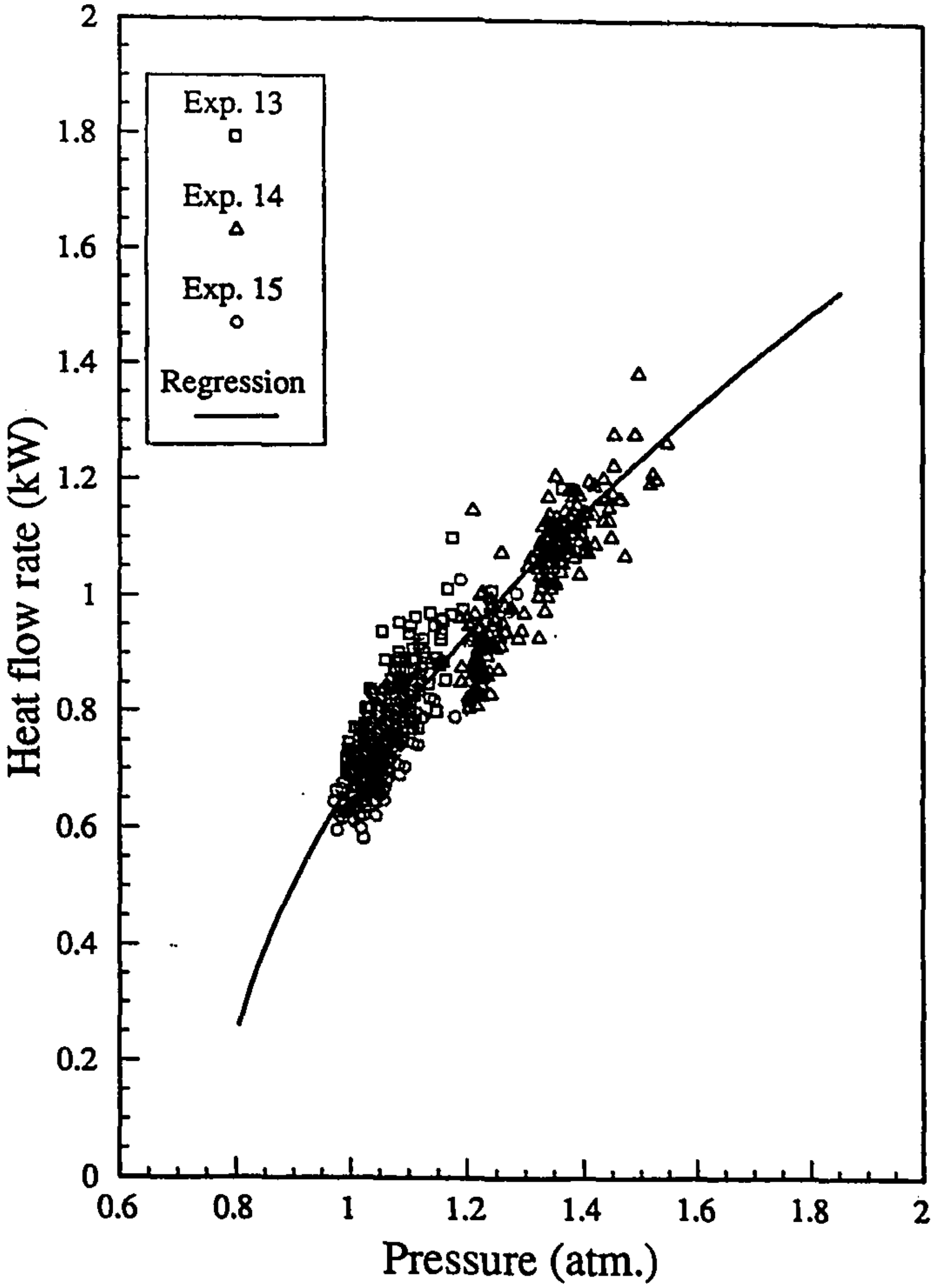

Figure 3.29: Heat flow rate vs. pressure for Exp. 13, 14, and 15.

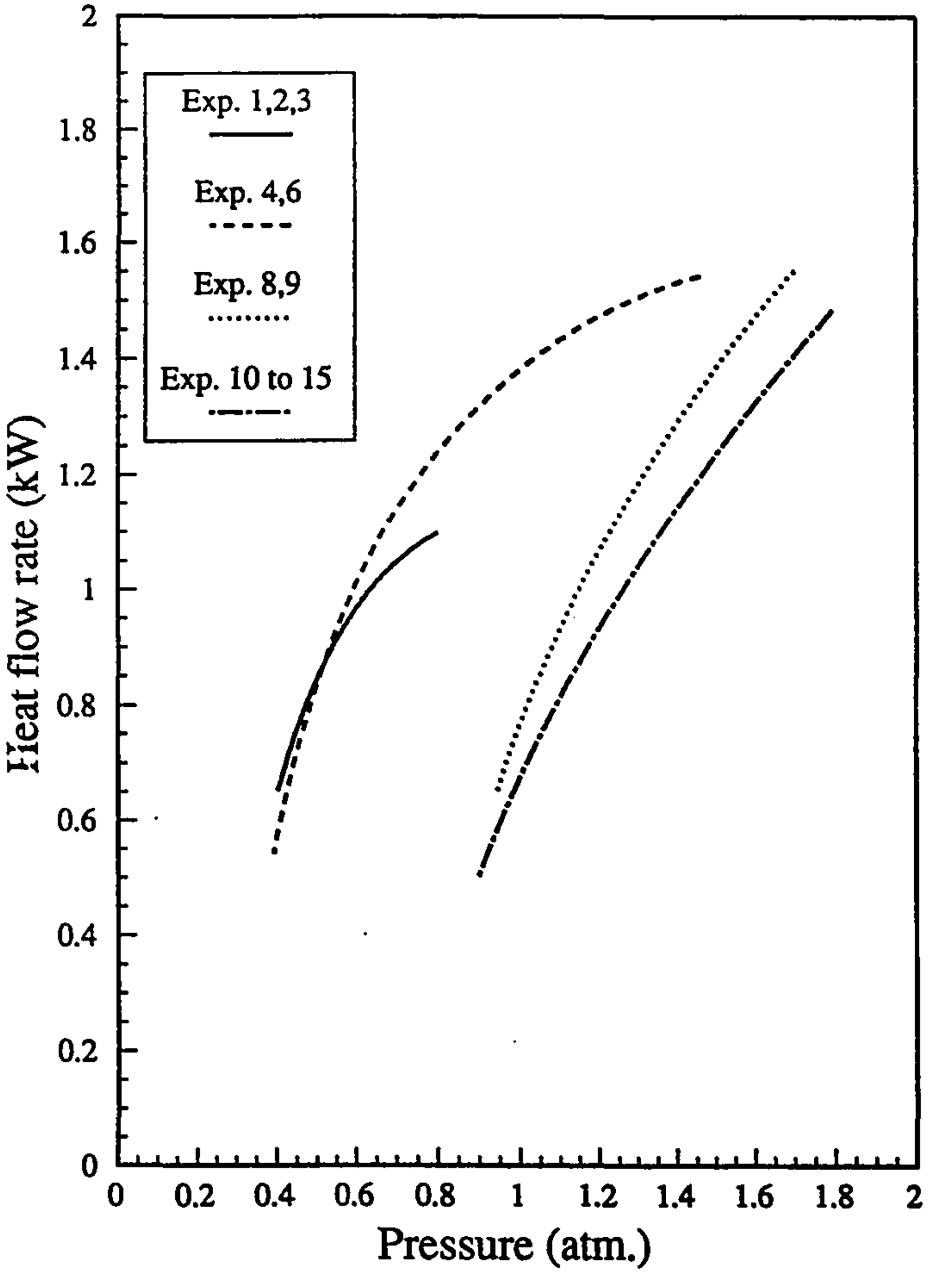

Figure 3.30: Regression curves for heat flow rate vs. pressure for Exp. 1 to 15.

3.3.2 Sodium Heat Pipe

In addition to the low temperature heat pipe using water as the working fluid, a high temperature heat pipe employing sodium as the working fluid was also constructed and tested. Figure 3.31 shows the testing of the heat pipe where the bottom part of the pipe was heated by induction furnace and the corresponding temperature variation of the thermocouples located outside the heat pipe at different levels. After the power of the furnace was turned on, the thermocouple reading closest to the bottom increased sharply due to the vaporization of the sodium. As the heat input was raised, the amount of the sodium vaporized increased and moved upward. Thus, the temperature at a higher location also increased sharply when the sodium vapor reached the level of the corresponding thermocouple. As more sodium vaporized, the inside pressure increased. The temperature that was obtained from the pressure values was quite similar to that of the thermocouple reading located 10 cm away from the bottom. After the power of the induction furnace was turned off some inert gas inside the pipe was observed from the reading of the pressure transducer. Thus after the heat pipe was cooled down it was connected to the vacuum pump and the retained inert gas was evacuated.

Next the heat pipe was tested in a bath of molten matte with the induction furnace. Before immersing the heat pipe into the molten matte, a section of stainless steel pipe was immersed into the molten matte for five minutes to evaluate its ability to withstand the matte. During the five minutes the pipe was dissolved into the molten matte and the diameter was reduced from 1.375 cm to 1.36 cm.

Figure 3.32 shows the top view of the heat pipe in operation. In this

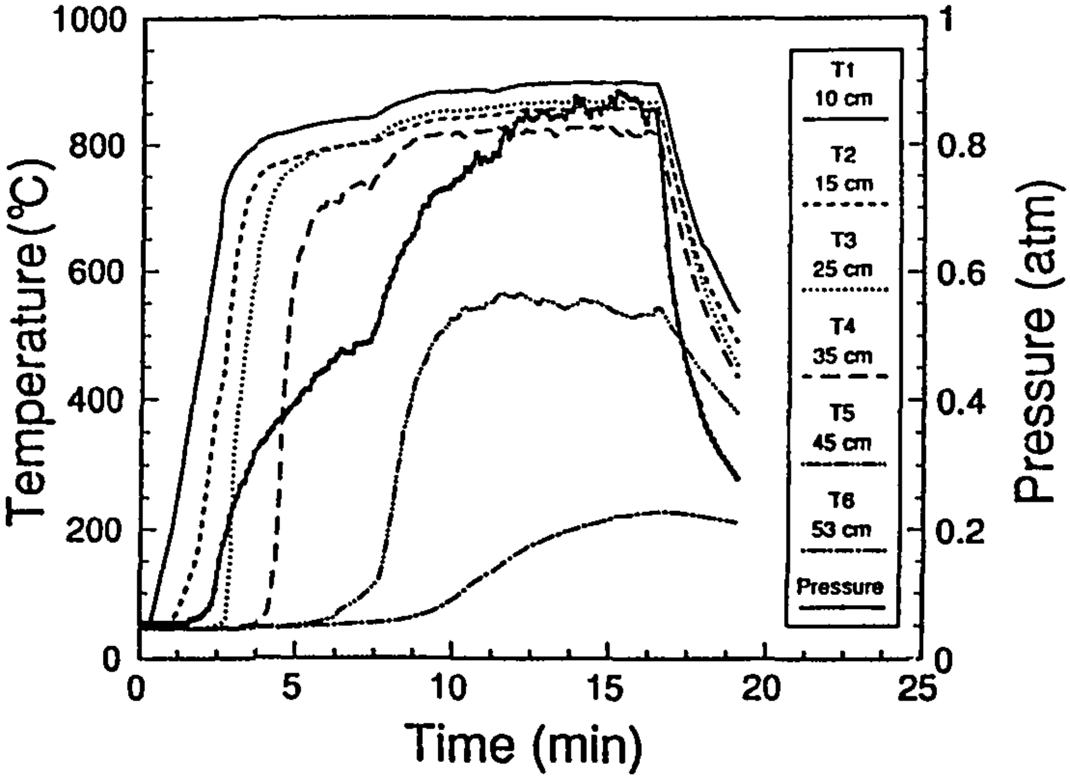

Figure 3.31: Testing of the heat pipe with induction furnace and the corresponding temperature variation of the thermocouples.

instance 3.5 cm of the pipe was dipped into the copper matte while the matte temperature was 1150 °C. From the top, a thin dark ring around the heat pipe was observed during heat pipe operation. This was found to be solid matte that was acting as protective layer over the pipe and prevented dissolution. Figure 3.33 shows the solid shell of matte after being immersed approximately 15 minutes. Corresponding pipe diameters after shell formation are shown in Table 3.9. For example, the diameter of the pipe with the shell was 2.88 cm when 3.5 cm of pipe was immersed. This translates to approximately 0.1 cm of solid shell on the heat pipe for this operating condition.

Table 3.9: Pipe diameter after shell formation.

Experimental condition	Diameter *cm*
Outer pipe diameter	2.67
3.5 cm immersed	2.88
7.0 cm immersed	2.8

Figure 3.34 shows the temperature variation of the thermocouples. First peak shows the case when 3.5 cm of the pipe was immersed. Inside pressure was about 0.3 atmosphere which corresponds to the vapor pressure of sodium at 765 °C. Figure 3.35 shows the solid shell when 7.0 cm of the pipe was immersed. The diameter with the solid shell was 2.8 cm. In this case a thin-

ner solid shell was formed than in the previous case. The second peak in Figure 3.34 shows temperature variation for this case. Since it was receiving more heat from the matte, the heat pipe was operating at a higher temperature. The temperature up to 30 cm from the bottom shows very uniform temperature. Inside pressure of the pipe was about 0.67 atmosphere and the corresponding vapor temperature was 840 °C. In both cases the heat pipe was working well even under very corrosive conditions.

The heat flow rate of the sodium heat pipe operating in the copper matte was estimated. Heat transport from the heat pipe to ambient air was considered to be predominantly by radiation, thus, natural convection effects were neglected. Heat flow by the radiation can be written as

$$q = AF\sigma\varepsilon(T_s^4 - T_a^4) \tag{3.34}$$

q = heat flow rate
A = area
F = view factor ($\simeq 1$)
σ = Stefan-Boltzman constant ($5.670 \times 10^{-8}\ W/m^2 \cdot K^4$)
ε = emissivity
T_s = heat pipe surface temperature
T_a = ambient temperature

For the emissivity of the surface, a value of 0.7 was chosen and as such was taken as a highly oxidized stainless steel surface[132]. Estimated heat flow rates are shown in Table 3.10. Estimated values are 2288 and 1344 W when the heat pipe was immersed 7.0 and 3.5 cm respectively.

Table 3.10: Estimation of heat flow rates.

Immersion depth *cm*	Length of hot surface *cm*	Surface temperature °C	Heat flow rate *W*
7.0	45	840	2288
3.5	35	765	1344

Figure 3.32: Top view of the heat pipe in operation.

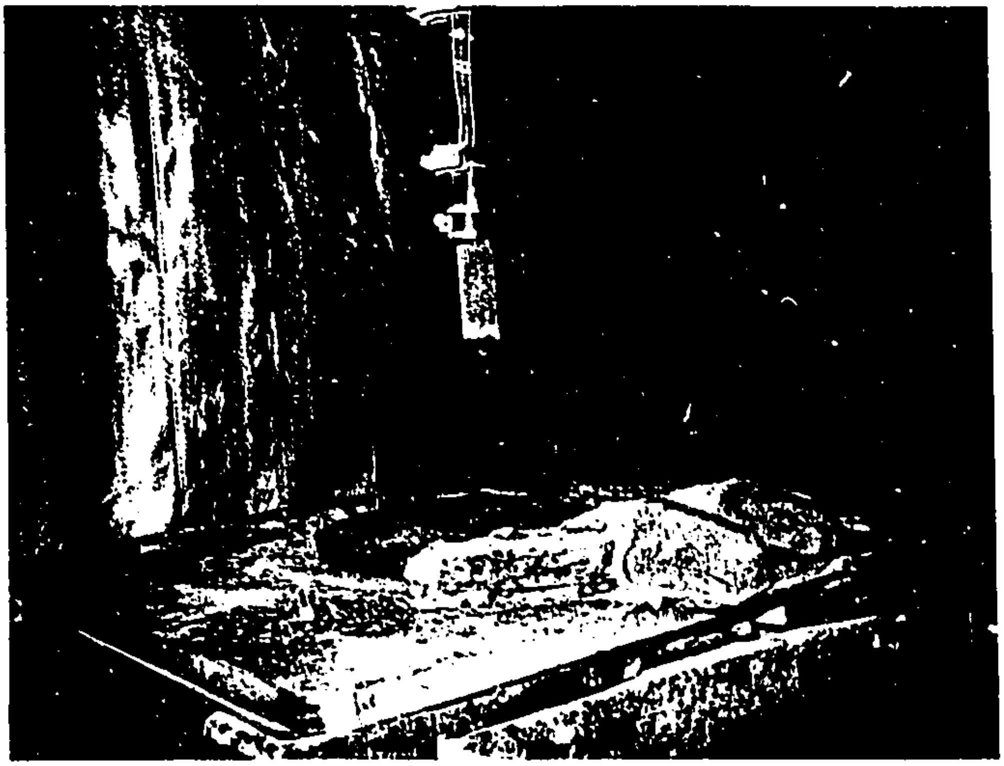

Figure 3.33: Solid shell formation onto the heat pipe (immersion depth = 3.5 cm).

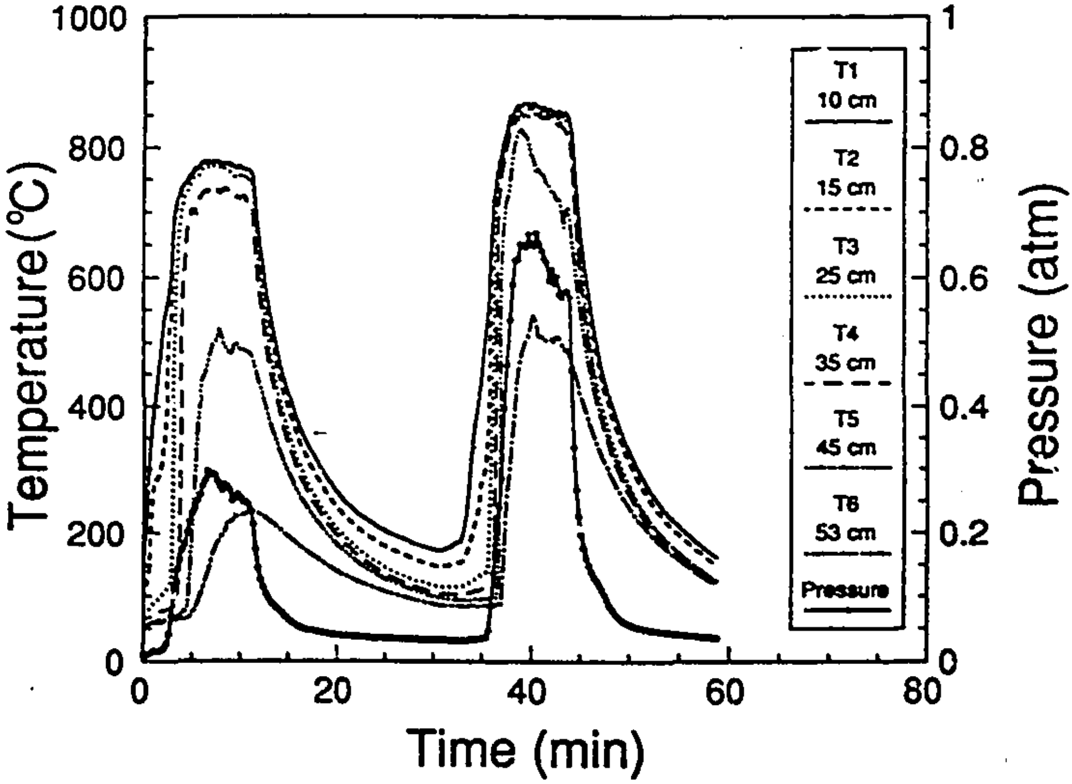

Figure 3.34: Temperature variations of the thermocouples located on the heat pipe.

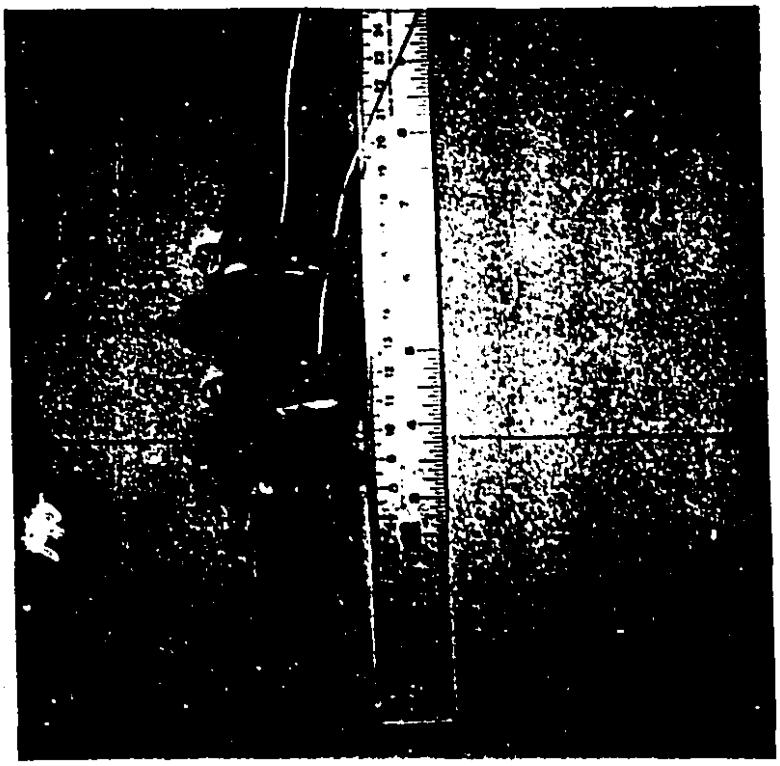

Figure 3.35: Solid shell formation onto the heat pipe (immersion depth = 7.0 cm).

Chapter 4

Conclusions

4.1 Inverse Heat Conduction Approach

Two mathematical models (1-D and 2-D) that track melt temperature have been developed. Both models use the readings from two embedded thermocouples to deduce bath temperature.

The 1-D model is used when the test piece is incorporated into the wall of a vessel. As the time step increases, the amplitude of the oscillation in the calculated values decreases and the error between calculated and measured temperature decreases even though the degree of resolution in the analysis is reduced. A time increment of appropriate length yields a suitable compromise between oscillation(i.e. variability) and resolution. To find a more appropriate form of the heat transfer coefficient, the effect of natural convection was taken into account. Heat flux was expressed as $q_{in} = h'(\theta'_b - \theta'_n)^{1+n}$. When the exponent($n$) was set to 0.08 and 0.25 the model showed good agreement between calculated and measured values for the vertical and horizontal test pieces respectively. High temperature experiments using an aluminum melt also showed good agreement for the same mathematical model.

Laboratory tests have shown it to be reliable provided the 1-D nature of the system is preserved. When this is not possible or feasible, one can resort to the 2-D model which allows for the use of a floating cylindrical probe. Laboratory tests of such a probe in an aluminum melt have confirmed the 2-D model.

4.2 Self-Cooling Sleeve

A low temperature heat pipe employing water as the working fluid and copper as pipe material was tested in a bath of molten tin. Solid tin crust was formed on outer surface of the heat pipe. A simple analysis to estimate the thickness of the solid tin shell was done assuming one dimensional heat conduction through the solid tin. Calculated ratios of the radii were smaller than experimental values.

Another low temperature heat pipe with water as working fluid and stainless steel as pipe material was built and tested. A series of experiments were performed in which the heat pipe was transporting energy at a rate of from 700 to 1400 W. The calculated solid tin shells were in general larger than those measured experimentally. Formations of thinner shells were considered to be a result of the contact resistance. When the value of the interfacial conductance was high, the thickness of the tin shell was comparable to the computed value.

Film behaviour during condensation has been examined. The experimental results were reduced in dimensionless form and compared to Nusselt's solution. It was found that heat transfer coefficients are less than the Nusselt predictions. Possible factors were discussed to explain such trends.

Sodium heat pipe was built and tested in a bath of molten copper matte. Solid copper matte, protective layers of 0.1 and 0.07 cm in thickness were formed on the heat pipe when immersion depths were 3.5 and 7.0 cm respectively. Without any form of cooling, stainless steel was dissolving relatively quickly in the molten matte and the diameter was reduced from 1.375 to 1.36 cm in five minutes. Thus a heat pipe self cooling sleeve is suitable protection for an immersion thermocouple, however, one would need to select the pipe and working substance with care to ensure compatibility with the melt. Nonetheless, it has been shown that self cooling sleeves are indeed viable.

Appendix

A Thermal Properties of Sodium

The properties of sodium in the vapor state are expressed in terms of temperatures, which are in degrees Kelvin in the following property equations:

Saturation vapor pressure[133]:

$$P = 2.29 \times 10^{11} \times \frac{1}{T^{0.5}} \times 10^{\frac{-5567}{T}} \qquad [N/m^2]$$

Density of sodium vapor[133]:

$$\rho = 6.335 \times 10^{8} \times \frac{1}{T^{1.5}} \times 10^{\frac{-5567}{T}} \qquad [kg/m^3]$$

Viscosity of sodium vapor[134]:

$$\mu = 6.083 \times 10^{-9} \times T + 1.2606 \times 10^{-5} \qquad [N-s/m^2]$$

Enthalpy of sodium vapor[133]:

$$h_f = 271831 - 1595.3 \times T - 0.29024 \times T^2 + 2.4 \times 10^6 \times exp\frac{-13600}{T} \qquad [J/kg]$$

$$h_{fg} = 4636437.26 - 180.817 \times T \qquad [J/kg]$$

Thermal properties of sodium in the solid and liquid state[135, 136] are tabulated as follows:

Thermal properties of solid sodium[135].

Density		**Specific heat**		**Conductivity**	
Temp. K	Density kg/m^3	Temp. K	Specific heat J/kgK	Temp. K	Conductivity $W/n.K$
273	972.5	273	1200	100	136
283	970.5	298	1223	150	140
293	968.4	323	1256	200	142
303	966.3	348	1308	250	143
313	964.2	371	1364	371	141
323	962.1				
333	959.9				
343	957.7				
353	955.5				
363	953.2				
371	951.4				

Thermal properties of liquid sodium[136].

Density		Specific heat		Conductivity	
Temp. K	Density kg/m^3	Temp. K	Specific heat J/kgK	Temp. K	Conductivity W/mK
373	927	371	1385	473	81.5
473	904	373	1384	573	75.7
573	882	473	1340	673	71.0
673	859	573	1305	773	67.2
773	834	673	1279	873	63.9
873	809	773	1262	973	61.0
973	783	873	1255	1073	58.3
1073	757	973	1255		
		1073	1269		
		1173	1289		

B Thermal Properties of Water

Thermal properties of water[137].

Temp.	Pressure	Density		Heat of vaporization
°C	P_v atm.	ρ_f kg/m^3	ρ_v kg/m^3	h_{fg} kJ/kg
121.1	2.0295	941.84	1.1591	2194.3
120.0	1.9594	942.73	1.1216	2197.5
118.9	1.8915	943.62	1.0851	2200.5
117.8	1.8254	944.51	1.0496	2203.8
116.7	1.7612	945.40	1.0150	2206.8
115.6	1.6990	946.30	0.9814	2209.8
114.4	1.6385	947.19	0.9486	2213.1
113.3	1.5798	948.03	0.9168	2216.1
112.2	1.5228	948.87	0.8858	2219.1
111.1	1.4675	949.77	0.8557	2222.1
110.0	1.4139	950.62	0.8264	2225.1
109.4	1.3877	951.02	0.8121	2226.8
108.9	1.3619	951.47	0.7979	2228.2
108.3	1.3366	951.86	0.7840	2229.8
107.8	1.3115	952.32	0.7703	2231.2
107.2	1.2869	952.71	0.7567	2232.8
106.7	1.2627	953.11	0.7434	2234.2
106.1	1.2388	953.56	0.7303	2235.8
105.6	1.2153	953.96	0.7173	2237.2
105.0	1.1922	954.36	0.7045	2238.8
104.4	1.1694	954.81	0.6919	2240.2
103.9	1.1470	955.21	0.6795	2241.6
103.3	1.1250	955.61	0.6673	2243.2
102.8	1.1033	956.01	0.6553	2244.6
102.2	1.0820	956.41	0.6434	2246.3

101.7	1.0610	956.81	0.6317	2247.7
101.1	1.0404	957.21	0.6202	2249.0
100.6	1.0200	957.61	0.6088	2250.7
100.0	1.0000	958.01	0.5977	2252.1
99.4	0.9803	958.41	0.5867	2253.5
98.9	0.9610	958.81	0.5758	2255.1
98.3	0.9420	959.22	0.5652	2256.5
97.8	0.9232	959.62	0.5546	2257.9
97.2	0.9048	960.02	0.5443	2259.5
96.7	0.8867	960.42	0.5341	2260.9
96.1	0.8689	960.83	0.5240	2262.3
95.6	0.8514	961.17	0.5142	2263.9
95.0	0.8342	961.58	0.5044	2265.3
94.4	0.8173	961.98	0.4949	2266.7
93.9	0.8006	962.39	0.4854	2268.1
93.3	0.7843	962.73	0.4761	2269.7
92.8	0.7682	963.14	0.4670	2271.1
92.2	0.7524	963.49	0.4580	2272.5
91.7	0.7369	963.89	0.4492	2273.9
91.1	0.7216	964.24	0.4405	2275.5
90.6	0.7067	964.65	0.4319	2276.9
90.0	0.6919	965.00	0.4235	2278.3
89.4	0.6775	965.40	0.4152	2279.7
88.9	0.6632	965.75	0.4070	2281.1
88.3	0.6492	966.16	0.3990	2282.7
87.8	0.6355	966.51	0.3911	2284.1
87.2	0.6220	966.86	0.3833	2285.5
86.7	0.6088	967.27	0.3757	2286.9
86.1	0.5958	967.62	0.3681	2288.3
85.6	0.5830	967.97	0.3607	2289.7
85.0	0.5705	968.32	0.3535	2291.1
84.4	0.5582	968.73	0.3463	2292.7
83.9	0.5461	969.08	0.3393	2294.1

83.3	0.5342	969.43	0.3324	2295.5
82.8	0.5225	969.79	0.3256	2296.9
82.2	0.5111	970.14	0.3189	2298.3
81.7	0.4999	970.49	0.3123	2299.6
81.1	0.4888	970.85	0.3059	2301.0
80.6	0.4780	971.20	0.2996	2302.4
80.0	0.4674	971.55	0.2933	2303.8
79.4	0.4570	971.91	0.2872	2305.2
78.9	0.4468	972.26	0.2811	2306.6
78.3	0.4367	972.61	0.2753	2308.0
77.8	0.4269	972.91	0.2694	2309.4
77.2	0.4172	973.26	0.2637	2310.8
76.7	0.4078	973.62	0.2581	2312.2
76.1	0.3985	973.97	0.2526	2313.6
75.6	0.3894	974.27	0.2472	2315.0
75.0	0.3805	974.63	0.2419	2316.4
74.4	0.3717	974.98	0.2367	2317.8
73.9	0.3631	975.28	0.2315	2319.1
73.3	0.3547	975.64	0.2265	2320.5
72.8	0.3464	975.93	0.2215	2321.9
72.2	0.3383	976.29	0.2167	2323.3
71.7	0.3304	976.59	0.2119	2324.7
71.1	0.3226	976.94	0.2072	2326.1
70.6	0.3150	977.24	0.2026	2327.5
70.0	0.3075	977.60	0.1982	2328.9
69.4	0.3002	977.90	0.1937	2330.3
68.9	0.2931	978.20	0.1894	2331.7
68.3	0.2860	978.50	0.1851	2333.1
67.8	0.2792	978.85	0.1809	2334.5
67.2	0.2724	979.15	0.1768	2335.9
66.7	0.2658	979.45	0.1728	2337.2
66.1	0.2593	979.75	0.1689	2338.6
65.6	0.2530	980.05	0.1650	2340.0

65.0	0.2468	980.41	0.1612	2341.2
64.4	0.2408	980.71	0.1575	2342.6
63.9	0.2348	981.01	0.1538	2344.0
63.3	0.2290	981.31	0.1503	2345.4
62.8	0.2233	981.61	0.1468	2346.8
62.2	0.2177	981.92	0.1433	2348.2
61.7	0.2123	982.16	0.1399	2349.5
61.1	0.2069	982.46	0.1366	2350.9
60.6	0.2017	982.76	0.1334	2352.1
60.0	0.1966	983.06	0.1302	2353.5
59.4	0.1916	983.36	0.1271	2354.9
58.9	0.1867	983.60	0.1241	2356.3
58.3	0.1819	983.91	0.1211	2357.7
57.8	0.1772	984.21	0.1181	2359.1
57.2	0.1727	984.45	0.1153	2360.2
56.7	0.1682	984.75	0.1125	2361.6
56.1	0.1638	985.06	0.1097	2363.0
55.6	0.1595	985.30	0.1070	2364.4
55.0	0.1553	985.60	0.1044	2365.8

Thermophysical properties of saturated water[132].

Temp.	Specific heat		Viscosity		Thermal conductivity		Surface tension
K	kJ/kgK		Ns/m^2		W/mK		N/m
	$c_{p,f}$	$c_{p,g}$	$\mu_f \cdot 10^6$	$\mu_g \cdot 10^6$	$k_f \cdot 10^2$	$k_g \cdot 10^3$	$\sigma_f \cdot 10^3$
273.15	4.217	1.854	1750	8.02	569	18.2	75.5
275	4.211	1.855	1652	8.09	574	18.3	75.3
280	4.198	1.858	1422	8.29	582	18.6	74.8

285	4.189	1.861	1225	8.49	590	18.9	74.3
290	4.184	1.864	1080	8.69	598	19.3	73.7
295	4.181	1.868	959	8.89	606	19.5	72.7
300	4.179	1.872	855	9.09	613	19.6	71.7
305	4.178	1.877	769	9.29	620	20.1	70.9
310	4.178	1.882	695	9.49	628	20.4	70.0
315	4.179	1.888	631	9.69	634	20.7	69.2
320	4.180	1.895	577	9.89	640	21.0	68.3
325	4.182	1.903	528	10.09	645	21.3	67.5
330	4.184	1.911	489	10.29	650	21.7	66.6
335	4.186	1.920	453	10.49	656	22.0	65.8
340	4.188	1.930	420	10.69	660	22.3	64.9
345	4.191	1.941	389	10.89	668	22.6	64.1
350	4.195	1.954	365	11.09	668	23.0	63.2
355	4.199	1.968	343	11.29	671	23.3	62.3
360	4.203	1.983	324	11.49	674	23.7	61.4
365	4.209	1.999	306	11.69	677	24.1	60.5
370	4.214	2.017	289	11.89	679	24.5	59.5
373.15	4.217	2.029	279	12.02	680	24.8	58.9
375	4.22	2.036	274	12.09	681	24.9	58.6
380	4.226	2.057	260	12.29	683	25.4	57.6
385	4.232	2.080	248	12.49	685	25.8	56.6
390	4.239	2.104	237	12.69	686	26.3	55.6
400	4.256	2.158	217	13.05	688	27.2	53.6
410	4.278	2.221	200	13.42	688	28.2	51.5
420	4.302	2.291	185	13.79	688	29.8	49.4
430	4.331	2.369	173	14.14	685	30.4	47.2
440	4.36	2.46	162	14.50	682	31.7	45.1
450	4.40	2.56	152	14.85	678	33.1	42.9
460	4.44	2.68	143	15.19	673	34.6	40.7
470	4.48	2.79	136	15.54	667	36.3	38.5
480	4.53	2.94	129	15.88	660	38.1	36.2
490	4.59	3.10	124	16.23	651	40.1	33.9

500	4.66	3.27	118	16.59	642	42.3	31.6
510	4.74	3.47	113	16.95	631	44.7	29.3
520	4.84	3.70	108	17.33	621	47.5	26.9
530	4.95	3.96	104	17.72	608	50.6	24.5
540	5.08	4.27	101	18.1	594	54.0	22.1
550	5.24	4.64	97	18.6	580	58.3	19.7
560	5.43	5.09	94	19.1	563	63.7	17.3
570	5.68	5.67	91	19.7	548	76.7	15.0
580	6.00	6.40	88	20.4	528	76.7	12.8
590	6.41	7.35	84	21.5	513	84.1	10.5
600	7.00	8.75	81	22.7	497	92.9	8.4

C Thermal Properties of Stainless Steel

Thermal properties of stainless steel[138].

Conductivity		Specific heat	
Temp. *K*	Conductivity *W/mK*	Temp. *K*	Specific heat *J/kgK*
80.4	8.3	71.8	286.5
107.6	9.7	114.0	329.7
154.8	11.5	162.9	367.0
195.2	12.8	197.9	392.3
247.3	14.2	270.0	433.4
299.3	15.2	337.3	465.0
379.1	16.5	435.1	500.7
442.5	17.5	587.6	540.7
516.5	18.4	736.5	561.8
611.1	19.8	967.7	604.5
687.8	20.8	1231.1	648.2
763.7	21.7	1468.5	690.2
855.7	22.8		
980.9	24.7		
1182.1	26.9		

Bibliography

[1] L. J. Heaslip and A. Mclean. Tundish metallurgy-consideration relating to tundish performance and metallurgical treatment during continuous casting. *Continuous casting*, Iron and Steel Society of AIME, vol. 1,pp. 93–97, 1983.

[2] A. Perkins and W. R. Irving. Two dimensional heat transfer model for continuous casting of steel. *Mathematical Process Models in Iron and Steelmaking*, The Metal Society,pp. 187–199, 1975.

[3] K. Takeo and H. Iwata. Continuous casting of high carbon steel. *Wire Journal*, August,pp. 32–38, 1971.

[4] H. Iwata, K. Yamada, T. Fujita, and K. Hayashi. Electromagnetic stirring of molten core in continuous casting of high carbon steel. *Transactions ISIJ*, vol. 16,pp. 374–381, 1976.

[5] H. Nashiwa, T. Kihsida, T. Nagahata, H. Tomono, and K. Tada. Continuous casting of slab, bloom and round billet at slab caster. *65th steelmaking conference proceedings*, Pittsburgh Meeting, vol. 65,pp. 49–58, 1982.

[6] J. E. Lait and J. K. Brimacombe. Solidification during continuous casting of steel. *Continuous casting*, Iron and Steel Society of AIME, vol. 2,pp. 171–183, 1984.

[7] C. Gomer and K. Andrews. Study of steel solidification by the use of radioactive isotopes. *Journal of the Iron and Steel Institute*, January,pp. 26–35, 1969.

[8] R. J. Gray, A. Perkins, and B. Walker. Quality of continuously cast slab. *Solidification and Casting of Metals*, pp. 300–305, 1977.

[9] K. Sorimachi, M. Shiraishi, and K. Kinoshita. Continuous casting of high carbon steel slabs at Chiba Works. *Continuous Casting of Steel, Proc. 2nd Process Tech. Conf.*, vol. 2, February 23-25,pp. 188–193, 1981.

[10] Y. Habu, T. Nozaki, M. Mabuchi, T. Ueda, and J. Bostedt. Development of tundish heating system for continuous casting. *Continuous Casting '85*, London,pp. 65.1–65.6, 1985.

[11] H. Abo, S. Nakamura, and H. Arai. The behaviour of non-metallic inclusions of continuous cast stainless steel slabs. *Process Technology Conference*, vol. 6, Wahsington Meeting,pp. 825–829, 1986.

[12] G. Drunen, J. K. Brimacombe, and F. Weinberg. Internal cracks in strand-cast billets. *Ironmaking & Steelmaking*, vol. 2,pp. 125–133, 1975.

[13] L. Backer and P. Gosselin. *Open Hearth Proc.*, vol. 53,pp. 145–156, 1970.

[14] C. I. Miller, Jr. *Open Hearth Proc.*, vol. 54,pp. 316–321, 1971.

[15] J. K. Brimacombe. Crack formation in the continuous casting of steel. *Continuous casting*, Iron and Steel Society of AIME, vol. 2,pp. 199–214, 1984.

[16] J. K. Brimacombe. Formation of longitudinal, midface cracks in continuously-cast slabs. *Continuous casting*, Iron and Steel Society of AIME, vol. 2,pp. 215–227, 1984.

[17] F. Weinberg. *Trans. Met. Soc., AIME*, vol. 221,pp. 844, 1961.

[18] Y. Tsuchida, I. Sugawara, S. Miyahara, and S. Tokushige. Behaviour of semi-macroscopic segregation in continuously cast slabs and technique for reducing the segregation. *Transactions ISIJ*, vol. 24,pp. 899–906, 1984.

[19] K. Ayata, T. Mori, T. Fujimoto, T. Ohnishi, and I. Wakasugi. Improvement of macrosegregation in continuously cast bloom and billet by electromagnetic stirring. *Transactions ISIJ*, vol. 24,pp. 931–939, 1984.

[20] A. Perkins and W. R. Irving. *Continuous Casting of Steel*, The Metal Society & IRSID, Biarritz,pp. 107–115, 1977.

[21] H. Mori, N. Tanaka, N. Sato, and M. Hirai. Microstructure of and segregation on continuously cast carbon steel billets. *Transactions ISIJ*, vol. 12,pp. 102–111, 1972.

[22] J. J. Moore. *Iron and Steelmaker*, vol. 7, No. 10,pp. 8–16, 1980.

[23] T. Adachi, M. Mizutani, and K. Kimura. Application of electromagnetic stirrers. *Continuous casting*, Iron and Steel Society of AIME, vol. 3,pp. 79–85, 1984.

[24] S. N. Singh and K. E. Blazek. Heat transfer and skin formation in a continuous-casting mold as a function of steel carbon content. *Journal of Metals*, October,pp. 17–27, 1974.

[25] A. A. Tzavaras. *Continuous Casting*, The Metallurgical Society, AIME, Chicago,pp. 198–214, 1973.

[26] M. Kawamoto, K. Yamada, and T. Fujita. *Wire Journal*, July,pp. 64–70, 1977.

[27] O. Haida, H. Kitaoka, Y. Habu, and S. Kakihara. Macro- and semi-macroscopic features of the centerline segregation in CC slabs and their effect on product quality. *Transactions ISIJ*, vol. 24,pp. 891–898, 1984.

[28] Y. Nakai, H. Kurahashi, T. Emi, and O. Haida. Development of steels resistant to hydrogen induced cracking in wet hydrogen sulfide environment. *Transactions ISIJ*, vol. 19,pp. 401–410, 1979.

[29] H. Mizukami, M. Komatsu, T. Kitagawa, and K. Kawakami. Effect of electromagnetic stirring at the final stage of solidification of continuous cast strand. *Transactions ISIJ*, vol. 24,pp. 923–930, 1984.

[30] L. Beitelman, J. A. Mulcahy, R. Hadden, et al. Influence of electromagnetic stirring on quality of continuously cast billets. *Continuous Casting of Steel, Proc. 2nd Process Tech. Conf.*, vol. 2, February 23-25,pp. 270–277, 1981.

[31] J. Birat and J. Chone. Electromagnetic stirring on billet, bloom and slab, continuous caster, state of the art in 1982. *Continuous casting*, Iron and Steel Society of AIME, vol. 3,pp. 21–34, 1984.

[32] J. J. Moore and N. A. Shah. A review of the effect of electromagnetic stirring (EMS) in continuously cast steels. *Continuous casting*, Iron and Steel Society of AIME, vol. 3,pp. 35–45, 1984.

[33] B. F. Blackwell. An efficient technique for the numerical solution of the one-dimensional inverse problem of heat conduction. *Numerical Heat Transfer*, vol. 4,pp. 229–239, 1981.

[34] C. J. Chen and D. M. Thomsen. On transient cylindrical surface heat flux predicted from interior temperature response. *AIAA Journal*, vol. 13,pp. 697–699, 1975.

[35] M. Imber. Nonlinear heat transfer in planar solids: direct and inverse applications. *AIAA Journal*, vol. 17,pp. 204–212, 1979.

[36] M. Imber. Inverse problem for the solid cylinder. *AIAA Journal*, vol. 17,pp. 91–94, 1979.

[37] G. P. Mulholl and M. H. Cobble. Diffusion through composite media. *Int. J. Heat Mass Transfer*, vol. 15,pp. 147–152, 1972.

[38] G. P. Mulholland and R. L. San Martin. Indirect thermal sensing in composite media. *Int. J. Heat Mass Transfer*, vol. 15,pp. 1056–1060, 1973.

[39] A. L. Alkidas. Heat transfer characteristics of a spark-ignition engine. *Journal of Heat Transfer*, vol. 102,pp. 189–193, 1980.

[40] T. K. J. Howse, R. Kent, and H. Rawson. The determination of glass-mould heat fluxes from mould temperature measurements. *Glass Technology*, vol. 12,pp. 91–93, 1971.

[41] E. M. Sparrow, A. Haji-Sheikh, and T. S. Lundgren. The inverse problem in transient heat conduction. *J. of Applied Mech., Trans. ASME, Series E*, vol. 86,pp. 369–375, 1964.

[42] A. M. Osman. Estimation of transient heat transfer coefficients in multidimensional problems by using in heat transfer methods. *Ph.D. thesis, Michigan State University, USA*, 1987.

[43] K. G. Omel'chenko and V. G. Pchelkina. Solution of an inverse problem of nonlinear heat conduction to determine thermophysical characteristics. *J. of Eng. Physics*, voi. 29,pp. 885–887, 1975.

[44] G. Stolz Jr. Numerical solutions to an inverse problem of heat conduction for simple shapes. *Journal of Heat Transfer*, vol. 82,pp. 20–26, 1960.

[45] J. V. Beck. Transient sensitivity coefficients for the thermal contact conductance. *Int. J. Heat Mass Transfer*, vol. 10,pp. 1615–1617, 1967.

[46] J. V. Beck. Surface heat flux determination using an integral method. *Nucl. End. Des.*, vol. 7,pp. 170–178, 1968.

[47] J. V. Beck. Determination of optimum, transient experiments for thermal contact conductance. *Int. J. Heat Mass Transfer*, vol. 12,pp. 621–633, 1969.

[48] J. V. Beck. Nonlinear estimation applied to the nonlinear inverse heat conduction problem. *Int. J. Heat Mass Transfer*, vol. 13,pp. 703–716, 1970.

[49] J. V. Beck. Criteria for comparison of methods of solution of the inverse heat conduction problem. *Nuclear Engineering and Design*, vol. 53,pp. 11–22, 1979.

[50] J. V. Beck, B. Blackwell, and C. R. St. Clair, Jr. *Inverse Heat Conduction.* A Wiley-Interscience Publication, 1985.

[51] A. N. Tikhonov and V. Y. Arsenin. *Solution of Ill-Posed Problems.* V. H. Winstom & Sons, Wash., D. C., 1977.

[52] M. Raynaud and J. V. Beck. Methodology for comparison of inverse heat conduction methods. *Journal of Heat Transfer*, vol. 110,pp. 30–37, 1988.

[53] J. M. Davis. Input power determined from temperatures in simulated skin protected against thermal radiation. *Journal of Heat Transfer*, vol. 88,pp. 154–160, 1966.

[54] I. Frank. An application of least square methods to the solution of the inverse problem of heat conduction. *Journal of Heat Transfer*, vol. 85,pp. 378–379, 1963.

[55] J. V. Beck. Calculation of surface heat flux from an internal temperature history. *ASME Paper 62-HT-46*, 1962.

[56] O. M. Alifanov. Inverse boundary-value problem of heat conduction. *J. Eng. Physics*, vol. 29,pp. 821–830, 1975.

[57] O. M. Alifanov and F. A. Artyukhin. Regularized numerical solution of nonlinear inverse heat-conduction problem. *J. of Eng. Physics*, vol. 29,pp. 934–938, 1975.

[58] J. B. Bell and A. B. Wardlaw. Numerical solution of an ill-posed problem arising in wind tunnel heat transfer data reduction. Naval Surface Weapons Center, NSWC TR 82-83, Dec., 1981.

[59] J. B. Bell. The noncharacteristic cauchy problem for class of equation with time dependence. I. problems in one space dimensions. *SIAM, J. Math. Anal.*, vol. 12,pp. 759–777, 1981.

[60] J. V. Beck and D. Murio. Combined function specification-regularization procedure for solution of inverse heat conduction problems. *AIAA Paper No. AIAA-84-0419*, January, 1984.

[61] D. W. Van Krevelen and P. J. Hoftyzer. *Properties of Polymers*. Elsevier Scientific Publishing Company, 1976.

[62] S. Ostrach. An analysis of laminar free convection flow and heat transfer about a flat plate parallel to the direction of the generating body force. *NASA Report 1111*, 1953.

[63] V. I. Kononenko, S. P. Yastenko, and I. M. Privalov. Viscosity and electrical resistivity of liquid aluminum. *High Temperature*, vol. 7, No. 2,pp. 243–246, 1969.

[64] R. S. Gaugler. Heat transfer device. *US Patent 2350348, Published 6 June*, 1944.

[65] G. M. Grover. Evaporation-condensation heat transfer device. *US Patent 3229759, Published 18 January*, 1966.

[66] K. T. Feldman and G. H. Whiting. The heat pipe and its application. *Engrs. Dig.*, London, vol. 28, No. 3,pp. 86–96, 1967.

[67] G. Y. Estman. The heat pipe. *Scientific American*, vol. 218, No. 5,pp. 38–46, 1968.

[68] K. T. Feldman and G. H. Whiting. Application of the heat pipe. *Mech. Engng.*, Nov., vol. 90,pp. 48–53, 1968.

[69] J. E. Deverall and J. E. Kemme. Satellite heat pipe. *USAEC Report LA-3278, Contract W-7405-eng-36.*, Los Alamos Sci. Lab., Univ. of Calif., 1970.

[70] T. Wyatt. A controllable heat pipe experiment for the SE-4 satellite. *JHU Tech. Memo APL-SDO-1134*, Johns Hopkins Univ., Appl. Physics Lab., 1965.

[71] J. L. Thurman and S. Mei. Application of heat pipes to spacecraft thermal control problems. *Tech. Note AST-275*, Brown Engineering, 1968.

[72] D. K. Anold. Heat pipe application to a gravity gradient satellite. *Proc. of ASME Annual Aviation and Space Conf.*, Beverley Hills, California, 16-19 June,pp. 634–658, 1968.

[73] E. D. Waters. Arctic tundra kept frozen by heat pipes. *The Oil and Gas Journal*, Aug. vol. 26,pp. 122–125, 1974.

[74] V. Zbořil and P. Stulc. Heat pipe in computer modules. *Research and Development of Heat Pipe Technology, Proc. V Int. Heat Pipe Conf., Part 1*, May 14-18, Tsukuba, Japan,,pp. 336–345, 1984.

[75] B. S. Larkin. Temperature control of electronic systems using inexpensive heat pipes. *Research and Development of Heat Pipe Technology, Proc. V Int. Heat Pipe Conf., Part 1*, May 14-18, Tsukuba, Japan,,pp. 346–351, 1984.

[76] V. Zbořil. Heat pipe cooling in computer electronics. *Advances in heat pipe technology, Proc. IV Int. Heat Pipe Conf.*, Pergamon Press, New York,pp. 767–779, 1981.

[77] O. Brost, J. Unk, and W. R. Canders. Heat pipes for electric motors. *Research and Development of Heat Pipe Technology, Proc. V Int. Heat Pipe Conf., Part 1*, May 14-18, Tsukuba, Japan,,pp. 359–364, 1984.

[78] F. Thoren. Heat pipe cooled induction motors. *Research and Development of Heat Pipe Technology, Proc. V Int. Heat Pipe Conf., Part 1*, May 14-18, Tsukuba, Japan,,pp. 365–372, 1984.

[79] T. Osakabe et al. Application of heat pipe to audio amplifier. *Advances in Heat pipe technology, Proc. IV Int. Heat Pipe Conf.*, Pergamon Press,pp. 25–36, 1981.

[80] H. Takagi, T. Mohtai, T. Kojima, et al. Study of latent heat thermal storage system using heat pipes for cooling underground power cable. *Research and Development of Heat Pipe Technology, Proc. V Int. Heat Pipe Conf., Part 2*, May 14-18, Tsukuba, Japan,,pp. 153–293, 1984.

[81] S. Kawakami, S. Yoshida, K. Matusumoto, and T. Koizumi. Application of heat pipes to a thermal storage cooling system. *Research and Development of Heat Pipe Technology, Proc. V Int. Heat Pipe Conf., Part 1*, May 14-18, Tsukuba, Japan,,pp. 156–166, 1984.

[82] A. Abhat. High performance heat pipes for a latent heat thermal energy storage application. *Research and Development of Heat Pipe Technology, Proc. V Int. Heat Pipe Conf., Part 1*, May 14-18, Tsukuba, Japan,,pp. 321–327, 1984.

[83] H. Jutusna, K. Akagawa, and S. Mizuno. Thermosyphon heat pipes for long-term underground storage of solar energy. *Research and Development of Heat Pipe Technology, Proc. V Int. Heat Pipe Conf., Part 1*, May 14-18, Tsukuba, Japan,,pp. 293–301, 1984.

[84] K. H. Kim and Y. Lee. A study on the use of two-phase closed thermosyphons for latent heat storage system. *Research and Development of Heat Pipe Technology, Proc. V Int. Heat Pipe Conf., Part 1*, May 14-18, Tsukuba, Japan,,pp. 316–320, 1984.

[85] D. A. Reay. *Industrial Energy Conservation.* Pergamon Press, 1977.

[86] R. O. Barratt and G. O. Henderson. The heat pipe air preheater. *Foster Wheeler Publication, Paper SP79-9*, Foster Wheeler Corporation, New Jersey, 1979.

[87] D. A. Littwin and J. McCurley. Heat pipe waste heat recovery boilers. *Advances in heat pipe technology, Proc. IV Int. Heat Pipe Conf.*, Pergamon Press, New York,pp. 213–224, 1981.

[88] M. Merrigan, W. Dunwoody, and L. Lundberg. Heat pipe development for high temperature recuperator application. *Advances in heat pipe technology, Proc. IV Int. Heat Pipe Conf.*, Pergamon Press, New York,pp. 245–257, 1981.

[89] T. P. Cotter. Theory of heat pipes. *USAEC Report LA-3246, Contract W7405-eng-36*, Los Alomos Sci. Lab., Univ. of Calif., 1968.

[90] E. K. Levy. Theoretical investigation of heat pipes operating at low vapor pressure. *J. Eng. Ind.*, voi. 90,pp. 547–552, 1968.

[91] J. E. Kemme. Ultimate heat-pipe performance. *IEEE Trans. on Electron Devices*, vol. ED-16,pp. 717–723, 1969.

[92] J. E. Deverall, J. E. Kemme, and L. W. Florschuetz. Sonic limitations and startup problems of heat pipes. *Los Alamos Sci. Lab. Rept. No. LA-4578*, 1970.

[93] J. E. Kemme. High performance heat pipes. *Proc. 1967 Thermionic Conversion Specialist Conference*, Palo Alto, California, October, 1967.

[94] E. C. Philips and J. D. Hinderman. Determination of capillary properties useful in heat pipe design. *A.S.M.E.- A.I.Ch.E. Heat Transfer Conf.*, Minneapolis, Minnesota, August, 1967.

[95] P. D. Dunn and D. A. Reay. *Heat Pipes.* Pergamon Press, 1982.

[96] A. Basiulis, R. C. Prager, and T. R. Lamp. Compatibility and reliability of heat pipe materials. *Proc. 2nd Int'l Heat pipe Conf.*, Bologna, Italy,pp. 357–372, 1976.

[97] T. Yamamoto and Y. Tanaka. Experimental study of sodium heat pipes. *JSME International Journal*, vol. 30,pp. 1776–1782, 1987.

[98] M. N. Ivanovsky, V. P. Sorokin, V. I. Subbotin, et al. Investigation of heat transfer capillary limit in sodium heat pipes. *Proc. 2nd Int'l Heat pipe Conf.*, Bologna, Italy,pp. 733–739, 1976.

[99] G. Grassi, P. G. Grassi, G. Coggiola, and L. Crovini. Analysis and experimental evaluation of the characteristics of water and sodium annular heat-pipe. *Proc. 2nd Int'l Heat pipe Conf.*, Bologna, Italy,pp. 555–571, 1976.

[100] H. Imura, K. Sasaguchi, and H. Kozai. Critical heat flux in a closed two-phase thermosyphon. *Int. J. Heat Mass Transfer*, vol. 26, No. 8,pp. 1181–1188, 1983.

[101] Y. Lee and U. Mital. A two-phase closed thermosyphon. *Int. J. Heat Mass Transfer*, vol. 15,pp. 1695–1707, 1972.

[102] S. Rosler, M. Takuma, M. Groll, and S. Maezawa. Heat transfer limitation in a vertical annular closed two-phase thermosyphon with small fill rate. *Heat Recovery System & CHP*, vol. 7,pp. 319–327, 1987.

[103] B. S. Larkin. An experimental study of the two-phase thermosyphon tube. *Transaction of the CSME*, vol. 14, No. B-6,pp. 39–46, 1971.

[104] F. E. Andros and L. W. Florschuetz. Heat transfer characteristics of the two-phase closed thermosyphon (wickless heat pipe). *Proceedings of the Seventh International Heat Transfer Conference*, vol. 4,pp. 187–192, 1982.

[105] K. Negishi and T. Sawada. Heat transfer performance of an inclined two-phase closed thermosyphon. *Int. J. Heat Mass Transfer*, vol. 26, No 8,pp. 1207–1213, 1983.

[106] U. Grob and E. Hahne. Reflux condensation inside a two phase thermosyphon at pressure up to the critical. *Proceedings of the Eighth International Heat Transfer Conference*, vol. 4,pp. 1613–1620, 1986.

[107] S. J. Chen, J. G. Reed, and C. L. Tien. Reflux condensation in a two-phase closed thermosyphon. *Int. J. Heat Mass Transfer*, vol. 27, No. 9,pp. 1587–1594, 1984.

[108] T. Ueda, T. Miyashita, and P. Chu. Heat transport characteristics of a closed two-phase thermosyphon. *JSME International Journal*, vol. 32, No. 2,pp. 239–246, 1989.

[109] H. Nguyen-Chi and G. Groll. Entrainment or flooding limit in a closed two-phase thermosyphon. *Advances in heat pipe technology, Proc. IV Int. Heat Pipe Conf.*, Pergamon Press, New York,pp. 147–162, 1981.

[110] K. Harada, S. Inoue, J. Fujita, H. Suematu, and Y. Wakiyama. Heat transfer characteristics of large heat pipe. *Hitachi Zosen Tech. Rev.*, vol. 41,pp. 167–174, 1980.

[111] E. Hahne and U. Gross. The influence of the inclination angle on the performance of a closed two-phase thermosyphon. *Advances in heat pipe technology, Proc. IV Int. Heat Pipe Conf.*, Pergamon Press, New York,pp. 125–136, 1981.

[112] M. Groll and Th. Spendel. The behaviour of high performance closed two-phase thermosyphons. *Research and Development of Heat Pipe Technology, Proc. V Int. Heat Pipe Conf., Part 1*, May 14-18, Tsukuba, Japan,,pp. 30–35. 1984.

[113] K. Kobayashi, T. Yamamoto, T. Kuroki, and K. Nagata. Heat transfer performance of a two-phase closed thermosyphon. *Research and Development of Heat Pipe Technology, Proc. V Int. Heat Pipe Conf., Part 2*, May 14-18, Tsukuba, Japan,,pp. 80–86, 1984.

[114] B. S. Larkin. An experimental study of the temperature profiles and heat transfer coefficients in a heat pipe for a heat exchanger. *Advances in heat pipe technology, Proc. IV Int. Heat Pipe Conf.*, Pergamon Press, New York,pp. 177–191, 1981.

[115] U. Grob and E. Hahne. Heat transfer in a two-phase thermosyphon operating with a fluid in the near critical state. *Int. J. Heat Mass Transfer*, vol. 28,pp. 589–601, 1985.

[116] I. C. Bilegan and D. Fetcu. Performance characteristics of gravity-assisted aluminum extruded heat pipes. *Advances in heat pipe technology, Proc. IV Int. Heat Pipe Conf.*, Pergamon Press, New York,pp. 89–94, 1981.

[117] F. E. Andros. Heat transfer characteristics of the two-phase closed thermosyphon(wickless heat pipe) including direct flow observations. *Ph.D. thesis, Arizona State University, USA*, 1980.

[118] R. L. Hirshberg. Laminar film flow phenomena - theory and application to the two-phase closed thermosyphon. *Ph.D. thesis, Arizona State University, USA*, 1980.

[119] T. Yamamoto and Y. Tanaka. Long-term operation test of sodium heat pipe. *Research and Development of Heat Pipe Technology, Proc. V Int. Heat Pipe Conf., Part 1*, May 14-18, Tsukuba, Japan,,pp. 186–192, 1984.

[120] W. D. Munzel. Compatibility tests of various heat pipe working fluids and structural materials at different temperatures. *Proc. 3rd Int'l Heat pipe Conf.*, Palo Alto, Calif.,pp. 96–101, 1978.

[121] S. W. Petrick. Hydrogen generation in water/stainless steel heat pipes. *ASME 72-WA/HT-30, presented November 28 - December 2*, New York, New York, 1972.

[122] C. A. Busse et al. Hydrogen generation in water heat pipes at 250 °C. *International Heat Pipe Conference*, October 15-17, Stuttgart, Germany, 1973.

[123] J. Schwartz. Performance map of the water heat pipe and the phenomenon of noncondensible gas generation. *ASME 69-HT-15, presented August 3-6*, Minneapolis, Minnesota, 1969.

[124] S. W. Chi. *Heat pipe theory and practice, A source book*. Hemisphere Publishing Cooperation, 1976.

[125] W. Nusselt. Die oberflächenkondensation des wasserdampfes. *Z. Ver. Deut. Ing.*, 60,pp. 541–569, 1916.

[126] G. F. Hewitt and N. Hall-Taylor. *Annular Two-Phase Flow*. Pergamon Press, 1970.

[127] Shyh-Jou Chen. Reflux condensation and operating limits of the two-phase closed thermosyphon. *Ph.D. thesis, University of California, Berkeley, USA*, 1984.

[128] F. Coyne Prenger. Performance limit of gravitity-assisted heat pipes. *Research and Development of Heat Pipe Technology, Proc. V Int. Heat Pipe Conf., Part 1*, May 14-18, Tsukuba, Japan,pp. 1–5, 1984.

[129] F. Coyne Prenger, Jr. and J. E. Kemme. Performance limit of gravity-assisted heat pipes with simple wick structure. *Advances in heat pipe technology, Proc. IV Int. Heat Pipe Conf.*, Pergamon Press, New York,pp. 137–146, 1981.

[130] S. S. Kutateladze. *Problems of Heat Transfer and Hydraulics of Two-Phase Media.* Pergamon Press, Oxford, 1969.

[131] M. N. Ivanovskii, V. P. Sorokin, and I. V. Yagodkin. The physical principles of heat pipes. Clarendon Press, Oxford,pp. 120, 1982.

[132] F. P. Incropera and D. P. DeWitt. *Fundamentals of Heat Transfer.* John Wiley & Sons, 1981.

[133] G. H. Golden and J. V. Tokar. Thermophysical properties of sodium. Argonne National Laboratory, August, 1967.

[134] M. Makansi, W. A. Selke, and C. F. Bonilla. Thermodynamic properties of sodium. *J. Chemical and Engineering Data*, vol. 5, No. 1, January,pp. 441–452, 1960.

[135] Atomic Energy Commission. Liquid-metals handbook. June, 1955.

[136] W. M. Rohsenow, J. P. Harnett, and E. N. Ganic. *Handbook of Heat Transfer Fundamentals.* 2nd edition, McGraw-Hill Book Co., 1986.

[137] Robert C. Weast ed. CRC handbook of chemistry and physics. CRC Press, Inc., 60th ed.,pp. E–20 – 23, 1980.

[138] American Society for Metals. Metals handbook. 9th edition, vol. 3.

Claims to Originality

Continuous temperature measurement of molten steel in new as well as existing steelmaking processes is not always feasible with current technology. Conventional thermocouples cannot withstand the severe corrosion around the slag line for a sustained period of time, although, molten steel temperature can have a profound effect on the quality of the product during the continuous casting operation. A knowledge of the instantaneous steel temperature in the tundish can serve as a valuable tool in the quest for better quality. This thesis contains many original features that should permit one to achieve a continuous steel temperature measurements in the tundish including:

1. Two mathematical models (1-D and 2-D) that track melt temperature have been developed using the readings from two embedded thermocouples to deduce bath temperature. Formulation of the inverse heat conduction problem(IHCP) was refined and incorporated into these models.

2. Thermal diffusivity(α) as a function of temperature can be computed(Eq. (2.29)) from a knowledge of three temperatures as measured by thermocouples located at equal spacings in the test section.

3. A low temperature heat pipe employing water as the working fluid was tested in a bath of molten tin. Solid tin crust was formed on outer surface of the heat pipe. Simple calculations to estimate the solid tin shell thickness were performed for one dimensional heat conduction through the solid tin.

4. An equation has been derived in an effort to allow for the prediction of the heat flow rate from the pressure transducer readings.

5. An annular heat pipe using sodium as the working fluid and stainless steel as the pipe material was built and tested. It was shown that the thermocouple probe can be protected from severe corrosion around slag line by the solidification of slag onto the heat pipe which then serves to protect the probe.